A study of quasi-thermal noise and shot noise in space plasmas

Mihailo M. Martinović

A thesis presented for the title of
PhD of the Observatoire de Paris
PhD of the University of Belgrade
Specialty: Astronomy and astrophysics

LESIA
Observatoire de Paris
École Doctorale A&A
France

Катедра за астрономију
Математички факултет
Универзитет у Београду
Србија

20.10.2016.

Thesis title in French

Une étude du bruit quasi-thermique et du bruit d'impact dans les plasma spatiaux

Thesis title in Serbian

Спектроскопија квази-термалних шумова и ударних електронских сигнала у свемирској плазми

	Jury
Reviewers	Adolfo Figueroa Vinas
	Hervé Lamy
Examinators	Jagoš Purić
	Dušan Jovanović
	Christophe Sauty
Co-mentors (French)	Milan Maksimović
	Arnaud Zaslavsky
Co-mentor (Serbian)	Stevo Šegan

In loving memory to Žarko Gavrilović,
the greatest man I ever knew

Acknowledgments

I want to thank...

Abstract

The quasi-thermal noise spectroscopy is an accurate method of determination of density and temperature in space plasmas. When an electric antenna is immersed into a plasma, it is able to measure electrostatic fluctuations caused by the thermal motion of plasma particles. These fluctuations are detected as the power spectral density at the antenna terminals, observing a spectrum at frequencies comparable to the electron plasma frequency for both electrons and protons, since the proton signal is strongly Doppler-shifted towards higher frequencies due to the solar wind drift velocity. Beside inducing the fluctuating electric field, some of the electrons are impacting the antenna surface, causing disturbances of the antenna electric potential. The signal caused by this population is directly proportional to the flux of plasma electrons impacting the antenna and is dominant if the antenna has a large surface area. In this work, we use the orbit limited theory to calculate the incoming particle flux for a non-thermal plasma described by κ velocity distribution function, commonly measured in the solar wind. The increase in the particle collection by cylindrical and spherical objects is quantified and presented as a function of the surface electrostatic potential and the fraction of supra-thermal particles. Including these results into the theory has turned out to be absolutely necessary for accurate measurements of the plasma parameters whenever the shot noise is the dominant component in the power spectrum. This is the case for STEREO because the impact noise is overwhelming on this probe, due to the presence of short and thick antennas. The comprehensive study of data on this mission is motivated by the fact that the electron analyzers are malfunctioning since launch and no information on thermal electrons is available. Results obtained are verified by comparing with the results from Wind, showing a good match between the values measured by the two spacecraft. Uncertainties of the measurements are determined by the uncertainties of the instruments used and are estimated to be around 40%. The final outcome of this work will be establishing a database of the electron moments in both STEREO A and B that will be covering the entire duration of the mission. In the second part of the thesis, we use the kinetic approach to expand the theory of the quasi-thermal noise to plasmas where electron-neutral collisions play a dominant role. This technique is able to measure the electron density, temperature and the collision frequency as independent parameters using the wide frequency range both below and above the plasma frequency, if the ratio of the collisional to plasma frequency is not smaller than 0.1. The results presented here have can be potentially applied in laboratory plasmas and unmagnetized ionospheres, while at the ionosphere of Earth their use is limited to low frequencies due to the presence of the magnetic field.

Résumé

La spectroscopie de bruit quasi-thermique est une méthode précise de détermination de la densité et de la température dans les plasmas spatiaux. Lorsqu'une antenne électrique est immergé dans un plasma, elle est capable de mesurer les fluctuations électrostatiques provoquées par le mouvement thermique des particules de plasma. Ces fluctuations sont détectées par la densité de puissance spectrale aux bornes de l'antenne, en observant un spectre à des fréquences comparables à la fréquence plasma électronique aussi bien pour les électrons que pour les protons, car le signal du proton est fortement décalé Doppler vers des fréquences plus élevées en raison de la vitesse de dérive du vent solaire. En plus d'induire le champ électrique fluctuant, une partie des électrons impactent sur la surface de l'antenne, ce qui provoque des perturbations de son potentiel électrique. Le signal provoqué par cette population est directement proportionnelle au flux d'électrons du plasma impactant l'antenne et est dominante si l'antenne a une grande surface. Dans ce travail, nous utilisons la théorie de l'orbite limite pour calculer le flux de particules impactantes pour un plasma non thermique décrit par fonction de distribution de vitesses κ ou Lorentzienne, communément mesurée dans le vent solaire. L'augmentation de la collecte de particules par des objets cylindriques et sphériques est quantifié et présenté en tant que fonction du potentiel électrostatique de surface et de la fraction des particules supra-thermique. La prise en compte de ces résultats théoriques est absolument nécessaire pour des mesures précises des paramètres du plasma à chaque fois que le bruit d'impact est l'élément dominant dans le spectre de puissance. Ceci est le cas pour STEREO, car les bruit d'impact est dominant pour cette sonde, en raison de la présence d'antennes courtes et épaisses. L'étude approfondie des données sur cette mission est motivée par le fait que ses analyseurs d'électrons sont défectueux depuis le lancement et aucune information sur les électrons thermiques n'est disponible. Les résultats obtenus sont vérifiés en comparant avec les résultats de Wind, montrant une bonne concordance entre les valeurs mesurées par les deux satellites. Les incertitudes des mesures sont déterminées par les incertitudes des instruments utilisés et sont estimés à environ 40%. Le résultat final de ce travail sera l'établissement d'une base de données des moments d'électrons pour les deux sondes STEREO A et B qui couvriront toute la durée de la mission. Dans une seconde partie de la thèse, nous utilisons l'approche cinétique pour étendre la théorie du bruit quasi-thermique à des plasmas où les collisions des électrons avec les neutres jouent un rôle dominant. Cette technique permet de mesurer la densité et la température des électrons, et aussi la fréquence des collisions en tant que paramètres indépendants. Ceci est obtenu sur une large gamme de fréquences aussi bien en dessous qu'au dessus de la fréquence plasma, pour peu que le rapport entre la fréquence de collision et fréquence de plasma ne soit pas inférieur à 0.1. Les résultats présentés ici peuvent potentiellement être appliqués avec succès dans les plasmas de laboratoire et ionosphères non

magnétisés, tandis que pour l'ionosphère de la Terre leur utilisation est limitée aux fréquences basses à cause de la présence d'un champ magnétique fort.

Резиме

Спектроскопија квази-термалних шумова је прецизна метода за одређивање концентрације и температуре свемирске плазме. Електрична антена која се налази у плазми може мерити електростатичке флуктуације које долазе од термалног кретања наелектрисаних честица. Радио пријемник за који се везују крајеви диполне антене мери спектар у опсегу око плазмене фреквенце. На овај начин могу се детектовати сигнали који долазе и од електрона и од протона јер је протонска компонента подложна значајном Доплеровом померају ка вишим фреквенцама услед велике брзине усмереног кретања сучевог ветра. Неке честице, осим што индукују сигнал путем флуктуација електричног поља, такође ударају у површину антене изазивајући промене у електричном потенцијалу. Сигнал који настаје на овај начин је директно сразмеран флуксу ударних електрона и доминантан је у мереном спектру уколико антена има велику површину. У овом раду користи се теорија ограниченог орбиталног кретања у циљу израчунавања флукса долазећих честица у плазми ван термалне равнотеже описаној κ расподелом по брзинама, каква је уобичајено мерена у сунчевом ветру. Увећање броја честица сакупљених на површини антене је одређено у зависности од процента нетермалних брзих честица у функцији расподеле. Употреба ових резултата у склопу коришћене теорије се испоставила неопходна у случајевима када је допринос ударних електрона значајан. Оваква ситуација је карактеристична за сателит STEREO који је опремљен кратким антенама великог пречника и овакав њихов облик чини ударне сигнале доминантнима у мереном спектру. Детаљна студија података са ове мисије је мотитвисана чињеницом да електронски анализатори не функционишу исправно на ниским енергијама и никакви подаци о термалним електронима не постоје за читав ток мисије. Добијени резултати су упоређени са поузаним резулатима сателита Wind и добијен је задовољавајући ниво сагласности. Грешке мерења су условљене нивоом прецизности инструмента и процењене су на око 40%. Коначни производ овог рада ће бити реализација базе података момената функције расподеле електрона за STEREO A и STEREO B која ће покривати читав ток мисије. У другом делу дисертације, коришћењем кинетичке теорије, проширена је теорија квазитермалних шумова на плазме у којима судари између електрона и неутралних честица играју значајну улогу. Овим путем је развијена метода способна да мери електронску густину, температуру и фреквенцију судара као независне параметре уколико однос ударне и плазмене фреквенце није мањи од 0.1. Представљени резултати могу бити коришћени у лабораторијским плазмама и немагнетизованим јоносферама док је у јоносфери Земље њихова употреба ограничена на ниске фреквенце због присуства Земљиног магнетног поља.

Contents

Notation

Mathematical functions		
	Definition	**Expression**
$Si(z)$	Sine integral	$\int_0^z \frac{\sin t}{t} dt$
$J_n(z)$	n-th order Bessel function of the first kind	$\frac{1}{2\pi i} \oint e^{\frac{z}{2}(t-\frac{1}{t})} dt$
$I_n(z)$	Modified $J_n(z)$	$\frac{1}{2\pi i} \oint e^{\frac{z}{2}(t+\frac{1}{t})} dt$
$Z_0(z)$	Plasma dispersion function	$\frac{1}{\pi^{1/2}} \int_{-\infty}^{\infty} \frac{e^{-t^2}}{t-z} dt$
$\Gamma(z)$	Gamma function	$\int_0^{\infty} t^{z-1} e^{-t} dt$
${}_2\bar{F}_1(a,b;c;z)$	Regularized hypergeometric function	$\sum_{k=0}^{\infty} \frac{\Gamma(a+k)\Gamma(b+k)z^k}{\Gamma(a)\Gamma(b)\Gamma(c+k)k!}$
$erf(z)$	Error function	$\frac{2}{\pi^{1/2}} \int_0^z e^{-t^2} dt$
$erfc(z)$	Complementary error function	$1 - erf(z)$
$erfi(z)$	Imaginary error function	$\frac{1}{i} erf(iz)$
Physical constants		
	Definition	**Value**
e	Elementary charge	$1.6 \cdot 10^{-19} C$
m_e	Electron mass	$9.1 \cdot 10^{-31} kg$
m_p	Proton mass	$1.67 \cdot 10^{-27} kg$
k_b	Boltzmann constant	$1.38 \cdot 10^{-23} J/^{\circ}K$
ϵ_0	Dielectric permittivity of vacuum	$8.85 \cdot 10^{-12} F/m$

μ_0	Magnetic permeability of vacuum	$4\pi \cdot 10^{-7} N/A^2$
c	Speed of light	$3 \cdot 10^8 m/s$
Physical quantities		
	Definition	
n_e	Electron density	
T_e	Electron temperature	
T_e^*	Generalized electron temperature	
L_D	Electron Debye length	
v_{the}	Electron thermal velocity	
v_{sw}	Solar wind bulk velocity	
ω_p	Electron plasma frequency	
ω_i	Ion plasma frequency	
ν	Electron collision frequency	
Ω_e	Electron cyclotron frequency	
ϵ	Plasma dielectric permittivity	
$f(\vec{v})$	Velocity distribution function	
V_0^2	Power spectral density	
V_{qtn}^2	Electron power spectral density	
V_{pn}^2	Proton power spectral density	
V_{sn}^2	Shot noise	
Antenna-related quantities		
V_0	Tip-to-tip potential difference	
Γ	Gain	

L_{ant}	Half-length (wire dipole)
L	Half-length (sphere dipole)
L_{eff}	Effective half-length (wire dipole)
a_{ant}	Radius (wire dipole)
a	Radius (sphere dipole)
S_{ant}	Surface (dipole)
S_{mon}	Surface (monopole)
$\vec{j_a}$	Current density
I_a	Current at the terminals
Z_{ant}	Impedance (dipole)
R_{ant}	Resistance (dipole)
Z_{mon}	Impedance (monopole)
C_{ant}	Capacitance (dipole)
C_{mon}	Capacitance (monopole)
C_{stray}	Stray capacitance (dipole)
C_{ms}	Stray capacitance (monopole)
ϕ	Electrostatic potential
Φ_{ph}	Photoelectron flux
T_{ph}	Photoelectron temperature

Chapter 1

Introduction

The natural noises detected by antennas in space plasmas are being studied for half a century now [Andronov, 1966, Fejer and Kan, 1969]. These signals are caused by the electrostatic fluctuations induced by thermal motion of plasma particles. The quasi-thermal noise (QTN) spectroscopy [Meyer-Vernet, 1979] is the technique developed in order to theoretically explain the measured antenna power spectrum and, based on its features, determine the velocity distribution function (VDF) moments of the surrounding plasma.

The measured QTN spectrum is dependent on the antenna configuration as well as on the plasma parameters. If the antennas used are dipoles that are long and thin (compared to plasma Debye length L_D) then the spectrum observed will be suitable for determination of both electron and proton density and temperature, as well as characteristics of supra-thermal particles, as independent parameters (see e.g. [Issautier et al., 1999]). Multiple spacecraft launched in past several decades, like ISEE3, Ulysses or Wind were equipped with antennas of satisfying characteristics that provided very 'clean' measurements, in good agreement with the theory (see Section 2.5 for details). This technique is a routinely used, powerful diagnostic tool in the solar wind plasma since it has several very positive features. Some of the most important ones are being almost independent of the spacecraft floating potential and possibility to quickly estimate the total electron density from the location of so called 'plasma peak' that appears in the spectrum just above the plasma frequency, given as $\omega_p = \sqrt{n_e e^2/\epsilon_0 m_e}$ (with n_e, e and m_e being electron density, charge and mass, respectively and ϵ_0 is dielectric permittivity of vacuum). This well known theory of the QTN is reviewed in Chapter 2.

However, some current and also future missions use radio instruments that are not primarily designed for observing the QTN and therefore the measured spectra will not have all the desirable features described above. This is the case for NASA STEREO spacecraft which carry both in-situ and remote sensing instruments and require therefore to be 3-axis stabilized during their operations at $1AU$ (Section 2.5). As a consequence only short, rigid and thick radio antennas have been installed on these spacecraft and the method described above was planned to be a 'bi-product', used only during coronal mass ejection (CME) events, when Debye length is small. Unexpectedly, electron analyzers experienced major issues measuring low energies and there is no data on thermal electrons at all for this mission. This work aims to recover this missing data (on a confidence level determined by the instrument characteristics), using the QTN spectroscopy, and prepare basis for producing the

electron moments database. In order to perform this task, several major theoretical and practical issues needed to be resolved along the way. For instance, since the antennas are shorter then the Debye length in the quiet solar wind, the characteristic plasma peak is not possible to observe while the signal that comes from the electrons impacting the antenna surface, which is strongly dependent on the antenna floating potential, becomes dominant due to antenna thickness. This so called shot noise has very low intensity for thin antennas used on previous missions and the theory that describes it offers only approximative expressions. This thesis further develops the shot noise theory, deriving precise theoretical expressions for the flux of particles collected by the antenna in the solar wind and, consequently, the shot noise below the plasma frequency. The results presented here are not important just for investigation of the specific spectra observed by STEREO, but will also be necessarily exploited on future missions Solar Orbiter and Solar Probe Plus, aimed to explore the interior of the solar corona and origins of the solar wind, as well as on Turbulence Heating ObserveR (THOR), primarily intending to explore plasma turbulence in the proximity of the Earth's bow shock, if this mission gets selected. All of these spacecraft will have the antennas with similar characteristics as the ones on STEREO.

Another research area, expected to be intensively explored in the future, is the development of cubesats and, in general, the QTN spectroscopy as a piggyback technique on complicatedly shaped devices (e.g. tubular booms). For this purpose, we explore the plasmas whose behavior is determined by collisions between electrons and neutrals. Using the method developed here, we are able to measure, beside n_e and T_e, the collision frequency ν as a separate independent parameter as long as $\nu/\omega_p \geq 0.1$. The possible applications of the theory in laboratory plasmas and unmagnetized ionospheres are also discussed. The usage in laboratory experiments can be double-natured. First, as a precise diagnostic tool for measuring the plasma parameters using wide frequency range, both below and above the plasma frequency. Second, the technique we introduce here would enable the validation, by ground testing, of various kinds of sensor geometries for QTN spectroscopy purposes. As recently proposed during the PIANOS project, both 3D stable and spinning configurations are interesting to test, including different types of booms or tethers.

The theoretical work related to determination of the incoming particle flux on the antenna surface and also the antenna charging in the solar wind is presented in Chapter 3 and partially published in [Martinović, 2016]. Applications to STEREO data and perspectives related to establishing of the electron moments database are given in Chapter 4 and by [Martinović et al., 2016b], while theory of the QTN in weakly ionized collisional plasmas is developed in Chapter 5 and [Martinović et al., 2016a]. Some predictions of the QTN spectroscopy perspectives and chalenges related to the future missions are briefly discussed in Section 6.

Chapter 2

Quasi-thermal noise in space plasmas

2.1 The Sun and the solar wind

2.1.1 The mystery of solar corona

Since the ancient times, the Sun has been a central topic of interest for philosophers, scientists and all people who wanted to know more about the Universe and Earth's position inside it. After centuries of astronomical observations that proved some basic but very important facts (like the one that the Earth is not flat and is orbiting around the Sun, not vice versa), with progress of telescopes the existence of outer layers of the Sun was revealed. First measurements in optical spectroscopy during second half of XIX and beginning of XX century explained their chemical structure and physical properties.

The 'surface' of the Sun, called photosphere, is $\sim 500km$ thick and radiates as a 'black body' at $T_{sun} \approx 5770K$. The chromosphere is the layer that extends from $500 - 2000km$ from the solar surface and spectroscopic measurements in this region (except at the lowest layers where was acknowledged that the temperature drops down to $\sim 4000K$) were possible only during eclipses due to weak radiation, so knowledge on the upper layers was quite limited for a very long time. It was only confirmed that above the chromosphere exists one more layer with very low particle densities, called solar corona, but its parameters were unknown.

The first measurement that required a fundamental explanation was the one performed by C. A. Young and W. Harkness during the 1869 total solar eclipse (which was visible from Alaska to North Carolina). They identified the strong $530.3nm$ green coronal line that has never been observed before. Since this line did not correspond to any known material, it was proposed that it was due to an unknown element, provisionally named coronium. Through many decades, great effort has been put by the space science community in order to explain this topic, until [Grotrian, 1939] concluded that non-equilibrium effects exist in the corona and, shortly after, the mystery was finally resolved when [Alfvén, 1941] proved that the corona is 'heated to an extremely high temperature'. Based on this work, [Edlén, 1943] has given an effective method of coronal spectral lines identification, detected lines of several highly ionized elements (iron, nickel, and calcium) and also recognized the famous $530.3nm$ line to originate from twelve times ionized iron. The ultraviolet emission from the corona was first detected with instruments built by [Baum et al., 1946] at the U.S. Naval Research Laboratory using captured German military V2

rockets, giving confirmation to the hypothesis of the hot corona.

All the information obtained about the corona were a step forward to explaining the stream of particles flowing outward from the Sun. Even though the existence of such a stream was first suggested by R. C. Carrington in 1859, the first simple physical model was given 100 years later by [Parker, 1958]. However, the solar wind has been finally confirmed by observations on Lunik 2 and Lunik 3 missions [Gringauz et al., 1960], after the Parker model was published. These results opened the interest for comprehensive in situ measurements of the solar wind plasma in order to obtain more information on the planetary medium and, as the ultimate goal, to understand heating mechanism of the corona and origins of the solar wind. After the pioneer mission of Mariner 2 in the solar wind five decades ago [Neugebauer and Snyder, 1966], many other successful missions (Helios, Ulysses, Wind, ACE, STEREO...) provided extensive measurements of in situ solar wind parameters. Results obtained by these missions improved our understanding of this medium and to related the interplanetary observations to the solar ones. However, even after half a century of research, the origin and acceleration of the solar wind are still not fully understood.

2.1.2 In situ measurements in the solar wind

The most important results of the in situ measurements are ion composition of the solar wind and properties of the VDF of each particle species. These measurements find the solar wind to be completely ionized plasma that dominantly contains protons and electrons coming from hydrogen and small percentage of fully ionized helium (α particles), making the interplanetary medium a faithful reflection of the coronal plasma. Ions of other elements (see e.g. [Bame et al., 1975, von Steiger et al., 2000]), solar or interstellar dust (see e.g. [Meyer-Vernet et al., 2009, Zaslavsky et al., 2012, Le Chat et al., 2013]), are observed only as isolated events and their influence on the bulk properties of the solar wind plasma is very small. Therefore, the dust and heavy ions will not be considered in this work.

The electron VDFs in the solar wind contain three components: the core, the halo, and the strahl. Core electrons with a speed smaller than the thermal speed v_{the}, are characterized by a bi-Maxwellian with an anisotropy at 1AU of $T_{||}/T_{\perp} = 1 - 1.5$, where parallel and perpendicular direction are defined with respect to the magnetic field.

The main two characteristics of the halo electrons are being isotropic and supra-thermal, forming a high-energy tail of the total electron distribution. At the orbit of the Earth, average values of the density and temperature ratio of the halo electrons to those of the core are $n_h/n_c \sim 0.05$ and $T_h/T_c \sim 6$. It is important to note that exact definition of T_h depends on the shape of this component which has been modeled in different ways by many authors. The natural path to use was modeling the non-thermal electrons with another Maxwellian or bi-Maxwellian distribution (see e.g. [Feldman et al., 1975, Gosling et al., 1987]). However, by careful examination of the particle analyzers data, it has been determined that the supra-thermal 'tails' of the VDF show a power low decrease toward higher velocities, rather than the exponential decrease characteristic for a Maxwellian. The power-low κ distribution model, initially proposed by [Scudder, 1992a, Scudder, 1992b] in order to explain the high temperature of the coronal plasma, was incorporated into the solar wind

models [Pierrard and Lemaire, 1996, Maksimović et al., 1997a], and application to Ulysses data showed somewhat better agreement than the two-Maxwellian model [Maksimović et al., 1997b]. Proprieties of the κ distributions will be explained in detail in Chapters 3 and 4.

The third population is the strahl. It is a sharply field-aligned beam, where the electron energy is comparable to that of the halo electrons. The largest importance of this VDF component is that, even though there is a very small fraction of 'beamed' electrons, they carry a significant portion of the total heat flux, which plays a key role in the solar wind acceleration [Zouganelis et al., 2004]. By investigating Helios, Wind, and Ulysses data, [Maksimović et al., 2005] showed that the strahl component is decreasing as we move away from the Sun as it is being scattered into the halo. The scattering mechanisms of the strahl electrons are still not well known and the adequate model that explains this topic is needed.

The comprehensive solar wind VDF model, which is widely accepted by the community, is given by [Štverak et al., 2009]. This model proposes bi-Maxwellian core, bi-κ halo and bi-κ beam-like strahl. The strahl component at 1AU is, in general, small compared to the halo and can be neglected when interpreting radio measurements [Couturier et al., 1981, Issautier et al., 1999, Salem et al., 2003]. This is why the strahl is not taken into account in this work. The entire distribution is shifted outwards from the Sun for a velocity v_{sw} which denotes the solar wind speed, highly varying in range $v_{sw} = 250 - 900 km/s$ in the Solar system. However, at the orbit of the Earth, there are mainly two types of wind: a fast wind of $v_{sw} \sim 700 - 800 km/s$, with a total electron density around $n_e \approx 2 - 3 cm^{-3}$, and 10% of α particles compared to protons, and a slow wind which has a speed around $v_{sw} \sim 350 - 400 km/s$ at 1 AU, slightly higher total electron density and a helium abundance which is reduced to $\sim 4\%$ [Matthias et al., 2001].

2.1.3 Solar wind theoretical models

Based on these observations multiple models have been developed in order to explain heating of the corona and acceleration of the solar wind (these two closely linked phenomena should not be treated separately). Hydrodynamic approach observes plasma as a fluid. This means that the plasma is in equilibrium and the VDF is Maxwellian, which is at the very start unrealistic for the solar wind. The first and most significant fluid model was the one by [Parker, 1958], already mentioned above, which explains the slow but not the fast fraction of the solar wind above $600 km/s$. There were multiple attempts to overcome this problem by generalization of the Parker's model to bi-fluids and multi-fluids [Sturrock and Hartle, 1966, Wolff et al., 1971] but macroscopic parameters obtained still do not fit well with the observations.

On the other hand, the exospheric approach, first introduced by [Chamberlain, 1960] assumes that above a critical level called exobase, the charged particles move freely without collisions along helicoidal trajectories determined by their energy and pitch angle. When the VDF of the particles is known at the exobase reference level and the system is described by the stationary version of the Vlasov equation, it can be calculated at any other point in the exosphere using Liouville theorem. This approach requires usage of the adequate electric field model. Namely, the electric flux of the electrons escaping the corona (which is proportional to the thermal speed of the electrons) is $\sqrt{m_p/m_e} \approx 43$ times larger than the proton flux, where m_p is the

proton mass. Hence to equilibrate the fluxes and to have no net current, an electric potential of the order of several hundred volts has to be constantly present in order to attract more electrons towards the Sun. The electric field associated to the latter potential will then 'push' the protons and accelerate the wind to its supersonic regime. The shape of the electric field was first proposed to be proportional to the gravitational potential [Pannekoek, 1922, Rosseland, 1924]. However, this field model is not realistic and does not explain the fast solar wind. More precise, but much more demanding when it comes to mathematics, approach to the problem is using the Vlasov equation with self-consistent electric field to describe the corona and the solar wind [Jockers, 1970, Lemaire and Scherer, 1971]. Even thought multiple upgrades to these models exist (see e.g. [Maksimović et al., 1997a, Meyer-Vernet and Issautier, 1998, Pierrard and Lemaire, 2001]), they neglect the fact that position of the exobase is not the same for different kinds of particles. The multi-exosphere model with different exobase positions that uses the Pannekoek-Rosseland electric field was proposed by [Brandt and Cassinelli, 1966] but making this kind of a general model with self-consistent field is the task that still has not been performed yet. A review of both fluid and kinetic models can be found in [Echim et al., 2011].

All the models described above give theoretical predictions of the conditions inside the corona as well as in the solar wind. Their full verification and development to a higher level can be done only by probing the solar wind origin region and performing in situ measurements there for comparison. However, particle analyzer measurements have shown multiple difficulties due to the spacecraft potential [Scudder et al., 2000, Kellogg et al., 2009, Pulupa et al., 2014], not being able to measure during extreme events [Liu et al., 2014] or even systematically malfunctioning [Fedorov et al., 2011]. This is why the QTN spectroscopy [Meyer-Vernet, 1979] in radio domain is used as an alternative way to measure plasma VDF moments. The QTN (excluding the shot noise) is almost completely independent of the potential [Meyer-Vernet and Perche, 1989] and has multiple advantages for both quick and precise diagnostics that will be explained throughout following chapters. This is why the methods that will be presented here are routinely used on various missions (Section 2.5) and will be the important part of science on the Solar Probe Plus [Bale et al., 2016] - the spacecraft aimed to make in situ measurements inside the corona, down to 9 solar radii from the photosphere, in the years to come.

2.2 Phenomena of the quasi-thermal noise

When electric antenna is immersed into a plasma and connected to a sensitive wave receiver it is able to detect electromagnetic fluctuations due to the thermal motion of plasma electrons and ions. These fluctuations are measured at the antenna terminals as a noise that is dominant in the frequency range comparable to the plasma frequency.

In order to understand the nature of this phenomenon we will consider an idealized case of the spherical dipole antenna that does not perturb the surrounding plasma. Sufficient conditions for the plasma to stay nearly homogeneous near the antenna are that the antenna radius a is much smaller then the plasma Debye length L_D and that the antenna potential is not large compared to the particles thermal energy [Laframboise, 1966, Meyer et al., 1974].

At this oversimplified, heuristic approach, we will consider the signal as a sum

of uncorrelated events, each one coming from a single particle. We also neglect temporal dispersion, limiting our derivation only to very low frequencies and assume a long dipole $L >> L_D$ so that two spheres receive uncorrelated signals.

Consider at first a single particle that passes near the antenna within the distance $r \leq L_D$. This event has a duration $\tau_1 \sim 2L_D/v_{the}$ and induces a voltage inside the antenna in the order of

$$V_1 \approx \frac{e}{4\pi\epsilon_0 r}$$

The Fourier transform of a single event for $\omega\tau_1 << 1$ is simply $V_1(\omega) \approx \tau_1 V_1$. If the plasma is in thermal equilibrium then we have $N_1 = 2\pi^{1/2} n_e v_{the}$ uncorrelated events. The power spectral density (PSD) is given as $V^2 \approx 2N_1|V_1(\omega)|^2$ [Meyer-Vernet, 1983] (here, the factor 2 comes from the symmetry of positive and negative frequencies), yielding

$$V^2[V^2/Hz] \approx \frac{m_e v_{the}}{\pi^{3/2}\epsilon_0} \approx 9.5 \cdot 10^{-17} T^{1/2}[^\circ K]$$

which is actually not far from the low frequency result derived by more precise calculations [Meyer-Vernet and Perche, 1989].

Although the derivation shown above is simple and gives decent estimation for spherical antenna at low frequencies it is not correct for cylindrical antennas that are used more often in space instrumentation. Also, the result breaks down at $\omega \geq \omega_p$ as the temporal dispersion becomes important. In order to discover the general noise properties it is necessary to perform the accurate calculation given below.

2.3 Modeling the response of an electric dipole antenna

After understanding the noise received by an antenna on a simple, phenomenological level, we will develop more precise calculations. Thermal motion of the charged particles generates fluctuating electric field and, if the antenna is immersed in the plasma, this field will induce the voltage fluctuations measurable at the antenna terminals through the mechanism briefly described above. The objective of the QTN spectroscopy is to determine the plasma VDF characteristics (density, temperature, fraction of the supra-thermals, drift velocity...) from the measured power spectrum. From this statement it is clear that both the antenna and the plasma properties will influence the spectrum.

In this Section we explore the nature of the QTN measurements in the solar wind, illustrating how the antenna signal and the fields generated by the plasma are connected. Further on, we investigate the antenna influence on the spectrum and characteristics necessary for interpretation of the measurements.

2.3.1 Voltage power spectral density measured in response to a fluctuating electric field

In order to calculate the PSD we will assume an ideal antenna made of thin mesh wires, considering that charged particles can freely penetrate through it while

the electric field inside the antenna is equal to zero (the so-called 'grid antenna' approximation). Real antennas don't have these properties so the calculations of the QTN will have to be corrected due to the antenna thickness later on (Section 2.4.3).

Random motion of the charged particles, that is described by velocity distribution $f(\vec{v})$ produces a current $\vec{j_p}$ in the plasma. This current produces a random electric field $\vec{E}$ in both antenna and the plasma. Under influence of this field the current, described by the current distribution $\vec{j_a}$, is induced inside the receiving antenna.

From here we can calculate the the tip-to-tip potential difference V_0 on each of the antenna thin wires in an open circuit (Figure 2.1) using the 'induced electromotive force method' (see e.g. [Schiff, 1970]). The power delivered to the antenna is equal to

$$\int \vec{E} \cdot \vec{j_a} d\vec{r}$$

where integration is performed over the antenna volume. On the other hand, the same quantity is given as the product of V_0 and the current intensity at the antenna terminals I_a, so we can write

$$V_0 = \int \vec{E} \cdot \frac{\vec{j_a}}{I_a} d\vec{r} \tag{2.1}$$

Equation 2.1 provides a very important conclusion that the electric potential difference between the two antenna arms V_0 caused by the random plasma currents can be determined by knowing the properties of the random electric field in the absence of the antenna and the normalized antenna current distribution $\vec{j_a}/I_a$. The formal proof of this statement requires using the Lorentz reciprocity theorem in the limit of thin wires and is given by [Fejer and Kan, 1969].

However, since the quantity measured by a radio receiver is the PSD, we need to link it with the voltage that appears on the terminals. This can be done using Wiener-Khintchine theorem that gives the power spectrum as Fourier transform of autocorrelation function of the voltage

$$V_0^2(\omega) = \int < V_0(t_1) V_0(t_1 + t) > e^{i\omega t} dt \tag{2.2}$$

The autocorrelation of the antenna voltage is [Meyer-Vernet, 1979]

$$< V_0(t_1) V_0(t_2) >= I_a^{-2} \int \int \vec{j_{ai}}(\vec{r_1}) < \vec{E_i}(\vec{r_1}, t_1) \vec{E_j}(\vec{r_2}, t_2) > \vec{j_{aj}}(\vec{r_2}) d\vec{r_1} d\vec{r_2} \tag{2.3}$$

The power spectrum is then directly

$$V_0^2(\omega) = \frac{2}{(2\pi)^3 I_a^2} \int \vec{j_{ai}}(\vec{k}) < \vec{E_i}(\vec{k}, \omega) \vec{E_j^*}(\vec{k}, \omega) > \vec{j_{aj}}^*(\vec{k}) d\vec{k} \tag{2.4}$$

where we have defined Fourier transforms

$$\vec{j_a}(\vec{k}) = \int \vec{j_a}(\vec{r}) e^{-i\vec{k}\cdot\vec{r}} d\vec{r} \tag{2.5}$$

$$< \vec{E}_i(\vec{k},\omega)\vec{E}_j^*(\vec{k},\omega) >= \int\int < \vec{E}_i(\vec{r_1},t_1)\vec{E}_j^*(\vec{r_1}+\vec{r},t_1+t)d\vec{r} > e^{i(\omega t-\vec{k}\cdot\vec{r})}d\vec{r}dt \quad (2.6)$$

From Equation 2.4 it is clear that we need to calculate the Fourier transform of the antenna current distribution (Section 2.3.3) as well as mean squared value of the electric field fluctuations in order to obtain the noise spectrum.

2.3.2 Measurements in open circuit - antenna gain

The theory given throughout this Chapter is devoted to calculating the PSD $V_0^2(\omega)$ that is induced by different plasma particle populations. However, this quantity, defined by Equation 2.4, is related to the electrostatic potential difference between the tips of the antenna mesh wires (Figure 2.1), while we are only able to measure it at the antenna terminals. The relation between theoretically calculated and measured power spectrum is

$$V_{obs}^2 = \Gamma^2 V_0^2 + V_r^2 \quad (2.7)$$

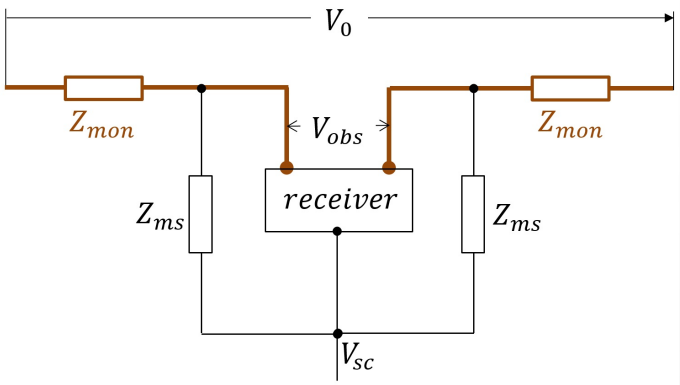

Figure 2.1: Schema of the dipole antenna. In general, for both dipole and monopole mode the voltage needs to be measured between one arm and the spacecraft potential V_{sc} (see e.g. [Bougeret et al., 1995]). Then, for dipole antenna (investigated in this work) two values are subtracted to obtain the difference of two signals. It is worth noting that this Figure is applicable not only to wire dipoles, but to any antenna shape that satisfies approximations given in Section 2.3.1

Here, V_r^2 is the receiver internal noise, usually measured in laboratory before the mission (although the laboratory measurements of V_r^2 are not always useful in the space due to various effects of the spacecraft payload itself). The antenna gain Γ is, from Figure 2.1

$$\Gamma = \frac{Z_{ms}}{Z_{mon}+Z_{ms}} \quad (2.8)$$

The total 'stray' impedance of a monopole is actually combined base impedance (impedance of the enclosure to the spacecraft body) and preamplifier input impedance, along with some contribution from the cable connections. For measurements in

dipole mode, it is convenient to express the antenna gain given in Equation 2.8 in terms of the impedance of dipole antenna Z_{ant}. Since $Z_{ant} = 2Z_{mon}$ and $Z_{stray} = 2Z_{ms}$ (see e.g. [Bale et al., 2008]) we can write

$$\Gamma = \frac{Z_{stray}}{Z_{ant} + Z_{stray}} \tag{2.9}$$

At the frequencies comparable to the plasma frequency in the solar wind, Equation 2.9 can be reduced to (see e.g. [Bougeret et al., 1995, Gurnett et al., 2004, Bale et al., 2008])

$$\Gamma = \frac{C_{ant}}{C_{ant} + C_{stray}} \tag{2.10}$$

This is the expression for the antenna gain used further on. From the Equation 2.10 it is noticeable that the attenuation factor of the signal depends on the relation between the antenna and stray capacitance. It is desirable for C_{stray} to be as small as possible so the gain can be close to unity because, as value of the gain decreases, the signal given by Equation 2.7 will be more and more affected by the internal noise V_r^2. This is difficult to achieve in space missions and we usually have $C_{stray} = 20 - 50pF$.

For a wire dipole antenna with L_{ant} and a_{ant} being the length and radius of one arm, the capacitance can be well approximated at low frequencies as

$$C_{ant}(\omega < \omega_p) = \frac{\pi\epsilon_0 L_{ant}}{ln(L_D/a_{ant})} \tag{2.11}$$

provided that $L_{ant} > L_D$. In the opposite case ($L_{ant} < L_D$), the expression is more complicated to evaluate, but a good approximation is the value which is also viable at the high frequency limit, given as

$$C_{ant}(\omega > \omega_p) = \frac{\pi\epsilon_0 L_{ant}}{ln(L_{ant}/a_{ant}) - 1} \tag{2.12}$$

As in the solar wind we have $L_{ant} = 5 - 50m$, $a_{ant} = 0.02 - 2cm$ and $L_D = 3 - 10m$ the characteristic values of the capacitance are in the range $C_{ant} = 30 - 90pF$, causing the gain to be $\Gamma = 0.4 - 0.85$.

For double spheres we have

$$C_{ant} = 2\pi a\epsilon_0 \tag{2.13}$$

where a is radius of the sphere. These results are given in more detail by [Meyer-Vernet and Perche, 1989], while some aspects of the antenna capacitance near the plasma frequency are given in Section 5.1.4.

2.3.3 Antenna current and response function

As demonstrated in Section 2.3.1, the response of an antenna to plasma waves is strongly dependent on the antenna size and geometry through the current density $\vec{j_a}(\vec{k})$. It can be expressed in terms of the so-called antenna response function. Here we derive this function for wire and sphere dipole antennas, along with some remarks for other geometries.

Wire dipole

A dipole made of two wires (we assume that the gap between the two antenna arms is very small) is a conductor that contains charges free to move along the antenna. For the case of electromagnetic radiation in vacuum, the current distribution for both transmitting and receiving antenna was calculated by many authors (see e.g. [Schelkunoff and Friis, 1952, Balanis, 1997, Zhong et al., 2008]) and the result obtained is a standing wave pattern which is sinusoidal with nulls at the tips and period $\lambda = c/f$ (where c is the speed of light and $f = \omega/2\pi$). This solution can be simplified when we observe the frequency range up to $\sim 100kHz$ since the value of λ is of the order of several kilometers. In this case we have $\lambda >> L_{ant}$ and $\sin(kL_{ant}) \approx kL_{ant}$ so the sinusoidal form can be replaced with the triangular one (this assumption is equivalent to consideration of the linear charge density to be constant along the antenna arms).

On the other hand, if the receiving antenna is immersed in a plasma, it will observe the waves with $kL_{ant} \sim 1$. When observing this range of wavenumbers, the contribution of the surface waves needs to be taken into account [Meyer et al., 1974] and the current distribution can, in general case, become very complicated. However, the calculation valid for a wire dipole in the interplanetary medium (where the antenna can be treated as a thin infinite cylinder of radius $a_{ant} << L_D$) was performed by [Couturier et al., 1981] who showed that the correction due to surface waves is negligible and the hypothesis of the triangular current is justified. Therefore, we will use the triangular approximation in the following of this thesis. For a dipole along the z axis we have

$$\int \vec{j_a}(\vec{r})d\vec{r} = I_a(1 - |z|/L_{ant})\vec{e_z} \tag{2.14}$$

where $\vec{e_z}$ is the unity vector. The Fourier transform of the current given in Equation 2.14 along both of the antenna arms is, following Equation 2.5

$$\vec{j_a}(\vec{k}) = \int_{-L_{ant}}^{L_{ant}} I_a(1 - |z|/L_{ant})e^{ik_z z}dz\vec{e_z} = \frac{4I_a}{k_z^2 L_{ant}} \sin^2\left(\frac{k_z L_{ant}}{2}\right)\vec{e_z} \tag{2.15}$$

Defining the antenna response function as

$$F(k) = \frac{1}{32\pi}\int \frac{|\vec{k}\cdot\vec{j_a}(\vec{k})|^2}{I_a^2}d\Omega \tag{2.16}$$

putting Equation 2.15 into Equation 2.16 and integrating over the entire solid angle Ω, we obtain an integral of the form

$$F(kL_{ant}) = \int_{-1}^{1} \frac{\sin^4(kL_{ant}u/2)}{k^2 L_{ant}^2 u^2}du \tag{2.17}$$

This integration has been performed by [Kuehl, 1966], giving the result

$$F(x) = x^{-1}\left[Si(x) - \frac{1}{2}Si(2x) - \frac{2}{x}\sin^4\frac{x}{2}\right] \tag{2.18}$$

which is the antenna response function for an infinitely thin wire dipole ($Si(x)$ stands for the sine integral). For small or large values of the argument $x = kL_{ant}$ the wire dipole response function given in Equation 2.18 can be approximated by

$$F(x \to 0) = \frac{x^2}{24} \tag{2.19}$$

$$F(x \to \infty) = \frac{\pi}{4x} \tag{2.20}$$

The function $F(x)$ and its approximations given by Equations 2.19 and 2.20 are shown on Figure 2.2.

Taking into account the finite antenna radius a_{ant} adds a factor of $J_0(k_r a_{ant})$ [Schelkunoff and Friis, 1952, Balanis, 1997] where J_0 is the zero-order Bessel function of the first kind and k_r is the component of the wave vector perpendicular to z axis. As will be explained below, for real antennas used in space missions ($L_{ant}/a_{ant} \sim 10^3 - 10^4$), this factor in the computation of the QTN makes negligible difference if $L_{ant} >> L_D$ (long dipole) and can be neglected for simplicity. On the other hand, for short dipole the Bessel factor needs to be incorporated into Equation 2.18 to give

$$F(x) = x^{-1}\left[Si(x) - \frac{1}{2}Si(2x) - \frac{2}{x}\sin^4\frac{x}{2}\right]J_0^2(k_r a_{ant}) \tag{2.21}$$

which is the general expression used to calculate the theoretical spectrum of the aligned wire dipole antenna.

If the antenna arms are not aligned then we need to observe the current on each arm separately. If we have antenna in the xy plane where one arm is along x axis then, by analogy with the Equation 2.15, we have

$$\vec{j_a}(\vec{k}) = \left(\frac{i}{k_x} + \frac{1 - e^{ik_x L_{ant}}}{k_x^2 L_{ant}}\right)\vec{e_x} - \left(\frac{i}{k_r} + \frac{1 - e^{ik_r L_{ant}}}{k_r^2 L_{ant}}\right)\vec{e_r} \tag{2.22}$$

with $\vec{e_r} = \vec{e_x}e^{i\psi}$ and ψ being the angle between the antenna arms. Of course, for $\psi = \pi$ we have the linear dipole, returning to Equation 2.15.

The integration of Equation 2.22 to obtain the antenna response function is not easy to perform. However, [Meyer-Vernet and Perche, 1989] showed that, if the dipole is long ($L_{ant} >> L_D$), it can be replaced by Equation 2.18 since the mean distance between the antenna arms is large and they observe uncorrelated signals (except for $\omega \approx \omega_p$) effectively in the same way as if they were collinear. On the other hand, for a short dipole ($L_{ant} << L_D$), L_{ant} can be, in the first approximation, replaced by the antenna effective length

$$L_{eff} = \sin(\psi/2)L_{ant} \tag{2.23}$$

making a considerable simplification, used in Chapter 4.

This work deals with the wire dipole antennas described here, while some remarks about spherical dipoles, that are another commonly used antenna geometry, are given for the sake of completeness.

Double sphere

For a spherical monopole that consists of two spheres of radius $a << L_D$, separated by $L >> a$ along the z axis we consider an uniform current distribution over its entire surface (see e.g. [Meyer-Vernet, 1983])

$$\int \vec{j_a}(\vec{r})d\vec{r} = \frac{I_a}{4\pi a^2}\delta(|\vec{r} - L\vec{e_z}| - a)\vec{e_z} \tag{2.24}$$

and, performing the same procedure as for a wire antenna, we have [Meyer-Vernet and Perche, 1989]

$$\vec{j_a}(\vec{k}) = -i\frac{2I_a}{k_z}\sin\left(\frac{k_z L}{2}\right)\frac{\sin(ka)}{ka}\vec{e_z} \tag{2.25}$$

and, using the Equation 2.16 we obtain

$$F(x) = \frac{1}{4}\left(1 - \frac{\sin x}{x}\right)\frac{\sin^2(x\frac{a}{L})}{x^2\frac{a^2}{L^2}} \tag{2.26}$$

denoting the antenna response function of a dipole made of two small spheres. For small or large arguments this function can be approximated (considering $a \to 0$) as

$$F(x \to 0) = \frac{x^2}{24} \tag{2.27}$$

which is the same value as the one for a wire dipole and

$$F(x \to \infty) = \frac{1}{4} \tag{2.28}$$

The function given by Equation 2.26 and approximations given by Equations 2.27 and 2.28 are given on Figure 2.2.

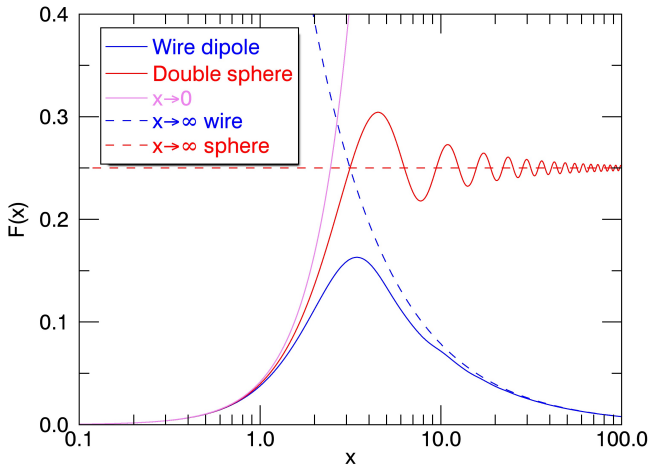

Figure 2.2: Antenna response function and its approximations for wire dipoles and double spheres

2.4 Thermal fluctuations of the electric field in a plasma measured by the antenna

As explained above, the tensor in Equation 2.4 describes the influence of plasma to the noise spectrum. Here, we explore the contributions from both electrons and protons to the fluctuating electric field and, consequently, to the signal measured by a 'grid' antenna. The correction due to the finite antenna thickness, valid below the plasma frequency, is calculated in Section 2.4.3.

2.4.1 Voltage fluctuations induced by the motion of electrons

When investigating the electrostatic noise produced by the electron motion, we look at frequencies sufficiently high to neglect ion motion so that the ions act as an uniform background of a positive charge. Under this assumption, the autocorrelation tensor of the electric field in an isotropic, unmagnetized plasma is given as (see e.g. [Fejer and Kan, 1969])

$$< \vec{E_i}(\vec{k},\omega)\vec{E_j^*}(\vec{k},\omega) >= \frac{2\pi n_e e^2}{\epsilon_0^2 k^2}\int d\vec{v} f_0(v)\delta(\omega-\vec{k}\cdot\vec{v}) \left[\frac{k_i k_j}{k^2|\epsilon_L(k,\omega)|^2}+\frac{1}{2}\Big(\delta_{ij}-\frac{k_i k_j}{k^2}\Big)|\vec{k}\times\vec{v}|^2\frac{\omega^2}{k^4c^4|\epsilon_T(k,\omega)|^2}\right] \quad (2.29)$$

where we introduce longitudinal and transverse dielectric permittivity as

$$\epsilon_L(k,\omega) = 1+\frac{\omega_p^2}{k^2}\int\frac{\vec{k}\cdot(\partial f_0(\vec{v})/\partial\vec{v})}{\omega-\vec{k}\cdot\vec{v}}d\vec{v} \quad (2.30)$$

$$\epsilon_T(k,\omega) = 1-\frac{\omega^2}{k^2c^2}+\frac{\omega\omega_p^2}{k^2c^2}\int\frac{f_0(v)}{\omega-\vec{k}\cdot\vec{v}}d\vec{v} \quad (2.31)$$

From Equation 2.29 we conclude that the electric field tensor is completely determined by characteristics of the VDF. Putting Equation 2.29 into Equation 2.4 gives

$$V_0^2(\omega) = \frac{n_e e^2}{2\pi^2 I_a^2\epsilon_0^2}\int f_0(v)\delta(\omega-\vec{k}\cdot\vec{v}) \left[\frac{|\vec{k}\cdot\vec{j_a}(\vec{k})|^2}{k^4|\epsilon_L(k,\omega)|^2}+\frac{1}{2}\left(|\vec{j_a}(\vec{k})|^2-\frac{|\vec{k}\cdot\vec{j_a}(\vec{k})|^2}{k^2}\right)\frac{\omega^2|\vec{k}\times\vec{v}|^2}{k^6c^4|\epsilon_T(k,\omega)|^2}\right]d\vec{k}d\vec{v} \quad (2.32)$$

which, combined with Equation 2.7, gives the expression for electrostatic noise measured at the antenna terminals, dependent only of the electron VDF of particles and antenna properties. This result is very general and can be considerably simplified for usage in space plasmas.

First of all, since for $v_{the} << c$ the term that originates from transverse waves and scales with $(\omega/kc)^2$ is negligible, it can be omitted. This is the case for both solar wind and planetary magneto and ionospheres. Considering only longitudinal waves, Equation 2.32 gains the much simpler form

$$V_0^2(\omega) = \frac{n_e e^2}{2\pi^2 I_a^2 \epsilon_0^2} \int B(\vec{k}) \frac{|\vec{k} \cdot \vec{j_a}(\vec{k})|^2}{k^4 |\epsilon_L(k,\omega)|^2} d\vec{k} \tag{2.33}$$

with

$$B(\vec{k}) = \int f_0(v) \delta(\omega - \vec{k} \cdot \vec{v}) d\vec{v} \tag{2.34}$$

and we can rewrite Equation 2.33 as

$$V_0^2(\omega) = \frac{16 m_e \omega_p^2}{\pi \epsilon_0} \int_0^\infty \frac{B(k) F(kL)}{k^2 |\epsilon_L(k,\omega)|^2} dk \tag{2.35}$$

The antenna response function $F(kL)$ is defined by Equation 2.16. For two most common antenna geometries, wire dipole and double sphere, it is given, to a good approximation, by Equations 2.21 and 2.26, respectively. Using the VDF isotropy we can rewrite Equation 2.34 as

$$B(k) = \frac{2\pi}{k} \int_{\omega/k}^\infty v f_0(v) dv \tag{2.36}$$

The noise expression in the form given in Equation 2.35 is very convenient for practical usage since it contains only one-dimensional numerical integration with k^{-2} factor and function $F(kL)$ that has a power-law decrease (wires, Equation 2.20) or tends to the constant value (spheres, Equation 2.28), while from Equation 2.30 we see that $|\epsilon_L(k,\omega)|^2 \to 1$ for high values of k. This is the expression used for calculation of the antenna signal induced by electrons further on.

Maxwellian electrons - thermal noise

For exploring the noise spectra in space plasmas it is first needed to understand the properties of a single Maxwellian noise. From definition of the normalized VDF

$$f_0(v) = \frac{e^{-\frac{v^2}{v_{the}^2}}}{\pi^{3/2} v_{the}^3} \tag{2.37}$$

where $v_{the} = \sqrt{2 k_b T_e / m_e}$, we can calculate the function $B(k)$ using Equation 2.36 as

$$B(k) = \frac{e^{-\frac{\omega^2}{k^2 v_{the}^2}}}{\pi^{1/2} k v_{the}} \tag{2.38}$$

The longitudinal dielectric permittivity of a Maxwellian plasma can be found from Equation 2.30, giving the well known result (see e.g. [Fitzpatrick, 2014])

$$\epsilon_L(k,\omega) = 1 + \frac{1}{k^2 L_D^2} \Big[1 + \frac{\omega}{k v_{the}} Z_0 \Big(\frac{\omega}{k v_{the}} \Big) \Big] \tag{2.39}$$

where $L_D = v_{the} / 2^{1/2} \omega_p$ and Z_0 is the plasma dispersion function [Fried and Conte, 1961]. From here we can calculate the thermal noise spectrum using Equation 2.35.

At this point, an important relation between the antenna resistance and PSD can be made for Maxwellian plasma. Using the method similar to the one presented in Section 2.3.1 [Schiff, 1970] calculated the antenna impedance to be

$$Z_{ant}(\omega) = \frac{2i}{(2\pi)^3 I_a^2 \epsilon_0 \omega} \int \frac{|\vec{k} \cdot \vec{j_a}(\vec{k})|^2}{k^2 \epsilon_L(k,\omega)} d\vec{k} \tag{2.40}$$

This expression can be rewritten using Equation 2.16 as

$$Z_{ant}(\omega) = \frac{4i}{\pi^2 \epsilon_0 \omega} \int_0^\infty \frac{F(kL_{ant})}{\epsilon_L(k,\omega)} dk \tag{2.41}$$

and expression for the antenna resistance $R_{ant}(\omega) = Re[Z_{ant}(\omega)]$ is directly

$$R_{ant}(\omega) = -\frac{4}{\pi^2 \epsilon_0 \omega} Im\left[\int_0^\infty \frac{F(kL_{ant})}{\epsilon_L(k,\omega)} dk\right] \tag{2.42}$$

where the term $Im[\epsilon_L^{-1}(k,\omega)]$ appears. Knowing that, for real arguments x, $Im[Z_0(x)] = \pi^{1/2} e^{-x^2}$, we obtain from Equation 2.39

$$Im[\epsilon_L^{-1}(k,\omega)] = -\frac{2\pi^{1/2}\omega_p^2}{k^3 |\epsilon_L(k,\omega)|^2} \frac{\omega}{v_{the}^3} e^{-\frac{\omega^2}{k^2 v_{the}^2}} \tag{2.43}$$

Using $Im[\epsilon_L^{-1}(k,\omega)] = -Im[\epsilon_L(k,\omega)]/|\epsilon_L(k,\omega)|^2$ and combining Equations 2.35 and 2.42 gives

$$V_0^2(\omega) = 4 k_b T_e R_{ant}(\omega) \tag{2.44}$$

which is actually the Nyquist theorem [Nyquist, 1928], satisfied in the thermal equilibrium. An important characteristic of the power spectrum given by Equation 2.35 is the existence of the so-called 'plasma peak' near the plasma frequency where the real part of $\epsilon_L(k,\omega)$ has a minimum. Several examples of thermal noise spectra are given on Figure 2.3, clearly showing that the peak is more noticeable if dipoles are longer.

Rough estimation of the peak intensity can be given in a following way. As the antenna response has the highest value for $k \sim L_{ant}^{-1}$ (so waves with the wavelength $\sim L_{ant}$ are highly preferred) then for $L_{ant} >> L_D$ we can develop the permittivity expression given in Equation 2.39 for $\omega >> k v_{the}$ (see Chapter 5 for details) as

$$\epsilon_L(kL_D << 1, \omega \geq \omega_p) = 1 - \frac{\omega_p^2}{\omega^2 - 3k^2 v_{the}^2/2} \tag{2.45}$$

This approximation is not valid below the plasma frequency while for $\omega \approx \omega_p$ it can be reliably used only for very long dipoles ($L_{ant}/L_D \geq 10$) [Kuehl, 1967]. Using Equation 2.45, the integral in Equation 2.42 can be calculated analytically, giving

$$R_{ant}(\omega) = \frac{2F(k_* L_{ant})}{3\pi \epsilon_0 \omega L_D^2 k_*} \tag{2.46}$$

with

$$k_* = \frac{1}{L_D} \sqrt{\frac{1}{3}\left(\frac{\omega^2}{\omega_p^2} - 1\right)} \tag{2.47}$$

From here we can estimate the peak intensity for $L_{ant} >> L_D$ by examining the maximum of $F(k)/k$. The calculation was done by [Meyer-Vernet and Perche, 1989] giving

$$V^2(\omega_{peak})[V^2/Hz] \approx 2 \cdot 10^{-17} T^{1/2}[^\circ K] \frac{L_{ant}}{L_D} \tag{2.48}$$

Therefore we can see from Equation 2.48 that the peak amplitude increases linearly with L_{ant}/L_D. In a similar fashion, we can find

$$\frac{\omega_{peak}}{\omega_p} \approx 1 + 8\frac{L_D^2}{L_{ant}^2} \tag{2.49}$$

Equation 2.49 gives quick estimation of the plasma density from position of the peak. The changes in the plasma peak with L_{ant}/L_D (and approximations given by Equations 2.48 and 2.49) are illustrated on Figure 2.3. The error made by these approximative expressions is less than 30% for $L_{ant}/L_D > 7$ [Meyer-Vernet and Perche, 1989].

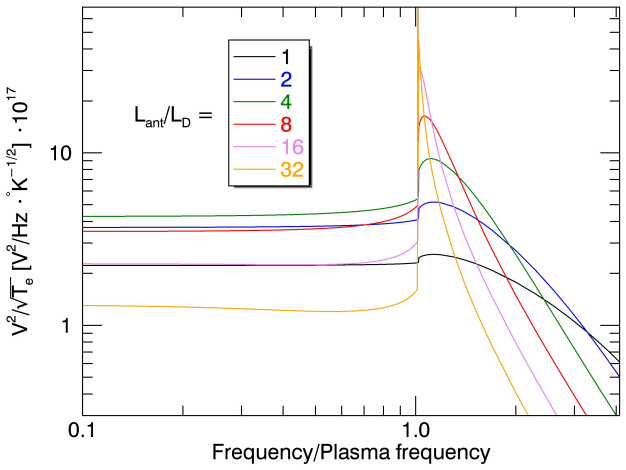

Figure 2.3: Normalized electron thermal noise spectrum received by a wire dipole antenna for different values of L_{ant}/L_D

Enhancement of the noise by the non-thermal electrons - quasi-thermal noise

Since non-thermal VDFs are ubiquitous in the solar wind, in this paragraph we examine the effect of fast electrons to the measured power spectrum. In order to illustrate the quasi-thermal contribution to the noise we will use example of the two-Maxwellian VDF.

If we have two Maxwellian electron populations - thermal 'core' and supra-thermal 'halo', then we have

$$\epsilon_L(k,\omega) = 1 + \sum_{s=c,h} \frac{1}{k^2 L_{Ds}^2} \left[1 + \frac{\omega}{k v_{thes}} Z_0\left(\frac{\omega}{k v_{thes}}\right) \right] \tag{2.50}$$

and

$$B(k) = \sum_{s=c,h} \frac{e^{-\frac{\omega^2}{k^2 v_{thes}^2}}}{\pi^{1/2} k v_{thes}} \tag{2.51}$$

By analogy with the procedure from the previous paragraph we can write

$$Im[\epsilon_L(k,\omega)] = Im[\epsilon_{Lc}(k,\omega)] + Im[\epsilon_{Lh}(k,\omega)] = \frac{2\pi^{1/2}\omega}{k^3} \sum_{s=c,h} \frac{\omega_{ps}^2}{v_{thes}^3} e^{-\frac{\omega^2}{k^2 v_{thes}^2}} \tag{2.52}$$

and, putting Equations 2.51 and 2.52 into Equation 2.35 we obtain, after few simple transformations

$$V_0^2(\omega) = 4k_b T_c \frac{4}{\pi^2 \epsilon_0 v_{thec}} \int \frac{dz_c}{z_c^2} \frac{F(k)}{|\epsilon_L(k,\omega)|^2} \left(Im[\epsilon_{Lc}(k,\omega)] + \frac{T_h}{T_c} Im[\epsilon_{Lh}(k,\omega)] \right) \tag{2.53}$$

where $z_c = \omega / k v_{thec}$. On the other hand, [Couturier et al., 1981] calculated the resistance of the antenna in a double Maxwellian plasma to be

$$R_{ant}(\omega) = -\frac{4}{\pi^2 \epsilon_0 v_{thec}} \int \frac{dz_c}{z_c^2} F(k) Im[\epsilon_L^{-1}(k,\omega)] \tag{2.54}$$

In order to distinguish the double Maxwellian plasma behavior from the thermal plasma given by Equation 2.44 we can compare the integrands from Equations 2.53 and 2.54. After replacing Equation 2.52, we have

$$\frac{Im[\epsilon_{Lc}(k,\omega)] + \frac{T_h}{T_c} Im[\epsilon_{Lh}(k,\omega)]}{Im[\epsilon_{Lc}(k,\omega)] + Im[\epsilon_{Lh}(k,\omega)]} = 1 + \frac{t-1}{1 + \frac{t^{3/2}}{n} e^{\frac{\omega^2}{k^2 v_{theh}^2} - \frac{\omega^2}{k^2 v_{thec}^2}}} \tag{2.55}$$

where $t = T_h/T_c >> 1$ and $n = n_h/n_c << 1$. We assume that ratio of the integrals is similar to the ratio of the integrands. This is a very rough approximation but can be used here for a quick estimation since both integrands are similarly shaped, positive on the entire domain and their derivatives are not different for more then a factor T_h/T_c.

For low frequencies, the exponential part in the denominator tends to unity, making the denominator on the right-hand side of Equation 2.55 to be approximately equal to $t^{3/2}/n >> t-1$. This implies that the integrands have the same value in this approximation, bringing us back to the Nyquist theorem. From here we make an important conclusion that, at low frequencies, the noise signal scales as $V_0^2(\omega \to 0) \sim T_c^{1/2}$. This is clearly visible on Figure 2.4, where the low frequency part remains unchanged even though the supra-thermal population parameters are varied.

If frequency is close to the plasma frequency, we can make use of the fact that, in the solar wind, $n << 1$ so we have $\omega_p^2 \approx \omega_{pc}^2$. Knowing this, for $\omega \to \omega_p$ we can approximate the exponential term in Equation 2.55 to be

$$e^{\frac{\omega^2}{k^2 v_{theh}^2} - \frac{\omega^2}{k^2 v_{thec}^2}} \approx e^{-\frac{t-1}{2tk^2 L_{Dc}^2}}$$

In the QTN spectroscopy we are mostly interested in the long dipole antennas. As was noted above, the antenna highly favors wavelengths for which $k \sim L_{ant}^{-1}$. This implies that, for $L_{ant} >> L_D$ the factor $k^2 L_{Dc}^2$ can be considered small, making the denominator of the Equation 2.55 very close to unity. Consequently, ratio of the integrands for $\omega \approx \omega_p$ is approximately equal to the temperature ratio, not dependent on the integration variable z_c, so we have

$$\frac{V_0^2(\omega \approx \omega_p)}{4k_b T_c R_{ant}(\omega \approx \omega_p)} \sim \frac{T_h}{T_c} \tag{2.56}$$

showing that the enhancement of the PSD close to the plasma frequency is proportional to T_h/T_c. We conclude that the increase in the noise signal for non-thermal VDFs around the plasma frequency is not matched by the increase in the antenna resistance, justifying the name 'quasi-thermal noise' (we will use the notation $V_{qtn}^2 = V_0^2$ further on). The more exact analysis give the same enhancement factor (see e.g. [Perkins and Salpeter, 1965, Fejer and Kan, 1969]). The effect of the supra-thermal electrons on the QTN spectrum, calculated using Equation 2.35, can be observed on Figure 2.4 by comparing the peak noise intensity with the one at low frequencies.

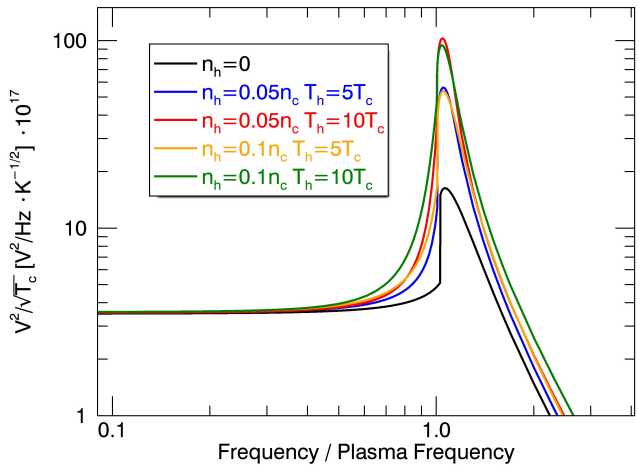

Figure 2.4: QTN spectra at the wire dipole antenna in a double Maxwellian plasma with different characteristics of core and halo populations. Plots are normalized to the same core temperature and $L_{ant}/L_{Dc} = 8$

Basic properties of the QTN spectrum

It is noticeable from both Figures 2.3 and 2.4 that, if the antenna length is larger then the Debye length, three spectral regions exist - the flat spectrum below the plasma frequency, the 'plasma peak' at $\omega \approx \omega_p$ and the high frequency part with clear power-law decrease.

As discussed above, the way plasma affects the electric field is described by the dielectric permittivity function $\epsilon(k, \omega)$, and for a frequency range around the plasma frequency, it is enough to observe only its longitudinal component $\epsilon_L(k, \omega)$.

For $\omega < \omega_p$, it can be easily shown that $\epsilon_L \to 1+k^{-2}L_D^{-2}$ as the plasma behavior is determined by the Debye shielding, making the spectrum flat in this frequency range. This result is somewhat expected since the Debye shielding causes the antenna to observe only fluctuations within the distance proportional to L_D. Another important characteristic shown above is that the spectrum is dominantly determined by the thermal component, so we have $V_{qtn}^2 \sim T_c^{1/2}$.

On the other hand, for $\omega \sim \omega_p$ the permittivity has a sharp minimum, giving an increase to the signal and characteristic plasma peak arises in the QTN spectrum. The peak location can be used for quick estimation of the total electron density (Equation 2.49). Visibility of the peak is determined by two factors: participation of the supra-thermal particles and the L_{ant}/L_D ratio. Both of these features are discussed above. For $n_h = 0$ the peak is visible for $L_{ant}/L_D > 2$ (Figure 2.3).

At high frequencies, the plasma permittivity scales as $\epsilon_L \to 1 - \omega_p^2/\omega^2$, independently of the VDF (see Chapter 5 for details). This causes rapid decrease in the power spectrum and the slope of the signal is determined by the shape of the antenna response function, yielding ω^{-3} for wire dipoles and ω^{-2} for double spheres [Meyer-Vernet and Perche, 1989].

However, if the dipole is short $L_{ant} < L_D$ then the antenna will sense only up to the distance comparable to the antenna length, giving nearly white spectrum not just below plasma frequency but also for $\omega \sim \omega_p$. In this case the plasma peak disappears and it will not be possible to obtain electron density and temperature from the spectrum as independent parameters. A brief illustration for the case of STEREO spacecraft that has $L_{ant} \sim L_D$ at $1AU$ is given in Section 2.5.2 (Figure 2.11) while detailed description is given in Chapter 4.

2.4.2 Voltage fluctuations induced by the motion of protons

The fluctuations at the antenna terminals induced by protons in the solar wind were at first expected to be observed around the ion plasma frequency $\omega_i = \omega_p\sqrt{m_e/m_p}$. However, since the solar wind speed is larger than the proton thermal speed $v_{sw} >> v_{thep}$, the noise signal is strongly Doppler-shifted towards higher frequencies and is significant up to $\omega/\omega_p \sim 0.4 - 0.8$, overlapping with the low frequency part of the electron QTN spectrum. This component can't be neglected in a fast drifting plasma as the solar wind and we need to calculate the proton induced noise and include it into the theory.

The presence of a directional factor of the solar wind speed causes necessity of introducing several characteristic angles. If we set up a cylindrical coordinate system of axis parallel to v_{sw} and call θ the angle between $\vec{k}$ and $\vec{v_{sw}}$, β the angle between $\vec{v_{sw}}$ and the antenna and define angle γ as

$$\cos\gamma = \cos\theta\cos\beta + |\sin\theta|\sin\beta\cos\varphi$$

with φ being the azimuthal angle of $\vec{k}$ in a plane perpendicular to $\vec{v_{sw}}$. The characteristic angles are shown on Figure 2.5. The proton contribution for a wire dipole antenna with triangular current distribution (Equation 2.14) can be calculated to be [Issautier et al., 1999]

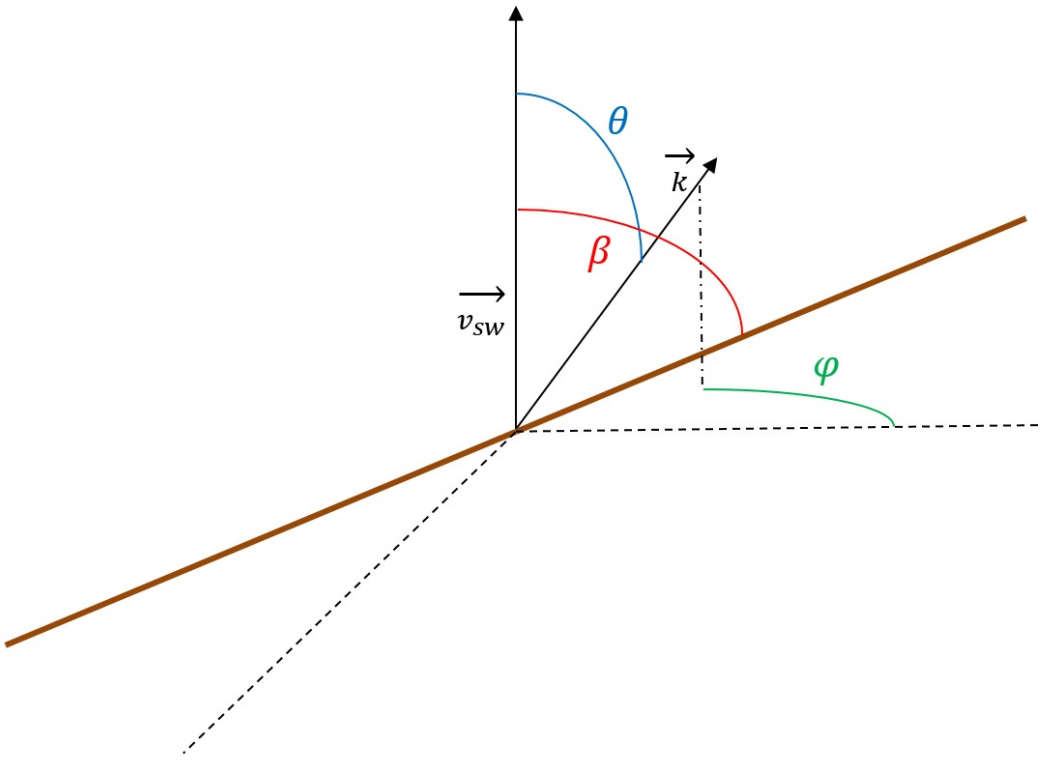

Figure 2.5: The angles used for calculation of the proton noise

$$V_{pn}^2 = \frac{8 n_p e^2 \mu}{\pi^2 \epsilon_0^2} \left(\frac{m_e}{2\pi k_b T_e^*} \right)^{1/2} \int_0^\infty \frac{dk}{k^3} \int_{-1}^{1} \frac{e^{-\mu \frac{(\omega - k v_{sw} u)^2}{k^2 v_{the}^2}}}{|\epsilon_L(k, \omega - k v_{sw} u)|^2} du \int_0^{2\pi} d\varphi \frac{\sin^4 (k L_{ant} \cos\gamma / 2)}{(k L_{ant} \cos\gamma)^2} \quad (2.57)$$

where $u = \cos\theta$ and $\mu = v_{the}/v_{thep}$ being the ratio between electron and proton thermal speed. Inside the dielectric permittivity factor the Doppler shift is introduced by replacing ω with $\omega - \vec{k} \cdot \vec{v_{sw}}$. T_e^* is generalized electron temperature given as

$$T_e^* = \frac{m_e}{k_b < v^{-2} >} \quad (2.58)$$

The generalized temperature is related to the total Debye length by the expression $L_D = \sqrt{\epsilon_0 k_b T_e^* / e^2 n_e}$. For thermal equilibrium, T_e^* is equal to T_e while for two Maxwellian VDF, it is very close to the core temperature T_c. The result given in Equation 2.57 is not appropriate for usage in data processing since it contains demandfull numerical integrations, but it can be considerably simplified for special cases of the antenna perpendicular or parallel to the solar wind flow.

If the antenna is perpendicular to the solar wind speed we have $\beta = \pi/2$ so $\cos\gamma = |\sin\theta| \cos\varphi$ and integrals over different variables u, φ and k given in Equation 2.57 can be approximated by simpler expressions. This derivation is performed by [Issautier et al., 1999] for dipole antennas and is valid whenever

$L_{ant}/L_D < v_{sw}/v_{thep} \approx 15 - 20$ which is always the case for antennas on space missions (Section 2.5), giving the result

$$V_{pn}^2(\omega) = \frac{(2m_e k_b T_e^*)^{1/2}}{4\pi\epsilon_0 M} \int_0^{+\infty} \frac{yF_\perp(yL_{ant}/L_D)}{(y^2+1+\Omega^2)(y^2+1+\Omega^2+t)} dy \tag{2.59}$$

with $F_\perp(x)$ being the antenna response function to a wave field having cylindrical symmetry around one preferred direction (in this case direction of $\vec{v_{sw}}$), derived by [Meyer-Vernet et al., 1993]

$$F_\perp(x) = \frac{8}{x}\left[2\int_0^x J_0(t)dt - \int_0^{2x} J_0(t)dt + J_1(2x) - 2J_1(x)\right] \tag{2.60}$$

In Equation 2.59 substitutions $\Omega = \omega L_D/v_{sw}$, $t = T_e^*/T_p$ and $M = v_{sw}/v_{the}$ are made. This result is a good approximation whenever $\beta > 15°$ [Tong et al., 2015], and is used further on in this work. The dependence of the noise level to the solar wind speed is given on Figure 2.6, clearly illustrating the effect of Doppler shift as the drift velocity increases. Since the purpose of the Figure is to illustrate the Doppler shift effect, the T_e/T_p ratio used is kept constant, not taking into account the well known correlation between T_p and v_{sw} in the solar wind.

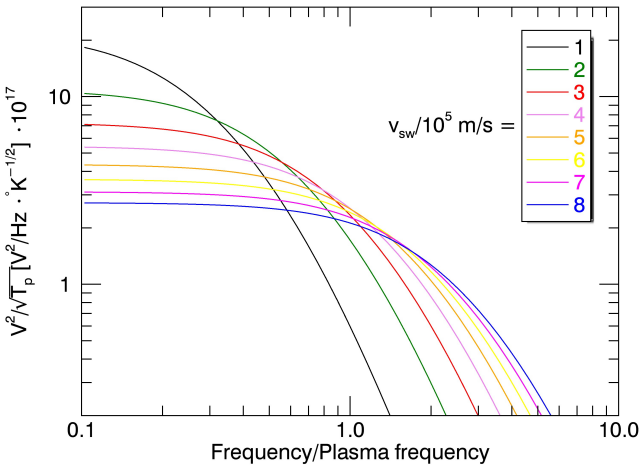

Figure 2.6: Normalized proton noise measured by a wire dipole antenna perpendicular to the solar wind speed for $L_{ant}/L_D = 1$ and $T_e^*/T_p = 2$. The Doppler shift towards higher frequencies is evident as v_{sw} increases

If the antenna is parallel to the solar wind speed, then the deduction is quite simplified as $\beta = 0$ and $\cos\gamma = u$, yielding

$$V_{pn}^2(\omega) = \frac{8k_b T_p}{\pi\epsilon_0 v_{sw}} \frac{\sin^4(\Omega L_{ant}/2L_D)}{(\Omega L_{ant}/L_D)^2} ln\left[\frac{1+t+\Omega^2}{1+\Omega^2}\right] \tag{2.61}$$

an analytical expression easy to compute. The result given in Equation 2.61 is shown on Figure 2.7, again demonstrating the strong Doppler shift as v_{sw} increases. The sinusoidal term that originates from integration over the azimuthal angle φ causes

the frequency 'harmonics' to appear in the spectrum. This approximation is suitable only for very small angles between the antenna and the solar wind speed (less than 5%) [Tong et al., 2015].

We can also note that the decrease of the signal towards high frequencies is mostly determined by the term $(\Omega L_{ant}/L_D)^{-2}$, making the proton noise for the antenna parallel to the v_{sw} less important for longer dipoles.

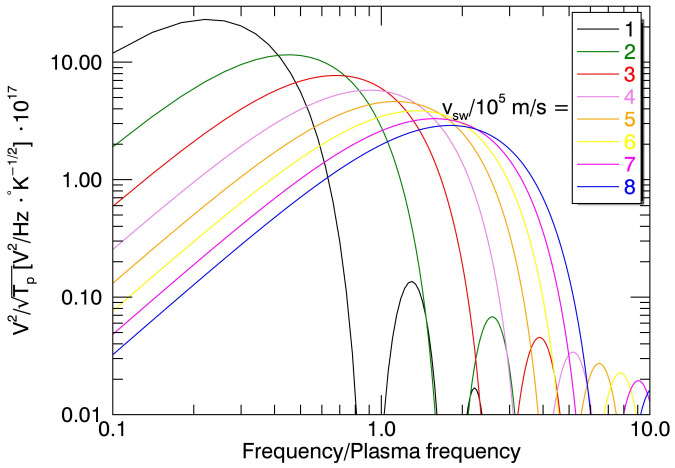

Figure 2.7: Normalized proton noise measured by a wire dipole antenna parallel to the solar wind speed for $L_{ant}/L_D = 1$ and $T_e^*/T_p = 2$. The Doppler shift is even more noticeable than for the case of the antenna perpendicular to the solar wind speed, shown on Figure 2.6

2.4.3 Shot noise

The discussion in this Section has been so far investigating only the electrostatic fluctuations of the electric field - assuming that the antenna is 'transparent' so that no particles impact its surface. In reality the antenna has a finite volume and both absorbs and emits charged particles, causing an additional 'shot noise' component to appear in the power spectrum.

The voltage on the monopole antenna due to electron impacts will decrease by an amount

$$V(\omega) = Z_{mon}(\omega)I(\omega) \tag{2.62}$$

We consider the current produced by a single impact to be an infinitely thin pulse $I_1(t) = e\delta(t - t_0)$, with a simple Fourier transform $I_1(\omega)/e = e^{i\omega t_0}$. If during a long time interval τ we have $N(\tau)$ events then

$$I(\omega) = e\sum_{j=1}^{N(\tau)} e^{i\omega t_{0j}} \tag{2.63}$$

and the power spectral density is

$$V^2_{sn(mon)}(\omega) = e^2|Z_{mon}(\omega)|^2\frac{2}{\tau}|\sum_{j=1}^{N(\tau)} e^{i\omega t_{0j}}|^2 \tag{2.64}$$

Since the 'arrival' times t_{0j} of the electrons are not dependent of each other we assume that they are regulated by the Poisson process, determined by a flux of the electrons per unit surface Φ, investigated in detail in Chapter 3. The calculation of the sum that appears in Equation 2.64 was performed by e.g. [Petit, 1975] through determination of ensemble average of the exponential factor to be

$$\lim_{\tau\to\infty} |\sum_{j=1}^{N(\tau)} e^{i\omega t_{0j}}|^2 = N(\tau)$$

which gives

$$V^2_{sn(mon)}(\omega) = 2e^2 S_{mon}\Phi|Z_{mon}(\omega)|^2 \tag{2.65}$$

where S_{mon} is the surface of the monopole and Φ is the flux per unit of the antenna surface defined as

$$\Phi = \lim_{\tau\to\infty}\frac{N(\tau)}{\tau S_{mon}} \tag{2.66}$$

For a dipole antenna, since the signals are uncorrelated, the result is twice of the result for a monopole [Meyer-Vernet, 1983]. Including $S_{ant} = 2S_{mon}$ and $Z_{ant} = 2Z_{mon}$, we obtain

$$V^2_{sn}(\omega) = \frac{1}{2}e^2\Phi S_{ant}|Z_{ant}(\omega)|^2 \tag{2.67}$$

As explained in Section 2.3.2, we can write the square modulus of the antenna impedance simply as $|Z_{ant}(\omega)|^2 = \omega^{-2}C^{-2}_{ant}$ so

$$V^2_{sn}(\omega) = \frac{e^2 S_{ant}\Phi}{2\omega^2 C^2_{ant}} \tag{2.68}$$

Beside the impact noise given by Equation 2.68 the contribution to the PSD measured is also given by the electrons that are emitted from the antenna surface. Since secondary electrons can be neglected most of the time in the solar wind at $1AU$ [Escoubet et al., 1997] and the ion flux is negligible compared to the electron flux, then the signal is determined by the electrons emitted due to photoelectric effect. Since the flux of photoelectrons is usually larger then the flux of incoming plasma electrons the antenna charges positively in order to establish an equilibrium between these two components (see Chapter 3 for details). Therefore the current equilibrium condition is $I = I_{ph}$ or, written in terms of the flux, $\Phi S_{ant} = \Phi_{ph}S_{\perp}$, with $S_{\perp}$ being the illuminated antenna surface. This finally gives

$$V^2_{sn}(\omega) = \frac{e^2 S_{ant}\Phi}{\omega^2 C^2_{ant}} \tag{2.69}$$

which is the expression for the shot noise used further on. However, the Equation 2.69 has certain limitations. First, the electron signal is given as the step function while in reality it has some finite decay time. Second, we completely neglect the noise

that particle induces on its trajectory to the antenna as well as the collective plasma effects. These approximations have been widely used by many authors (see e.g. [Kellogg, 1981, Aubier et al., 1983, Issautier et al., 1999]) as a good approximation below the plasma frequency. On the other hand, the exact theoretical treatment of the shot noise that takes into account both particle trajectories and the collective effects has been performed by [Meyer-Vernet, 1983]. However, the results obtained require very complicated and time consuming numerical integrations which makes them unpractical for processing large data sets. This is the reason why, in this work, we only investigate the shot noise spectra for $\omega < \omega_p$ (Chapter 4), preserving the validity of Equation 2.69.

Additional component of the spectrum that was not taken into account is the noise caused by the photoelectrons that leave the antenna, increasing its voltage, but do not have enough energy to escape the antenna potential well, so then 'fall' back to the surface, decreasing the voltage to the initial value. [Petit, 1975] proved that the 'returning' photoelectrons induce nearly white power spectrum that is at least an order of magnitude below the one given by Equation 2.69. Approximations used in this calculation are valid up to $\sim 300kHz$ so the QTN frequency range in the solar wind is well covered.

2.5 QTN spectroscopy in space missions

2.5.1 Pioneer work

The first attempts to send objects to the space were performed right after the Second World War. The V2 rockets, developed in the Nazi Germany as the first guided ballistic missiles, were captured in spring of 1945 and the technology was transfered to the United States, Soviet Union and Great Britain. This was the very start of the era of rockets that are further developed and used (among other purposes) for space research. Successful flights in the ionosphere were performed already in 1947 [Katzin and Katzin, 1961], followed by building more and more powerful rockets and instrumentation for in situ measurements. The pioneer experiments have measured ionosphere parameters up to $200km$ [Seddon, 1953, Seddon et al., 1954] by examining indices of refraction of the medium around the rocket. The refraction measurements had multiple difficulties and provided only integral properties along the ray paths through the ionosphere instead of a 'point' measurements. In order to measure local plasma properties more accurately, the interest for the radio antenna impedance measurements arose in 1960s leading to first rocket experiments [Jackson and Kane, 1959] and multiple theoretical models ([Katzin and Katzin, 1961, Kaiser, 1962, Balmain, 1964]).

The most acknowledged impedance model of a dipole antenna in magnetized collisional plasma that showed decent agreement with laboratory measurements was given by [Balmain, 1969]. This model gives hydrodynamic plasma description and is used as base for the impedance data interpretation on multiple rocket experiments during 1970s [Bishop, 1972, Hoang, 1972, Meyer and Vernet, 1975] and even up to this day [Spencer and Patra, 2015].

On the other hand, application of the kinetic theory to the antenna in a magnetized collisional plasma which is applicable to the ionosphere is a very difficult task which has not been done yet. The calculations have been performed only

for simple spherical geometry, but even in that case they remain very complicated [Buckley, 1966]. On the other hand, collisionless models of the antenna impedance and noise with neglected magnetic field [Kuehl, 1966, Fejer and Kan, 1969, Schiff, 1970], presented in details in Section 2.4, are not applicable to the ionosphere or magnetosphere, but only to the solar wind plasma and have been waiting for the spacecraft capable to collect data from the interplanetary medium. This was finally possible in late 1970s, opening the path to investigation of the Solar system.

2.5.2 Extraterrestrial missions

Here we will give a short overview of the past and ongoing missions in terms of the contribution to the QTN spectroscopy. The radio wave receivers on most of these missions were not specifically made to detect the quasi-thermal noise. This is why the antenna and/or instrument characteristics in some cases do not meet the demands for the 'clean' usage of the noise spectrum (given in Section 2.4) in measuring the plasma parameters. However, even on the missions where QTN was not planed to be a primary diagnostic tool, it has shown up as a convenient bi-product, providing some useful results.

International Sun-Earth Explorer(s) - ISEE

The International Cometary Explorer (ICE) spacecraft, originally named International Sun-Earth Explorer-3 (ISEE-3) [Ogilvie et al., 1978], was launched August 12, 1978, into a heliocentric orbit. It was one of three spacecraft, along with the mother/daughter pair of ISEE-1 and ISEE-2, built by a joined effort of NASA and ESA to study the interaction between the Earth's magnetic field and the solar wind [Ogilvie et al., 1977]. While ISEE-1 and ISEE-2 were used to study magnetic fields near the Earth, ISEE-3 was the first spacecraft to be placed at the L1 Earth-Sun Lagrangian point.

The ISEE-3 3-dimensional Radio Mapping Experiment (SBH) [Knoll et al., 1978] was supplied with a very long dipole made of two $45m$ antennas with $0.4mm$ in diameter. These long and thin antennas were very convenient for detection of the plasma peak. On the other hand, the SBH receiver had only 24 frequency channels in the range $30 - 200kHz$, which is not a resolution sufficient to perform detailed analysis of the spectra around the peak.

Second problem with this receiver is that the plasma frequency $f_p = \omega_p/2\pi$ is usually below $30kHz$ in the solar wind. This is why the noise that was first recognized and analyzed was actually the f^{-3} slope above the plasma frequency [Meyer-Vernet, 1979]. The first comparison of the theory with the observation of the QTN both around and above the plasma frequency was performed by [Hoang et al., 1980] for special events with sufficiently high electron density. Since assumed VDF was Maxwellian and the spectrum was calculated using the Nyquist theorem given by Equation 2.44, the theory for $\omega \approx \omega_p$ was not fitting well to the observations. Later on, [Couturier et al., 1981] accommodated the theory for two Maxwellian distribution as observed by ISEE-3. This work provided good insight into the influence of the supra-thermal electrons to the QTN spectrum and showed decent agreement with observations (Figure 2.8), even though precise measurements of the non-thermal characteristics weren't possible due to the poor instrument resolution.

On ISEE-3, the proton noise was first observed as 'f^{-1} component below the plasma frequency' [Hoang et al., 1982], which could not be explained by the QTN theory. This raised motivation to develop the theory of the noise induced by protons [Meyer-Vernet et al., 1986], presented in Section 2.4.2.

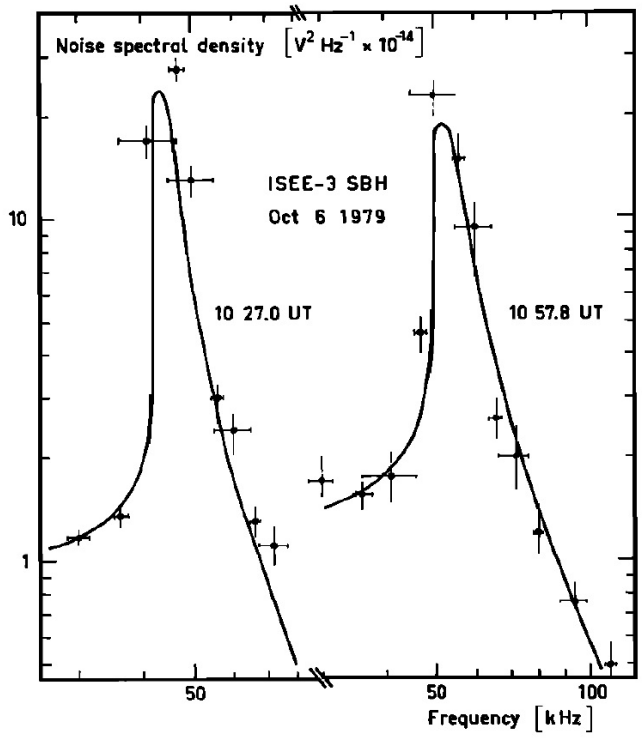

Figure 2.8: Quasi-thermal noise spectra at the receiver input as theoretically computed (solid line) and measured by ISEE-3/SBH (dots). Figure reproduced from [Couturier et al., 1981]. *Note: content of this Figure, as well as of other ones in this Section and Figure 4.1, are reproduced as they appear in original publications, so their formatting could be different than for the ones used in the rest of the thesis*

Although on the ISEE-3 systematic analysis of the QTN measurements has never been performed, the great importance of this mission was in motivating the theoretical work in order to explain the SBH spectra. NASA suspended routine contact with ISEE-3 in 1997, and made brief status checks in 1999 and 2008.

Ulysses - solar wind at high latitudes

Launched on October 6, 1990, Ulysses was intended to explore the solar wind at high heliographic latitudes (up to $\sim 80°$) at distances $1.5 - 4.2AU$. The Unified Radio and Plasma Wave (URAP) [Stone et al., 1992] receiver enabled observations of the QTN with the low frequency Radio Astronomy Receiver (RAR) subinstrument. The receiver was providing 64 equally spaced frequency channels in the range $1.25 - 48.5kHz$, which was quite decent frequency resolution that measured a 'good looking' spectra when connected to a dipole made of two $35m$ antennas ($2.2mm$ in diameter).

The Ulysses QTN measurements were suitable for deeper analysis and comparison with results from other instruments. First insights into the problematic and

results from nearly simultaneous measurements of plasma parameters from the radio receiver and particle analyzers were given by [Maksimović et al., 1992] while in-depth study was performed by [Issautier et al., 1999] with two Maxwellian model, giving very good agreement between theory and observations (Figure 2.9) and also with the SWOOPS analyzer [Bame et al., 1992] about the core temperature and total density values. The main issue with URAP measurements was the low measurement rate as one spectrum was provided only every $128s$. With such a long integration time the plasma peak expands due to density fluctuations and, since the peak size and shape are determined mostly by non-thermal electrons, disables precise measurements of the halo density and temperature. In order to overcome this difficulty, another statistical study with a single κ VDF model was done by [Le Chat et al., 2011], deriving a single, total electron temperature along with the κ index that denotes the participation of the supra-thermals in the VDF (Chapter 3). Apart from the temperature and solar wind speed profiles that were in agreement with some previous models and measurements [Ogilvie and Scudder, 1978, Scime et al., 1994, Maksimović et al., 2000], the obtained values of the κ index also confirmed increased presence of the supra-thermals in the fast wind at high latitudes. This result has demonstrated the possibility to measure the VDF properties using the QTN spectroscopy on Ulysses, even with two-minute sampling period.

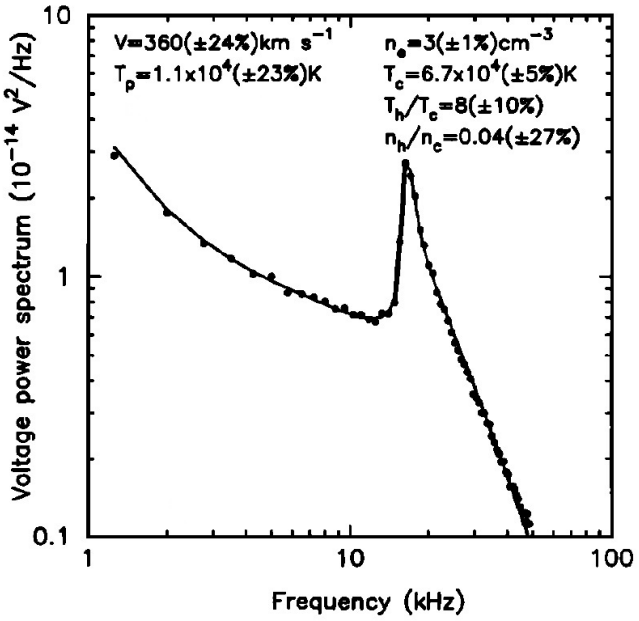

Figure 2.9: Thermal noise spectra as theoretically computed (solid line) and measured by Ulysses/URAP (dots). Figure reproduced from [Issautier et al., 1999]

After the July 1, 2008, which was scheduled as the end of the extended mission, the operations continued in a reduced capacity until the June 30, 2009, when the communication with the spacecraft was cut off entirely.

Wind

With multiple scientific objectives related to both magnetosphere and the solar wind, the mission was divided in two phases. From the launch on November 1,

1994, Wind has spent almost ten years orbiting around the Earth, making numerous crossings through the Earth's bow shock. The goal of this part of the mission was to determine the magnetospheric output to interplanetary space in the up-stream region. Afterwards, in May 2004, the spacecraft was stationed into the Lagrangian L1 point with fuel for around 60 years in order to investigate basic plasma processes occurring in the near-Earth solar wind, and has been collecting the data for over a decade now.

Wind was the first mission equipped with a device made specially for the QTN measurements. The Thermal Noise Receiver (TNR) as part of the Waves instrument [Bougeret et al., 1995] collects a QTN spectrum every $4.4s$ on 96 logarithmically spaced frequency channels in the range $4 - 256kHz$. This makes the frequency resolution to be $\delta f/f \approx 4.4\%$ which is an order of magnitude of the density measurements accuracy. Very long and thin dipole (one antenna arm $50m$ long, $0.38mm$ in diameter) gives quite clear QTN spectrum while shot noise is negligible.

The studies with the two Maxwellian models were done a decade ago [Salem et al., 2003], providing histograms that illustrate the variation of the electron density and core temperature throughout the solar cycle, while the comprehensive analysis of the Wind data using κ model is currently being performed at the Paris Observatory. The TNR measurements are very precise and can be used for comparison with data from other instruments. Since the integration time is short, the results are more accurate than the ones from similar procedures on Ulysses. Shortly after the launch, the plasma density data from the TNR and Wind/SWE Faraday Cup [Ogilvie et al., 1995] was compared on a representative data set, showing a very good agreement between measured values [Maksimovic et al., 1998]. The cross calibration of the TNR and Wind/3DP particle analyzer [Lin et al., 1995] is currently in progress at the University of California, Berkeley and insight into this work is given on Figure 2.10.

Solar TErrestrial RElations Observatory - STEREO

STEREO, launched on October 26, 2006, consists of two space-based spacecraft - one ahead of Earth in its orbit (STEREO A), and another trailing behind (STEREO B). The mission intends to understand the causes and mechanisms that initiate coronal mass ejections and accelerate the energetic particles in the low corona, though it is not primarily made to investigate the QTN. The antennas that are attached to the STEREO/Waves radio receiver [Bale et al., 2008] are $6m$ long - shorter then the Debye length of the surrounding plasma, and $2.86cm$ in diameter - making the shot noise dominant. These antenna characteristics make the plasma peak invisible in the quiet solar wind and it can only be observed during the events with low temperature and high density, usually CMEs (Figure 2.11). Beside the antenna issues, the STEREO/Waves Low Frequency Receiver (LFR) has 48 frequency channels in the $2.61 - 153.2kHz$ range, yielding $\delta f/f \approx 8.2\%$, so even in rare occasions when the plasma peak is visible, the density can be determined with just mediocre accuracy.

The QTN on STEREO is examined in detail in this work, with accommodation of the method, application and results explained in Chapter 4.

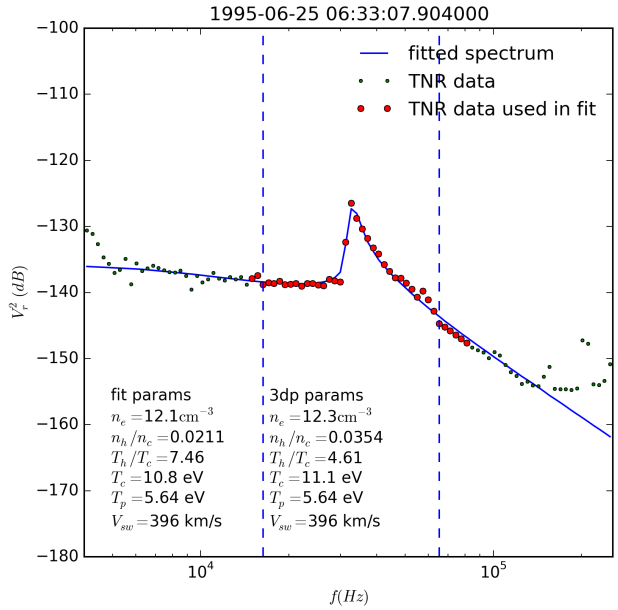

Figure 2.10: Cross calibration of the Wind/3DP parameters with the QTN spectra. Figure reproduced from [Tong et al., 2016] via personal communication

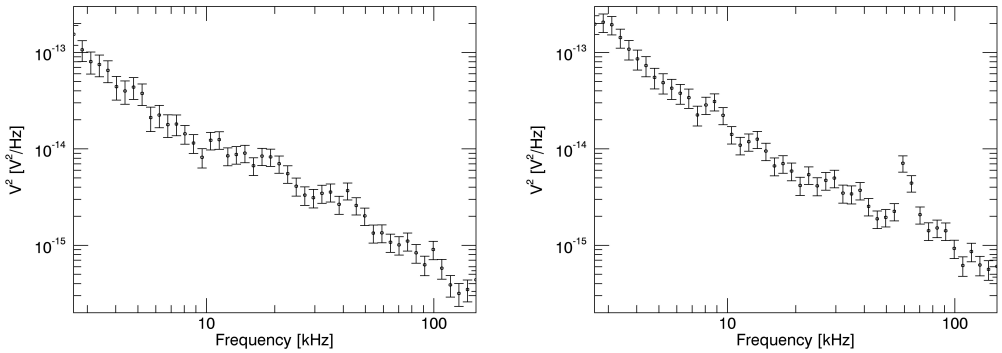

Figure 2.11: The QTN spectra obtained by STEREO A in the quiet solar wind for $L_{ant}/L_D \approx 0.6$ (left) and during the CME event for $L_{ant}/L_D \approx 2$ (right). The plasma peak is visible around $f_p \approx 58kHz$ on the spectrum presented on the right panel

Chapter 3

Orbit limited theory in the solar wind

It was demonstrated in Section 2.4.3 that the shot noise contribution is linearly dependent of the antenna surface S_{ant} as well as of the flux Φ of solar wind electrons impacting the antenna. If antenna has a large surface area, then the shot noise will be dominant compared to the electron and proton noise. An example of spectrum overwhelmed by the shot noise is shown on Figure 2.11. As will be shown below, the incoming flux Φ and, consequently, the shot noise roughly scales with $n_e\sqrt{T_e}$. This simple relation implies that any kind of systematic errors in calculating the flux will disable precise measurements of the electron temperature and shows importance of its estimation to be as correct as possible.

Accurate determination of this factor for plane, cylindrical and spherical geometries in the solar wind plasma, described by κ VDF, is the topic of this chapter. These calculations are performed in the work [Martinović, 2016] and presented in Section 3.3. Previously, we give some basic remarks on nature of the body charging in a plasma (Section 3.1) and give strict definition of the κ distribution and its parameters (Section 3.2). Generalization to non-ideal geometrical shapes is briefly discussed in Section 3.4 and some applications in the solar wind are described in Section 3.5. Application to the shot noise on STEREO antennas is given in Chapter 4.

3.1 Phenomena of charge collection in a plasma

When an object is immersed into the plasma it causes electrostatic disturbances in the surrounding area. The reason for these disturbances that do not exist in neutral gases lies in the collection of charged particles from the plasma by the object (afterwards also called collector) surface. Since the light plasma electrons are faster than the ions, they will more frequently collide with the surface of the collector. This way the surface gets charged and a 'plasma sheath' is formed around the object [Langmuir, 1923]. The sheath size is of the order of the plasma Debye length and it contains a net amount of charge in order to balance the potential of the collector surface [Laframboise, 1966, Franklin, 2003, Allen, 2008]. If there are no additional processes responsible for electron emission (photoelectric effect, secondary emission, sputtering...) then the potential is expected to be negative. On the other hand, photoelectrons ejected from the illuminated surface are approximately for an

order of magnitude more numerous than the electrons collected from the plasma in the solar wind [Pedersen, 1995], so the potential becomes positive in order to prevent loss of too many electrons.

In the pioneer work on this topic [Mott-Smith and Langmuir, 1926] established the theory of orbit limited motion of particles, calculating the incoming particle flux on the collector surface for multiple geometries and plasma VDFs. This work has been extended by many authors. For laboratory plasmas the theory has a lot of limitations, mostly due to very short Debye lengths [Allen, 1992, Annaratone et al., 1992]. On the other hand, in electrostatic probe design [Laframboise and Parker, 1973] and space plasmas it has found a great number of applications, especially in determining spacecraft floating potentials (see e.g. [Scudder et al., 2000, Kellogg et al., 2009, Henri et al., 2011]).

None of the VDFs which have been considered by previous authors allowed to take accurately into account the effect of supra-thermal particles on the surface charging process, even though it was already proven to be important for charging of dust particles on the solar wind [Meyer-Vernet, 1982, Rosenberg and Mendis, 1992, Mishra et al., 2013]. Namely, non-Maxwellian distributions exhibiting large non-thermal tails are ubiquitous in several non-collisional plasma environments, and in particular in the solar wind. The measured non-thermal VDFs are well described by the κ distribution model [Maksimović et al., 2005, Štverak et al., 2009]. Presence of these fast particles modifies both the value of the surface potential and amount of particles collected by the charged surface of a certain potential. The orbit limited theory quantitatively describes both of these effects, and is given here for the case of κ distributions. It will be shown below that the supra-thermals considerably increase the charge collection. The work presented in this Chapter can be observed as a generalization of method given by [Laframboise and Parker, 1973] to non-thermal plasma.

3.2 Definition and characteristics of κ distributions

The κ VDF is actually a generalized Lorentzian [Scudder, 1992a], power law distribution with higher percentage of supra-thermal particles compared to a classic Maxwellian, and is defined as

$$f(v) = \frac{\Gamma\big(\kappa+1\big)}{(\pi\kappa)^{3/2} v_{the\kappa}^3 \Gamma\big(\kappa-1/2\big)} \left(1 + \frac{v^2}{\kappa v_{the\kappa}^2}\right)^{-(\kappa+1)} \tag{3.1}$$

where $\Gamma(x)$ denotes the gamma function. The physical quantities are derived from the VDF moments calculated as

$$< v^n >= 4\pi \int_0^\infty v^{n+2} f(v) dv \tag{3.2}$$

Further on, it is convenient to define the average velocity as the first moment of the distribution

$$< v >_\kappa = 2\sqrt{\frac{\kappa}{\pi}} \frac{\Gamma\big(\kappa-1\big)}{\Gamma\big(\kappa-1/2\big)} v_{the\kappa} \tag{3.3}$$

Here, $< v >$ is expressed over the thermal speed $v_{the\kappa}$, which is calculated from the second moment (traditionally defining the kinetic temperature $T = m < v^2 > /3k_b$, with m being the particle mass) to be

$$v_{the\kappa} = \left(\frac{2\kappa - 3}{\kappa} \frac{k_b T}{m} \right)^{0.5} \tag{3.4}$$

The average speed $< v >_\kappa$ converges to the Maxwellian value of $< v >= \sqrt{8k_bT/\pi m}$ for very large values of the κ index, while $v_{the\kappa}$ converges to $v_{the} = \sqrt{2k_bT/m}$.

The VDF is defined for $\kappa > 1.5$ and for $\kappa \to \infty$ it reduces to the Maxwellian distribution. This property is important for the solar wind since value of the κ index can be understood as a measure of 'nonthermality' of the plasma (low values of κ assume significant portion of supra-thermal particles while for $\kappa \geq 10$ the VDF is so close to Maxwellian that it can be considered thermal). The shape of the κ distributions is given on Figure 3.1.

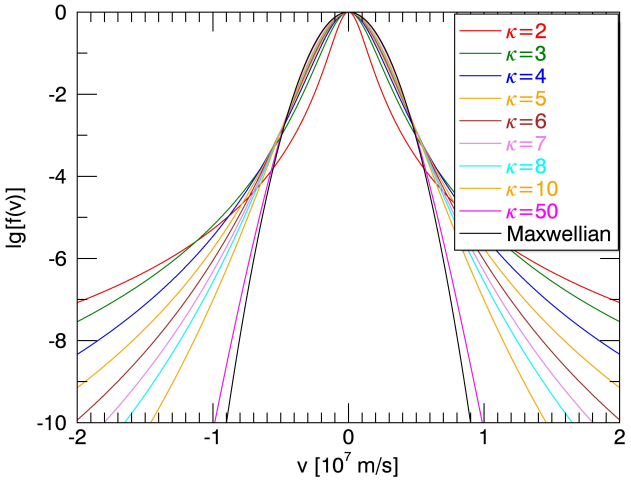

Figure 3.1: Generalized Lorentzian VDFs for different values of the κ index, normalized to $f(0) = 1$ and $T = 10eV$

3.3 Flux corrections

Now we deal with the corrections to the flux of incoming particles per unit of surface area of the charged collector. If the collector which is immersed into the plasma is not charged (has zero potential) then the flux of incoming particles will be

$$\Phi_0 = \frac{n < v >}{4} \tag{3.5}$$

which is a well known result of classical thermodynamics, for any kind of an isotropic VDF. On the other hand, this result will be modified for a finite value of the potential. As it will be seen below, this change depends on both collector geometry and VDF of particles.

3.3.1 Basics of the model

Since the solar wind plasma we observe here has extremely long mean free paths ($\sim 1AU$) it means that collisions can be neglected. We will assume that radius of the collector r_c is much smaller than particles' mean free path and that every particle has its own trajectory that comes from 'infinity' towards the collector. Also, for cylindrical and spherical collectors, the plasma local Debye length (and size of the plasma sheath) is required to be very large compared to radius of the collector. Since $L_D \approx 5 - 10m$ at distances $0.3 - 1AU$ from the Sun, both of these conditions are satisfied in the solar wind.

We observe a particle which is moving with velocity $\vec{v}$ in the electrostatic potential $\phi(\vec{r})$. A particle coming from infinity $\phi(\infty) = 0$ carries the kinetic energy $E_k = mv_\infty^2/2$. As in a collisionless plasma the particle at any distance r can be traced back to its position at $r \to \infty$ (the constants of motion are preserved, see e.g. [Watson, 1956, Bernstein and Rabinowitz, 1959]), then at the distance r its energy is given as

$$E_k(r) = \frac{mv^2}{2} + q\phi(r) > 0 \tag{3.6}$$

So, the condition for a particle to reach the collector surface is simply

$$v \geq \left(- \frac{2q\phi(r)}{m} \right)^{1/2} \tag{3.7}$$

It has been proven by [Laframboise and Parker, 1973] that this statement stays valid as long as the VDF at infinity is isotropic. This important conclusion enables the results already known for equilibrium plasma to be expanded to any isotropic distribution, in this case the generalized Lorentzian.

Consequence of Equation 3.6 is that we can find density of the particles $n(r)$ by integrating $f(v)$ over the entire velocity space except the region defined by Equation 3.7.

$$n(r) = \frac{1}{2} \int_{v > (-2q\phi(r)/m)^{1/2}} f(\vec{v}) d\vec{v} \tag{3.8}$$

The factor 1/2 arises since only the part of the VDF that moves towards the collector contributes. By analogy, the flux through a collector surface element defined by the unity vector $\vec{e_S}$ perpendicular to it is given as

$$\Phi(r) = \int_{v > (-2q\phi(r)/m)^{1/2}} \vec{v} \cdot \vec{e_S} f(\vec{v}) d\vec{v} \tag{3.9}$$

In this study we are interested only in calculating the impact rate of the particles on the collector surface so the only the flux calculations will be presented.

Using this method, the exact correction of particle flux Φ/Φ_0 for Maxwellian distribution was calculated by [Laframboise and Parker, 1973] for three different cases - plane, cylindrical and spherical geometry and for both attracting and repelling potential. The results obtained for attracting potential ($q\phi < 0$) give linear dependence of the correction from the factor $\eta = -q\phi/k_bT$ for spherical collectors, while for cylindrical ones the solution turns out to be more complicated but tends to $\Phi/\Phi_0 \sim \eta^{1/2}$ for high values of the surface potential. If we have $q\phi < 0$, then the

surface is repelling particles, decreasing the flux by the Boltzmann factor e^{η}. Here, we review these results and extend them for the case of κ distributions.

3.3.2 Attracting potential

Plane geometry

A flat infinite collector produces one-dimensional potential well. We will assume that the object surface is infinite in yz frame and potential ϕ is dispersed over x axis. For Maxwellian distribution we have

$$\Phi = n\pi^{-3/2}v_{the}^{-3}e^{\eta} \int_{\sqrt{\frac{-2q\phi}{m}}}^{\infty} dv_x \int_{-\infty}^{\infty} dv_y \int_{-\infty}^{\infty} dv_z v_x e^{-v_x^2/v_{the}^2} e^{-v_y^2/v_{the}^2} e^{-v_z^2/v_{the}^2} = \Phi_0 \quad (3.10)$$

Analogously, the expression for κ distributions is

$$\Phi_\kappa = n\frac{\Gamma(\kappa+1)}{\Gamma(\kappa-1/2)\pi^{3/2}\kappa^{3/2}v_{the\kappa}^3} \int_{\sqrt{\frac{-2q\phi}{m}}}^{\infty} dv_x \int_{-\infty}^{\infty} dv_y \int_{-\infty}^{\infty} dv_z \frac{v_x}{\left(1+\frac{v_x^2+v_y^2+v_z^2+\frac{2q\phi}{m}}{\kappa v_{the\kappa}^2}\right)^{\kappa+1}} \quad (3.11)$$

From here we make substitutions $x = v_x\kappa^{-1/2}v_{the\kappa}^{-1}$, $y = v_y\kappa^{-1/2}v_{the\kappa}^{-1}$ and $z = v_z\kappa^{-1/2}v_{the\kappa}^{-1}$. Putting these into Equation 3.11 we obtain

$$\Phi_\kappa = n\frac{\Gamma(\kappa+1)}{\Gamma(\kappa-1/2)}\frac{\kappa^{1/2}v_{the\kappa}}{\pi^{3/2}} \int_{\sqrt{\eta_\kappa}}^{\infty} dx \int_{-\infty}^{\infty} dy \int_{-\infty}^{\infty} dz \frac{x}{\left(1+x^2+y^2+z^2-\eta_\kappa\right)^{\kappa+1}} \quad (3.12)$$

where

$$\eta_\kappa = -\frac{2}{2\kappa-3}\frac{q\phi}{k_bT} \quad (3.13)$$

Result of the integral in Equation 3.12 is $\pi/(2\kappa(\kappa-1))$ and is not dependent on ϕ. Replacing Equation 3.3 into this solution we obtain

$$\Phi_\kappa = \Phi_{0\kappa} = \frac{n < v >_\kappa}{4} \quad (3.14)$$

concluding that the particle flux does not depend on the surface potential in the plane geometry for κ distributions as well as for the Maxwellian one.

Cylindrical geometry

In this geometry it is convenient to use cylindrical coordinate system with z axis parallel to the central axis of the collector and θ as the angle between the particle velocity projection to the xy plane and x axis. We choose the surface element to be perpendicular to x direction so $\vec{e_S} = \vec{e_x}$ and $\vec{v} \cdot \vec{e_S} = v_r \cos\theta$. The integration over θ is only for positive values of v_x which brings us to the Equation 6 in [Laframboise and Parker, 1973] for flux per unit of surface

$$\Phi = n\pi^{-3/2} v_{the}^{-3} e^{\eta} \int_{\sqrt{\frac{-2q\phi}{m}}}^{\infty} dv_r \int_{-\pi/2}^{\pi/2} d\theta \int_{-\infty}^{\infty} dv_z e^{-v_r^2/v_{the}^2} e^{-v_z^2/v_{the}^2} v_r^2 \cos\theta \tag{3.15}$$

for Maxwellian distribution, which gives the well-known result

$$\Phi = \Phi_0 [2\pi^{-1/2} \eta^{1/2} + e^{\eta} \operatorname{erfc}(\eta^{1/2})] \tag{3.16}$$

where $\operatorname{erfc}(x)$ is the complementary error function. Now we use the same approach for κ distribution, rewriting Equation 3.15

$$\Phi_\kappa = n \frac{\Gamma(\kappa+1)}{\Gamma(\kappa-1/2)\pi^{3/2}\kappa^{3/2} v_{the\kappa}^3} \int_{\sqrt{\frac{-2q\phi}{m}}}^{\infty} dv_r \int_{-\pi/2}^{\pi/2} d\theta \int_{-\infty}^{\infty} dv_z \frac{v_r^2 \cos\theta}{\left(1 + \frac{v_r^2 + \frac{2q\phi}{m} + v_z^2}{\kappa v_{the\kappa}^2}\right)^{\kappa+1}} \tag{3.17}$$

From here we make substitutions $x = v_r \kappa^{-1/2} v_{the\kappa}^{-1}$ and $y = v_z \kappa^{-1/2} v_{the\kappa}^{-1}$ and, after performing a trivial integration over y, obtain

$$\Phi_\kappa = \Phi_{0\kappa} \frac{4\Gamma(\kappa+1/2)}{\pi^{1/2}\Gamma(\kappa-1)} \int_{\sqrt{\eta_\kappa}}^{\infty} \frac{x^2 dx}{(1 + x^2 - \eta_\kappa)^{\kappa+1/2}} \tag{3.18}$$

For zero value of the potential we have

$$\int_0^{\infty} \frac{x^2 dx}{(1+x^2)^{\kappa+1/2}} = \frac{\pi^{1/2}\Gamma(\kappa-1)}{4\Gamma(\kappa+1/2)} \tag{3.19}$$

and the result is simply $\Phi_\kappa(\phi = 0) = \Phi_{0\kappa}$. In general case (non-zero potential), Equation 3.18 can be represented in terms of regularized hypergeometric function ${}_2\bar{F}_1$ as

$$\Phi_\kappa = 2\Phi_{0\kappa}\pi^{-1/2}\Gamma(\kappa+1/2)[\Gamma(\kappa)]^{-1}\eta_\kappa^{1-\kappa} {}_2\bar{F}_1\left(\kappa-1, \kappa+1/2, \kappa, 1-\eta_\kappa^{-1}\right) \tag{3.20}$$

For different integer values of κ the general solution can be obtained by performing recursive integrations by parts. The results for $\kappa \leq 5$ are given in Table 3.1, and Figure 3.2 illustrates larger number of solutions (since, for example, the expression for $\kappa = 50$ is the 49-order polynomial it is inconvenient to tabulate all the results).

The Equation 3.20 quantifies the increase in the incoming particle flux received by a cylindrical collector at a given potential in non-thermal plasma. It is clearly visible that the correction is not negligible if the Maxwellian is replaced by κ VDF.

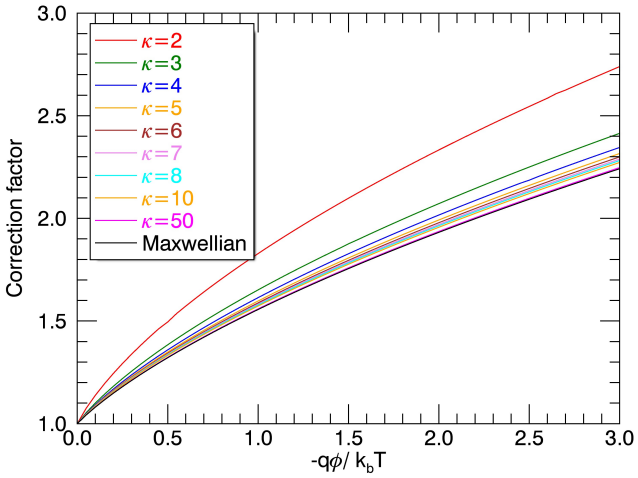

Figure 3.2: Particle flux correction factor in cylindrical geometry due to attracting potential for different values of κ index. Black line is the result given by [Mott-Smith and Langmuir, 1926] and [Laframboise and Parker, 1973] for Maxwellian electrons

Since for wire dipole antennas in the solar wind we have $a_{ant} << L_D$ then we can observe them as infinite cylinders and this result can be used for precise estimation of the shot noise level given by Equation 2.69.

κ	$\Phi_\kappa/\Phi_{0\kappa}$
2	$\frac{1-(2\eta)^{3/2}}{1-2\eta}$
3	$\frac{9+6^{1/2}\eta^{3/2}(2\eta-5)}{(3-2\eta)^2}$
4	$\frac{-500+10^{1/2}\eta^{3/2}(175+12\eta(\eta-7))}{4(2\eta-5)^3}$
5	$\frac{19208+14^{1/2}\eta^{3/2}(-5145+2\eta(1323+10\eta(2\eta-27)))}{8(7-2\eta)^4}$

Table 3.1: Expressions for correction of the particle flux due to attracting potential of a cylindrical collector for multiple values of κ index.

Spherical geometry

In this case we use spherical coordinates with polar axis along z direction, and angle θ that satisfies $v_z = v\cos\theta$. If we choose the surface element to be perpendicular to the z axis, we obtain for Maxwellian distribution

$$\Phi = n\pi^{-3/2}v_{the}^{-3}e^{\eta}\int_{\sqrt{\frac{-2q\phi}{m}}}^{\infty} dv \int_0^{\pi/2} d\theta \int_0^{2\pi} d\psi e^{-v^2/v_{the}^2} v\cos\theta v^2\sin\theta \tag{3.21}$$

resulting with $\Phi = \Phi_0(1+\eta)$. On the other hand, the same method for κ distribution gives

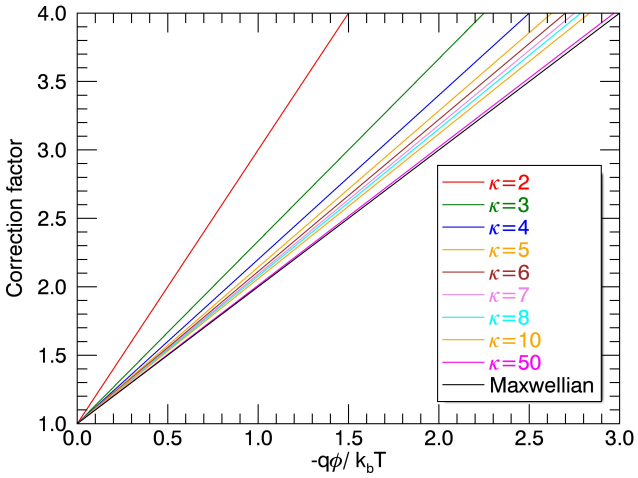

Figure 3.3: Particle flux correction factor in spherical geometry due to attracting potential for different values of κ index. Black line is the result given by [Mott-Smith and Langmuir, 1926] and [Laframboise and Parker, 1973] for Maxwellian electrons

$$\Phi_\kappa = n\frac{\Gamma(\kappa+1)}{\Gamma(\kappa-1/2)\pi^{3/2}\kappa^{3/2}v_{the\kappa}^3}\int_{\sqrt{\frac{-2q\phi}{m}}}^{\infty} dv \int_0^{\pi/2} d\theta \int_0^{2\pi} d\psi \frac{v^3\sin\theta\cos\theta}{\left(1+\frac{v^2+\frac{2q\phi}{m}}{\kappa v_{the\kappa}^2}\right)^{\kappa+1}} \quad (3.22)$$

Substituting $x = v\kappa^{-1/2}v_{the\kappa}^{-1}$ we obtain

$$\Phi_\kappa = \Phi_{0\kappa}2\kappa(\kappa-1)\int_{\sqrt{\eta_\kappa}}^{\infty}\frac{x^3dx}{(1+x^2-\eta_\kappa)^{\kappa+1}} \quad (3.23)$$

which is solved to give

$$\Phi_\kappa = \Phi_{0\kappa}\left(1+\frac{2\kappa-2}{2\kappa-3}\eta\right) \quad (3.24)$$

These linear solutions are given on Figure 3.3, clearly showing that spherical collectors are more sensitive to the variation of the VDF than cylindrical ones. However, this result is, in most cases, usable only as a first approximation since there are almost no real objects in the solar wind that have precisely spherical shape, as spacecraft body is usually not spherical and the double sphere antennas need to be placed on a boom that affects the particle collection. Limitations of the theory are discussed in more detail in Section 3.4.

3.3.3 Repelling potential

All the calculations above assume positive η and η_κ, which means that the potential is attractive. If it is not the case then we deal with the repelling potential which will effectively reduce the incoming particle flux. In order to calculate this flux, we make use of the same condition given in Equation 3.7, taking care that modulus

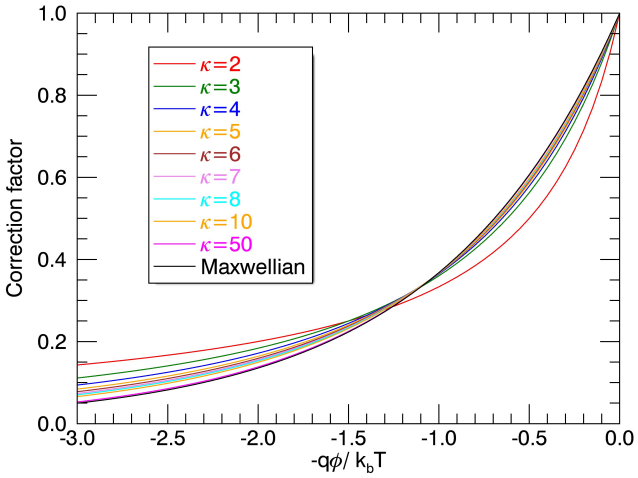

Figure 3.4: Particle flux correction factor due to repelling potential for different values of κ index. Black line is the result given by [Mott-Smith and Langmuir, 1926] and [Laframboise and Parker, 1973] for Maxwellian electrons

of the velocity vector v can't be negative. This effectively means that, when η_κ is negative, the integration in Equations 3.12, 3.18 and 3.23 can't go below zero. All three of these Equations give the same result

$$\Phi_\kappa = \Phi_{0\kappa}(1 - \eta_\kappa)^{1-\kappa} \tag{3.25}$$

and we conclude that the repelling potential provides the same correction to the incoming flux regardless of the collector geometry. Also, for very large values of κ, Equation 3.25 converges to the well-known Maxwellian limit $\Phi = \Phi_0 e^\eta$. The result is given on Figure 3.4, clearly showing that high values of the repelling potential can decrease the particle collection for more than an order of magnitude.

3.4 Validity of the theory for non-ideal collector shapes

If the collector is not an ideal cylinder or sphere then it is necessary to acknowledge limits of usage of the theory given above. As it was noted in Section 3.3.1, the 'orbit limited criterion' is that all particles arrive to the collector from 'infinity', so none of the particles can originate from the collector surface, for the results above to be valid. If we assume the opposite - that a particle does originate from the surface of the collector and then returns to it, then that particle needs to reach a point where it will have zero kinetic energy E_k (and maximum distance from the surface) before it starts to 'descend' back. Consequently, the criterion is $E_k = 0$ for spherical surfaces and $E_{k\perp} = 0$ for cylindrical ones. The important implicit condition is that the radius of the 'returning' orbit, when the theory breaks down, needs to be smaller than the equipotential surface radius at point of tangency.

Since these analyses are observing only a single particle without any collective effects, then the results given by [Laframboise and Parker, 1973] are valid for κ

distributions as well as for the Maxwellian one. This is why the full derivation of the criteria will not be repeated here, but only the results for the sake of completeness.

If we have cylindrical collector then, $\partial\phi/\partial r > 0$ for all values of r, and it will not be possible for any of the particles that satisfy conditions from Equation 3.7 to pass the surface twice, so we conclude that 'orbit limited criterion' is valid for cylinders for any kind of VDF. The same authors showed that we can apply the theory not just for circular cylinders, but for any kind of a convex cylinder. On the other hand, for spheroids there are limitations for the ratio of major to minor axis. For a prolate spheroid, maximum 'allowed' ratio is 1.653 and for oblate 'Earth-like' one, the maximum ratio is 2.537.

For more complicated collector shapes the problem is, in general, very difficult to calculate, but some general remarks can be given. If the collector is not completely convex (there are flat surfaces on it), then the theory will not be applicable. The same can be claimed for surfaces that contain 'cusps' since at these particular points we have infinitely small radius of equipotential surface. The complicated shapes of spacecraft bodies are the reason why the theory of particle collection can be used only with very rough assumptions and up to a very small confidence level. This statement has been confirmed for geometries of several spacecraft (see e.g. [Kellogg et al., 2009]). On the other hand, antennas can be considered to be close to infinite cylinders and the theory given here has turned out to be very useful (Chapter 4). The accuracy of the results for the antennas depends mostly on the confidence level of determining the photoelectron parameters (see next Section for details).

In general, the geometries that appear in both space missions and laboratory experiments are never perfectly shaped as in the theory presented in Section 3.3 and we will always have some smaller or larger deviations from the orbit limited criteria. One of the efficient ways to estimate the influence of these geometrical irregularities is usage of different simulations. However, performing a reliable simulation is a difficult task, even for the simplest realistic conditions, and demands developing of very efficient and optimized softwares (see e.g. [Roussel et al., 2005]) as well as powerfull supercomputers.

3.5 Applications in the solar wind

Velocity distribution of both protons and electrons has been measured with particle analyzers during various missions and analyzed in detail by many authors. These results show that the κ index is varying with heliographic distance and solar wind speed. The closest distance covered with spacecraft that give reliable VDF measurements is up to $\sim 0.3AU$. By analyzing the data, it has been proven (see e.g. [Štverak et al., 2009]) that, beside the Maxwellian core that carries $\sim 90\%$ of all particles, the κ index is decreasing with distance from the Sun for both halo and strahl components. Moreover, it is also evident that κ is lower for the fast solar wind.

Measured values give $\kappa \approx 10$ at $0.3AU$ decreasing with $\sim r^{0.65\pm0.15}$ for the slow wind (for both halo and the strahl), $\kappa \approx 7$ at $0.3AU$ decreasing with $\sim r^{0.45\pm0.1}$ (halo) and $\kappa \approx 14$ at $0.3AU$ decreasing with $\sim r^{0.9\pm0.1}$ (strahl) for the fast wind [Maksimović et al., 2005, Štverak et al., 2009]. Approximate values (with $\sim 20\%$ measurement errors) are given on Figure 3.5. These values, along with changes in temperature and density of the solar wind, determine the incoming particle flux $\Phi_{0\kappa}$

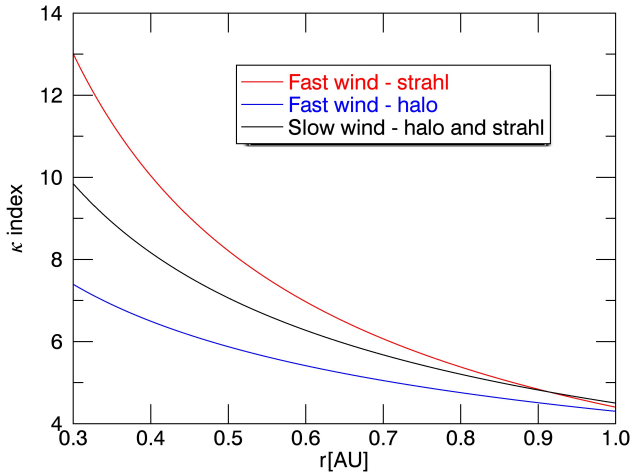

Figure 3.5: Evolution of κ index for non-thermal parts of VDFs measured by Helios between 0.3 and 1 AU. Results are given in details in the work by [Štverak et al., 2009]. Uncertainties of the results are less than 25%

as well as the corrections given in Section 3.3 as a function of distance from the Sun.

On the other hand, as already described in Section 2.4.3, the electron kinetics on the collector surface is determined by the photoelectric effect. Flux of the photoelectrons Φ_{ph} depends only on the sunlight intensity (decreasing as square of the distance from the Sun) and properties of the surface material. For a given cover material and frequency of incident radiation, the rate at which photoelectrons are ejected from the surface is directly proportional to the intensity of the incident light. Some order of magnitude estimates of both the flux of plasma electrons and the photoelectron flux at zero potential are given on Figure 3.6. On the Figure we use parameters $\Phi_{ph} = 1 - 5 \cdot 10^{14}(r[AU])^{-2}[m^{-2}s^{-1}]$, $n = (5 \pm 1)(r[AU])^{-2}[cm^{-3}]$ and $T = 10(r[AU])^{-0.8}[eV]$. The way these factors affect the shot noise spectrum as we move towards the Sun is briefly discussed below and illustrated in Section 6.1.

The equilibrium condition which determines the surface potential is that current produced by the photoelectrons escaping from the collector potential well and by electrons being collected from the surrounding plasma Φ_κ are balanced. If distribution of the emitted photoelectrons is Maxwellian, then the current balance equation at the collector surface is

$$S_\perp \Phi_{ph} e^{-\frac{e\phi}{k_b T_{ph}}} = S\Phi_\kappa \tag{3.26}$$

where $S_\perp$ and S are sunlight and total surface of the collector, charge q is replaced by $-e$ and Φ_κ is given by Equations 3.14, 3.20 and 3.24, depending on the geometry. With T_{ph} we mark the photoelectron temperature. The value of this parameter has been measured by many authors and is found to be $\sim 3eV$ (Henri et al. 2011) for spacecraft covers and $\sim 2-2.7eV$ for standard Beryllium–Copper ($BeCu$) antennas (Scudder et al. 2000, Pedersen et al. 2008, Kellogg et al. 2009). With assumption of these parameters, the potential ϕ of the collector can be found as the solution of Equation 3.26. Since values of Φ_κ are for an order of magnitude below values of Φ_{ph} in the solar wind, it is clear that potential of the antenna and spacecraft surface will

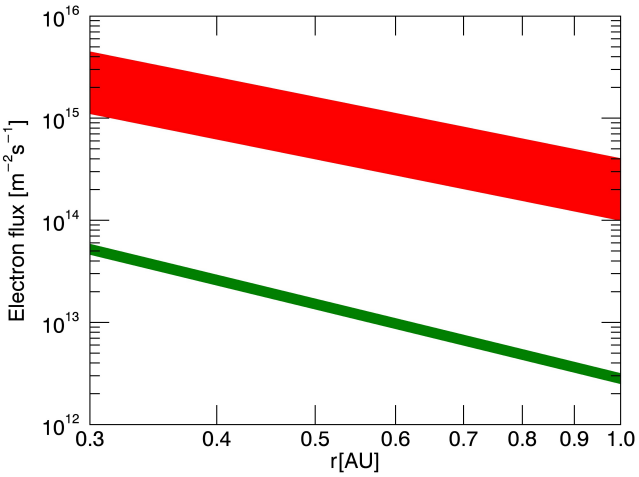

Figure 3.6: Approximate values for photoelectron flux at zero potential of standardly used $BeCu$ antennas Φ_{ph} (red) and flux of plasma electrons $\Phi_{0\kappa}$ (green). Values of the κ parameter used are given on Figure 3.5, assuming the slow solar wind. Width of each line represents range of parameters measured by various authors

be positive - attracting for electrons and characteristic values at $1AU$, calculated using the standard parameters given above, are $\phi \approx 3 - 9V$ for both spacecraft and antenna surface (see Section 4.2.1 for details). Negative potential can appear only in shadowed areas.

It is important to note that Equation 3.26 neglects secondary electrons. As fast electrons have higher probability to induce the secondary emission, this approximation can become problematic for small values of the κ index (usually in the fast solar wind and at very large distances from the Sun where even $\kappa \approx 2$ was measured [Maksimović et al., 1997b, Le Chat et al., 2011]). This problem was discussed by [Meyer-Vernet, 1982] while investigating potential of dust grains and also noticed during examination of the spacecraft floating potential in the fast solar wind using particle analyzers data from Wind mission [Salem, personal communication]. At this point, we can just conclude that results based on the current balance derived in this Section should be taken with some reserve when dealing with large fractions of supra-thermals and that influence of the secondary electron emission on charging processes needs to be detailedly investigated in the future.

Comparison of floating potential values in the κ and Maxwellian cases

The method of determination of the collector potential (antenna or spacecraft) needs to be used to perform or upgrade various in situ measurements in the solar wind. In this work we estimate the potential in order to find the flux of the plasma electrons arriving at the surface of the antenna (which we assume to be equal to the photoelectron flux leaving the antenna in equilibrium). The factor Φ from Equation 2.69 is determined self-consistently by solving Equation 3.26 for given parameters Φ_{ph} and T_{ph}. It turns out that the photoelectron parameters strongly affect the calculated value of Φ_κ, significantly decreasing the accuracy of determined plasma

VDF moments if the shot noise is dominant in the spectrum. This is the case for the study presented in Chapter 4 where the problem of postulating adequate photoelectron parameters is discussed in more detail.

Even though the correction of incoming particle flux has to be taken into account when calculating the shot noise (Section 3.3), the value of surface potential is not considerably changed. We can prove this statement by comparing the potential calculated by Equation 3.26 for cases of Maxwellian and κ distributions. If we mark these two potentials as ϕ and ϕ_κ and calculate them using flux expressions Φ and Φ_κ then we can subtract two versions of Equation 3.26 to obtain

$$ln\left[\frac{\Phi}{\Phi_\kappa}\right] = \frac{e}{k_b T_{ph}}(\phi_\kappa - \phi) \tag{3.27}$$

The fluxes given of the left hand side of Equation 3.27 are equal to the flux of electrons impacting the antenna at zero potential given by Equation 3.5 times corrections given in Section 3.3. As for the 'worst case', that is, the largest flux ratio and potential difference is for a spherical collector, we can write

$$\frac{\phi_\kappa}{\phi} = 1 + \frac{T_{ph}[eV]}{\phi[V]} ln\left[\sqrt{\frac{\kappa}{\kappa - 3/2}}\frac{1 + \frac{e\phi}{k_b T}}{1 + \frac{2\kappa-2}{2\kappa-3}\frac{e\phi_\kappa}{k_b T}}\right] \tag{3.28}$$

At $1AU$, value of the potential is $4.5 - 5.5V$ for standard solar wind parameters if $S_\perp/S = 0.5$. We can illustrate its variation with κ using Equation 3.26 to self-consistently calculate the potential with κ as the only varied parameter. The result is shown on Figure 3.7. It is noticeable that the potential ratio is around 1% for $\kappa \approx 4-5$, standardly measured at $1AU$, while it can increase up to $\sim 5\%$ for $\kappa = 2$. From here we can conclude that the difference induced by the supra-thermal electrons affects the accuracy of the QTN spectroscopy less than standard uncertainties of the instruments (see Chapter 4 for details) and much less than uncertainties of the photoelectron parameters.

Since the ratio between the photoelectron and plasma flux remains of the same order of magnitude as we move towards the Sun (Figure 3.6), the expected values of the potential will also remain of the same order of magnitude ($\sim 3-9V$), so $e\phi/k_bT$ fractions on the right hand side of Equation 3.28 should not exceed 0.5. This implies $\phi_\kappa - \phi < 1V$ even for $\kappa = 2$ and the potential difference tends to zero as κ increases, as expected. Also, as the logarithmic slope of the plasma flux given on Figure 3.6 is larger than the slope of the photoelectron flux (which is exactly equal to 2), the potential should slightly increase with distance.

In order to confirm these conclusions, we can calculate, again using Equation 3.26, the potential for both Maxwellian and κ distributions with solar wind and photoelectron parameters given on Figures 3.5 and 3.6 for wide range of distances from the Sun. The result is given on Figure 3.8, showing that indeed the difference between two potentials is less than $1V$ even if we assume a VDF with significant portion of supra-thermals. However, it must be noted that this result is only a decent approximation since effects of both secondary electrons and strahl, that might become important close to the Sun, are neglected.

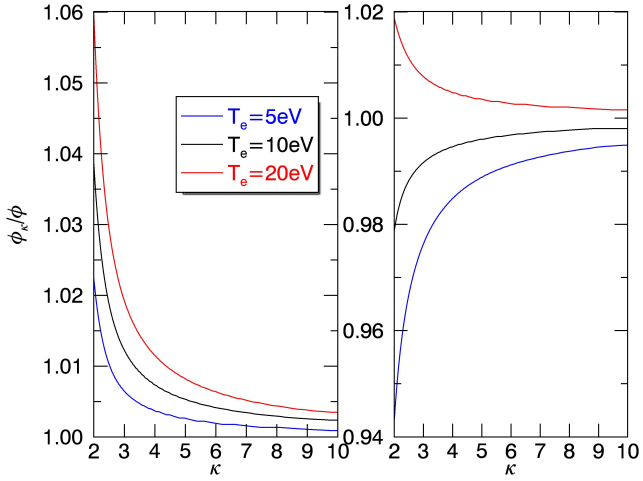

Figure 3.7: The cylindrical (left) and spherical (right) collector potential variation with κ index for different values of the electron temperature. The photoelectron parameters and electron density are assumed to be constant and equal to $\Phi_{ph} = 10^{14} m^{-2} s^{-1}$, $T_{ph} = 2eV$ and $n = 5cm^{-3}$, respectively, which are standard values at $1AU$, and $S_\perp/S = 0.5$. The potential value (not shown here) varies between $\phi = 4.7 - 5.7V$, and decreases with the temperature. Influence of the κ index is small and causes changes that are less than 5%, even for very low temperatures and low values of κ

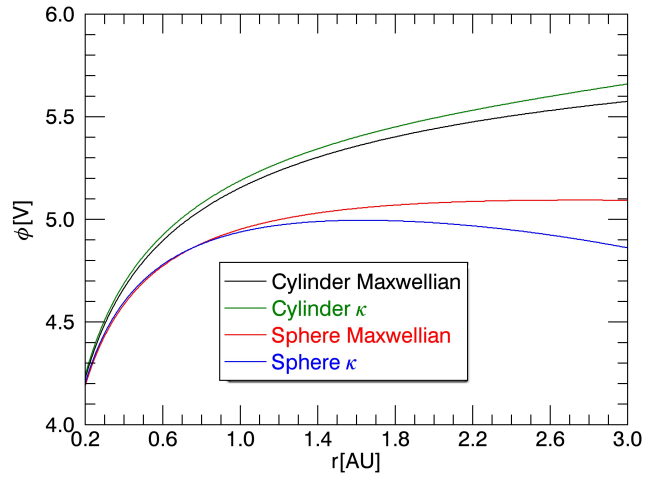

Figure 3.8: Approximate collector potential values calculated using Equation 3.26 with Maxwellian and κ models for the quiet solar wind conditions described above and shown on Figures 3.5 and 3.6. For purposes of illustration, we assume T_{ph} and $S_\perp/S$ to be the same as on Figure 3.7. Value of the κ index used has a power-law decrease from 12.8 to 2.2 throughout the plot range

Effect of the strahl

The strahl is well described by the κ distribution that is shifted by mean velocity v_{beam} and exhibits larger temperature anisotropies compared to the halo. Conse-

quently, in the reference frame moving with velocity v_{beam}, it can be described by a standard κ VDF with mean velocity $< v >_{s0}$ given by Equation 3.3. The flux corrections calculated in Section 3.3 still apply, but the value of flux at zero potential need to be calculated as

$$\Phi_0 = n_s \int \vec{v} \cdot \vec{e_S} f_s(\vec{v}) d\vec{v} \tag{3.29}$$

where $f_s(\vec{v})$ is the normalized anisotropic distribution described above. Contribution of this component is additive to the isotropic part.

Chapter 4

Electron temperature deduction on STEREO/WAVES using the QTN spectroscopy

In this Chapter, we apply QTN spectroscopy to the STEREO A and B spacecraft in order to obtain electron moments. These measurements are of importance as STEREO/SWEA (acronyms and brief descriptions of the instruments are given in Section 4.1) electron analyzers malfunction in detecting the low energy (below $45eV$) electrons since beginning of the mission and, at present time, no reliable measurements on thermal electrons exist on board these spacecraft [Fedorov et al., 2011]. In general, it is possible to obtain electron local density n_e and kinetic temperature T_e as independent parameters from the analysis of a QTN spectrum due to the existence of the plasma peak, as described in Section 2.4.1. However, since STEREO is equipped with $6m$ monopoles and orbits at $1AU$ from the Sun, where local Debye length is of the order of $10m$, the peak is expected to be observed only under special circumstances, e.g. in structures of high density and low temperature where the Debye length is small [Bougeret et al., 2008].

Beside VDF, the QTN spectrum is highly affected by size and shape of the antennas which, on STEREO/Waves, have a large surface area [Bale et al., 2008], and shot noise dominates the power spectrum at frequencies lower than ω_p. Therefore, measurement of the product $n_e\sqrt{T_e}$ can be derived from the shot noise spectra. Such kind of analysis has been previously performed by [Zouganelis et al., 2010] to derive the stray capacitance of the STEREO/Waves dipole. It is important to note that the method described here is impossible to perform when nanodust impact bursts are detected by the dipole, because the signal caused by dust is very high due to large antenna radii [Meyer-Vernet et al., 2009, Pantellini et al., 2012] and overwhelms the thermal noise.

Before describing the details of the QTN spectroscopy technique accommodated for STEREO instrumentation (Section 4.2), we will introduce some basic aspects of the mission (Section 4.1). Further on, we use STEREO/LFR measurements of the QTN, coupled with proton density measurements by PLASTIC instrument to provide electron temperature data for both STEREO A and B spacecraft (Section 4.3).

Due to lack of electron analyzers data to use for calibration, we compare the results of our analysis with the electron temperature provided by Wind using data

from the period when Wind and STEREO B were positioned close to each other (Section 4.4) in a similar way as it was done by [Zouganelis et al., 2010]. This comparison shows that our technique is reliable when integrated on a timescale of the order of 50 to 60 minutes. In addition to this real-time test, electron temperature histograms accumulated over ten months by Wind particle analyzers and the QTN spectroscopy technique on board STEREO A are finally compared, showing a good agreement between Wind and STEREO results.

Finally, since the ultimate goal of the study described above (which can be also found in [Martinović et al., 2016b]) is to provide, for the first time, a continuous survey of the electron temperature on STEREO, we will analyze possibilities and issues related to making such database in Section 4.5.

4.1 The STEREO mission

STEREO is the third mission in NASA's Solar Terrestrial Probes (STP) program that has a primary goal to understand the physical processes between the Sun and Earth. Beside STEREO, Thermosphere, Ionosphere, Mesosphere Energetics and Dynamics (TIMED) mission, exploring Earth's mesosphere and lower thermosphere, operates since 2001, Hinode (Solar-B) mission that aims to observe magnetic field structure of the Sun operates since 2006 and Magnetospheric Multiscale (MMS) mission that examines the Earth's magnetosphere operating since 2015 are also part of the program.

Primary science objective of the mission is to explore in detail the physical background of origin and propagation of CMEs. Energetic particle acceleration in the low corona and the interplanetary medium as well as the ambient solar wind are partially explored.

Two nearly identical spacecraft - one ahead of Earth in its orbit (STEREO A) and the other trailing behind (STEREO B) make both in situ and remote sensing observations simultaneously. The payload of each spacecraft contains four sets of instruments.

Sun Earth Connection Coronal and Heliospheric Investigation (SECCHI) [Howard et al., 2008] contains set of chronographs along with visible light and UV imagers in order to primarily observe propagation of CMEs. The SECCHI observations are not used in this work.

In-situ Measurements of Particles and CME Transients (IMPACT) [Luhmann et al., 2008] is a suite of seven instruments for various particle and magnetic field measurements. The IMPACT Solar Wind Electron Analyzer (SWEA) [Sauvaud et al., 2008] is particularly important for this work. Namely, the instrument was designed to make precise measurements of the electron distribution at $1AU$ but it experienced a serious malfunction, giving compromised low energy measurements (up to $45eV$). Consequently, the electron VDF moments are not possible to accurately determine from the SWEA data even though some approximative modeling is still possible [Fedorov et al., 2011]. This problem motivated the work presented in this Chapter - processing the radio instrument data to obtain the electron moments.

The Plasma and Supra-thermal Ion Composition (PLASTIC) [Galvin et al., 2008] provides measurements of kinetic properties and composition of ions and high energy particles. In this work, the data from PLASTIC was used for both obtaining proton parameters and electron density estimate, so the electron temperature could

be measured independently (see Section 4.3 for details). The data itself has been updated several times by the instrument team during the mission, each time improving the accuracy of the results, but detailed analysis of the data show that further improvements are necessary.

The radio measurements are performed by STEREO/Waves [Bougeret et al., 2008] with primary intention to study the solar Type II and Type III radio bursts. These measurements are collected by the High Frequency Receiver (HFR). The Low Frequency Receiver (LFR) gives measurements of the low frequency part ($2.6 - 153kHz$) of the spectrum, which is of interest for the QTN spectroscopy, and is described in more detail in Section 4.2.2. A Fixed Frequency Receiver (FFR) measures radio emissions at around $30MHz$, at high time resolution, for purposes of comparison with ground-based radioheliograph measurements. Time Domain Samplers (TDS) makes in situ analysis of the waveform on electric antennas, giving the data very important for the radio bursts. The instrument hardware contains three mutually orthogonal $L_{ant} = 6m$ monopole antennas; each antenna is having an average radius of $a_{ant} = 1.15cm$ [Bale et al., 2008]. The three monopoles are deployed away from the Sun so that they remain out of the fields of view of sunward looking instruments. The antennas are placed on the anti-sun side of the spacecraft in such a way that X and Y monopoles are inclined by $\beta \approx 125°$ and Z monopole by $\beta \approx 145°$ to the Sun-spacecraft direction (this is the angle defined in Section 2.4.2 and shown on Figure 2.5), which gives approximate relations for the ratio of total to illuminated antenna surface $S_{mon}/S_{\perp_x} \approx 4.41$, $S_{mon}/S_{\perp_y} \approx 3.84$ and $S_{mon}/S_{\perp_z} \approx 6.19$ [Kellogg et al., 2009]. All three antennas are mounted at the same location on the spacecraft body. The position and layout of the antennas are shown on Figure 4.1.

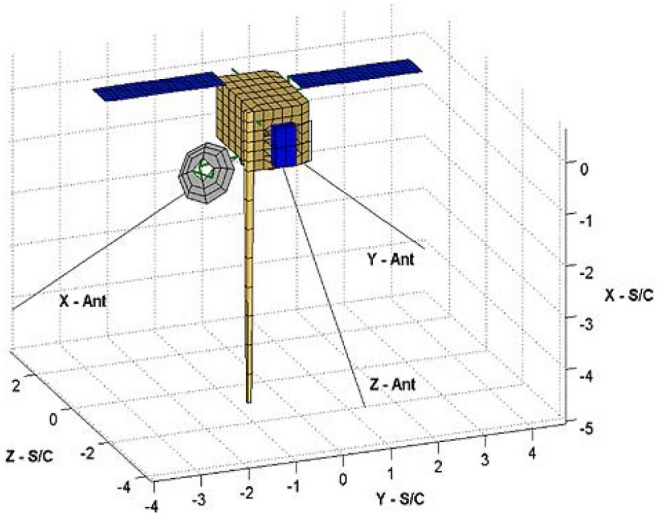

Figure 4.1: A plot of the antennas position with respect to the spacecraft payload. This Figure is reproduced from [Bale et al., 2008]

4.2 QTN spectroscopy on STEREO/Waves

The goal of this Section is to provide the generic spectrum as it is supposed to be measured by the LFR in quiet solar wind conditions. We use the theory given in Chapters 2 and 3 with parameters of the spacecraft given in Section 4.1. After calculating the theoretical spectrum we will be able to compare it with the data.

4.2.1 Accommodation of the theory to STEREO antennas

The QTN method can be applied to measurements in the frequency range above the ion plasma frequency up to the region of significant galactic radiation ($\sim$ few hundred kHz [Zaslavsky et al., 2011]). In this range, the voltage spectral density measured at the terminals of an electric antenna in the solar wind consists of three different contributing noises described in details in Section 2.4: the electron quasi-thermal noise V_{qtn}^2 due to the ambient electrons thermal motion, the proton noise V_p^2 due to the protons thermal motion which is Doppler-shifted by the solar wind bulk speed and the electron shot noise V_{sn}^2 due to electron impacts on the antenna. All three of these components are highly affected by antenna size and shape. The spectrum observed by the receiver is, following Equation 2.7

$$V_{obs}^2 = \Gamma^2 \left(V_{qtn}^2 + V_p^2 + V_{sn}^2 \right) + V_{LFR}^2 \tag{4.1}$$

Here V_{LFR}^2 is the receiver internal noise, given by [Bougeret et al., 2008] and Γ is the antenna gain (see Section 2.3.2). Stray capacitance for STEREO/Waves has been measured to be $C_{stray} \approx 32pF$ [Bale et al., 2008, Zouganelis et al., 2010]. The value of the antenna capacitance is a function of frequency, but it can be approximated by a constant factor at any frequency except at $\omega \sim \omega_p$ (see Chapter 5 for details). Actual value of the STEREO/Waves antenna capacitance is measured by [Bale et al., 2008] to be $\approx 63pF$ for a monopole which should be equivalent to twice the capacitance of a dipole. The given value is in good agreement with approximation for $L_{ant} < L_D$ (which is not always the case on STEREO) given by Equation 2.12 that, after replacement of the antenna parameters given in Section 4.1, yields $C_{ant} \approx 31.7pF$ for a wire dipole. From here the antenna gain is given by Equation 2.10 to be $\Gamma \approx 0.49$.

Electron quasi-thermal noise

The signal measured due to quasi-thermal noise is given by Equation 2.35. The argument of the antenna response function defined by Equation 2.21 is kL_{eff}. Since on STEREO we have 90° angle between the monopoles (Figure 4.1) then, following Equation 2.23, $L_{eff} \approx 4.25m$ in the limit $L_{ant} << L_D$. This value of L_{eff} is a rough approximation, but it can work well for STEREO since V_{qtn}^2 is only a small contribution to the power spectrum.

The function $B(k)$ is calculated for κ distribution (defined in Equation 3.1) using Equation 2.36 to be

$$B(k) = \frac{\Gamma\big(\kappa+1\big)}{\pi^{1/2}\kappa^{3/2} k v_{the\kappa} \Gamma\big(\kappa-1/2\big)} (1+z_\kappa)^{-\kappa} \tag{4.2}$$

with $z_\kappa = \omega/\kappa^{1/2} k v_{the\kappa}$ while the longitudinal dielectric permittivity, has been calculated by [Le Chat et al., 2009] to be

$$\epsilon_L(k,\omega) = 1 + \frac{2\pi\omega_p^2}{k^2}\left(\frac{\kappa - 1/2}{\pi\kappa v_{the\kappa}^2} + z_\kappa I_\kappa\right) \tag{4.3}$$

The factor I_κ is given by

$$I_\kappa = \frac{\Gamma(\kappa+1)}{\pi^{3/2}\kappa v_{the\kappa}^2 \Gamma(\kappa - 1/2)} \left[\int_{-\infty}^{\infty} \frac{1}{x_\kappa - z_\kappa}\left(\frac{1}{(x_\kappa^2+1)^{\kappa+1}} - \frac{1}{(z_\kappa^2+1)^{\kappa+1}}\right) dx_\kappa + \frac{i\pi}{(z_\kappa^2+1)^{\kappa+1}}\right] \tag{4.4}$$

where $x_\kappa = v/\kappa^{1/2} v_{the\kappa}$. For general values of κ, this expression requires a numerical integration over x_κ inside the another numerical integration in Equation 2.35. However, for integer values of κ an analytical solution can be obtained using integration by residues. The calculation was performed by [Chateau and Meyer-Vernet, 1991], producing the result

$$\epsilon_L(k,\omega) = 1 + \frac{z_\kappa^2\omega_p^2}{\omega^2} \left(2\kappa - 1 + i z_\kappa \frac{(-2)^{\kappa+1}}{(2\kappa-3)!!}\sum_{p=0}^{\kappa}\frac{(\kappa+p)!}{p!}\frac{1}{(2i)^{\kappa+1+p}(z_\kappa+i)^{\kappa+1-p}}\right) \tag{4.5}$$

which is a much more convenient expression numerics-wise and will be used throughout this Chapter whenever the QTN spectrum is calculated for integer values of the κ index.

The Equation 4.5 has a low frequency limit

$$\epsilon_L(k,\omega \to 0) = 1 + \frac{\omega_p^2}{k^2 v_{the\kappa}^2}\frac{2\kappa - 1}{\kappa} \tag{4.6}$$

from where one can read the Debye length in terms of κ distributions as

$$L_D = \frac{v_{the\kappa}}{\omega_p}\left(\frac{\kappa}{2\kappa - 1}\right)^{1/2} \tag{4.7}$$

that, of course, converges to the Maxwellian limit $L_D = v_{the}/2^{1/2}\omega_p$ for large values of the κ index.

Proton quasi thermal noise

The theoretical expressions for the proton noise are given in Section 2.4.2. Since the STEREO antennas are not far from being perpendicular to the solar wind bulk velocity, the Equation 2.59 is used to calculate the proton contribution. The generalized temperature used is given from Equations 2.58 and 4.7 to be

$$T_e^* = \frac{2\kappa - 3}{2\kappa - 1} T_e \tag{4.8}$$

Electron shot noise

For $\omega < \omega_p$, the shot noise on a wire dipole is approximated by Equation 2.69. The antenna potential is calculated for a given density and temperature using the electron current balance Equation 3.26 where we treat the antenna as an infinite cylinder and use Equation 3.20 to describe relation between the antenna potential and the incoming flux. The $S_{ant}/S_{\perp}$ ratio is given in Section 4.1.

Here, we use values $\Phi_{ph} = 10^{14} m^2 s^{-1}$ and $T_{ph} = 2eV$, which are in the low range of the results given by previous authors and are also lower then the ones obtained in laboratory measurements for $BeCu$ antennas (see e.g. [Spencer, 1975]). Namely, in the space, these parameters are modified by changes in the work function of the surface due to impurities of the material. Also, the secondary emission of electrons (which has been neglected in our calculations) can affect the electron current balance. This makes that the exact values of the photoelectron parameters are unknown and need to be chosen empirically. If these parameters are not correctly chosen, then the systematic error in measurements of T_e will appear. For these purposes we processed a large data set and made histograms of the electron moments, which are then compared with the data from Wind (see Section 4.4 for details). We chose these values as they do not imply any systematic error in our test.

The antenna potential ϕ has been calculated for wide range of electron densities and temperatures and is given on Figure 4.2. For conditions of quiet solar wind ($n_e \approx 2 - 10cm^{-3}$, $T_e \sim 10 - 15eV$) value of the potential is $\phi \approx 3 - 8V$. This produces the correction to the electron impact rate and, consequently, the shot noise for a factor of $1.3 - 1.6$ but for lower temperatures, usually observed in some CMEs, the correction can increase up to 50% of its initial value and highly affect measured results.

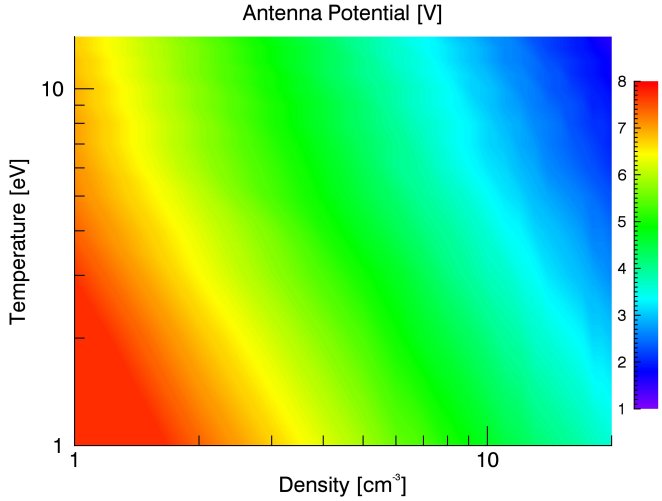

Figure 4.2: Dependence on plasma parameters for the potential of the STEREO antenna. For this example, $\kappa = 4$ is assumed

4.2.2 The LFR instrument

LFR [Bougeret et al., 2008] is a digital spectral analyzer that produces voltage power in three 2-octave bands (Table 4.1), covering frequency range from 2.6 to 153.2kHz with spectral resolution $\delta f/f \approx 8.7\%$. Each one of the bands includes 16 logarithmically spaced frequency channels. Frequency range of LFR is actually the range of dominating electrostatic noise in the solar wind (see Section 4.2.1). Time resolution of measurements is $\approx 38.5s$, and the spectral analysis is performed on board in order to obtain the voltage PSD.

Band	A	B	C
Frequency range [kHz]	2.61-9.58	10.44-38.30	41.77-153.22

Table 4.1: Frequency bands of the STEREO/LFR

Internal noise of the receiver [Bougeret et al., 2008] is at least an order of magnitude below the measured power spectrum. The spectrum expected to be observed by LFR instrument for typical plasma parameters in free solar wind at $1AU$ is shown on Figure 4.3. Shot noise is dominant at low frequencies and gives the shape of the spectrum which is almost linear at logarithmic scale. However, other contributions cannot be neglected in the analysis since sum of the QTN and the proton noise becomes equal to the shot noise at $f \sim 0.6 f_p$. It is worth noting that the spectrum shown is valid only at frequency range where shot noise can be approximated by Equation 2.69 (for $f < f_p$).

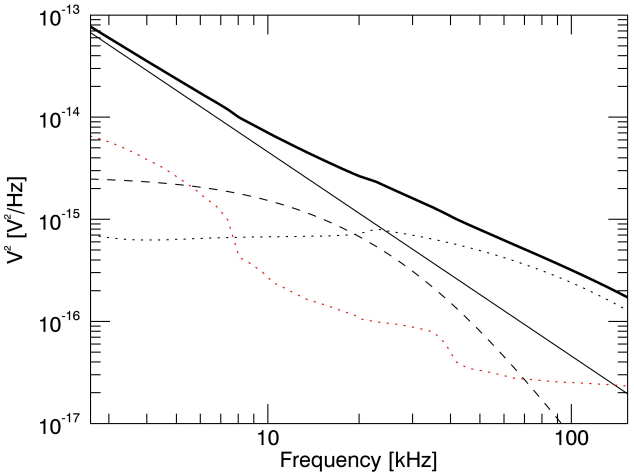

Figure 4.3: Theoretical spectrum of noise observed by STEREO. Shot noise is dominant (black line). Proton contribution is displayed by dashed line and QTN by dotted line. LFR instrument noise is given by red dots. The thick solid line is the total of the noise components. Assumed conditions in the solar wind are: $n = 5cm^{-3}$, $T_e = 10eV$, $\kappa = 4$, $v_{sw} = 340km/s$, $T_p = 4.3eV$, $f_p \approx 21kHz$. Receiver gain is assumed to be $\Gamma \approx 0.5$

4.3 Data analysis

4.3.1 The fitting procedure

The QTN spectrum is a function of 6 independent parameters: electron and proton densities n_e and n_p, electron and proton kinetic temperatures T_e and T_p, solar wind bulk velocity v_{sw} and κ index. In general, these parameters can be obtained separately by fitting the spectrum given in Equation 4.1 [Le Chat et al., 2011]. Unfortunately, on STEREO this is not possible, since short and thick antennas cause the shot noise to overwhelm all other contributions. Also, the condition $L_{eff} < L_D$, valid for STEREO in the free solar wind, makes the plasma peak that is normally used for accurate estimation of electron density, invisible. The almost linear shape of the spectrum (Figure 4.3) allows us to derive only one independent parameter. Consequently, we fit the data with a single free parameter - the electron temperature, while other parameters were taken from PLASTIC instrument. Electron density, not measured by PLASTIC, was approximated to be equal to the proton density plus an additional 8% due to presence of around 4% of α particles in free solar wind [Matthias et al., 2001], which are also not detected by the proton analyzer.

On the other hand, the effective temperature obtained by application of the model to the data is slightly dependent of the value of 'κ' index. This value needs to be assumed before data processing. The 'true' value of κ in the solar wind may vary significantly depending on distance from the Sun [Maksimović et al., 2005, Štverak et al., 2009] and solar wind speed [Maksimović et al., 1997b], and has been measured by various authors (see e.g. [Zouganelis, 2008, Le Chat et al., 2011]). Some details and illustrations on the κ index are given in Section 3.5. Most of the authors evaluate $\kappa \approx 4 \pm 1$ in the slow wind at $1AU$, which is the position of STEREO (Figure 3.5). This parameter affects all three components of the spectrum (electron, proton and shot noise) but, combined, κ value changes the power spectrum by less than 2% for $\kappa \geq 3$ in the case of STEREO. Figure 4.4 represents the level of the power spectrum at $6.2kHz$ calculated using our model. Variation between the signal expected to be observed for $\kappa \geq 2$ (the range of commonly observed κ index at $1AU$, see Section 3.5 for details) is smaller than 10%. In order to avoid multiple parameter fitting of the data set which is almost linear in logarithmic scale, we use the constant value of $\kappa = 4$ further on, as done by some previous authors. This approximation is justified since the error in measurement of T_e that is produced by assuming the constant value of the κ index is less than 3% for $\kappa \geq 3$ due to approximate $n_e\sqrt{T_e}$ scaling of the measured signal. This error is much less than uncertainties that originate from the instrument (Section 4.3.2).

Since the Equation 2.69 only holds for $f < f_p$ [Meyer-Vernet, 1983], all the frequencies above $9.58kHz$ have been excluded from the fitting process (only Band A of the LFR is used). This way we consider only the part of a spectrum below the plasma frequency and each spectrum is fitted using 16 frequency channels.

The main issue of the fitting procedure was filtering of measured spectra by quality and establishing criteria for their usability. Indeed, measured spectra are very sensitive to any kind of 'pollution' by dust impacts, which can appear and cover the thermal noise. This kind of spectra are not taken into account since their usage is propensed to give some unrealistic and incorrect results during the massive fitting procedure applied to the entire STEREO database (10 years, until now, of data with $\sim 40s$ time resolution).

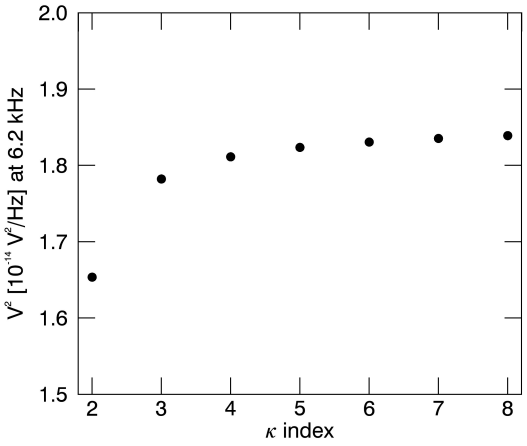

Figure 4.4: Level of the theoretical spectrum at $6.2kHz$ for different values of κ index. Plasma parameters are $n_e = 7.39cm^{-3}$, $T_e = 11eV$, $v_{sw} = 349.1km/s$, $n_p = 7.32cm^{-3}$, $T_p = 6.5eV$. Receiver gain is assumed to be $\Gamma \approx 0.5$. The spectrum level is nearly flat for $\kappa > 3$

Spectra with dust impacts are completely excluded as unusable. They are fairly easy to recognize due to characteristic f^{-4} spectrum characteristic and very high intensities of signal [Meyer-Vernet et al., 2009]. The reason for such high sensitivity of STEREO antennas to dust impacts occurrence close to a monopole, compared to other spacecraft, is the large antenna radius a_{ant} [Pantellini et al., 2012], which causes the signal to be 4-5 orders of magnitude above the usual shot noise signal. These features were used by [Meyer-Vernet et al., 2009] and [Le Chat et al., 2013] to discover and study nanodust impacts on STEREO. Linear fitting of every spectrum is performed. If the slope obtained from linear fit $\lg f, \lg V^2$ is less than -1.8 for entire spectrum or less than -3 for first five data points ($2.6-3.7kHz$), the spectrum is not taken into account. The reason for this treatment is the fact that signals caused by dust can manifest, in certain occasions, only at very low frequencies. The application of the criteria is illustrated on Figure 4.5 for a randomly picked day on STEREO B. The daily summary plot is given on the same graph clearly denoting dust impacts with high intensities, especially in Band A. The spectra with dust show a good match with the spectra below the red line.

4.3.2 Necessity of averaging of the results

The electron kinetic temperature measured by the model described above is very sensitive to the level of power spectrum measured by the receiver in the case of STEREO. Namely, for all three components (QTN, proton and shot noise) the noise level is roughly scaled with $T_e^{0.5}$. This means that the value of measured T_e can vary significantly with any kind of fluctuations in measurements. Figure 4.6 illustrates this effect. It is noticeable that measurement errors of the LFR instrument [Bougeret et al., 2008] are of the order of $\sim 20\%$ and theoretical curves for wide range of temperatures are 'passing through' the instrument uncertainties. This inevitably

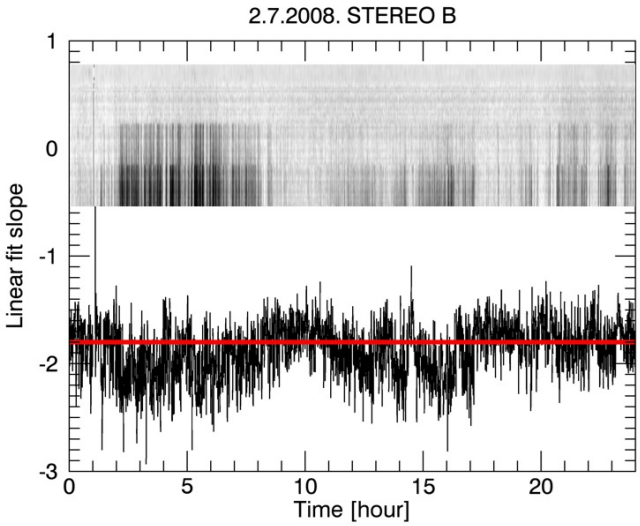

Figure 4.5: The linear fit criteria applied to 2233 spectra during 2.7.2008. on STEREO B. The slopes from $\lg f, \lg V^2$ linear fitting are shown in black. Red line represents the slope equal to -1.8 and all the spectra below the line are excluded. The time shown on the x axis is also valid for the summary plot

leads to a very big dispersion of the results, even for periods when 'true' value of the electron temperature remains approximately constant.

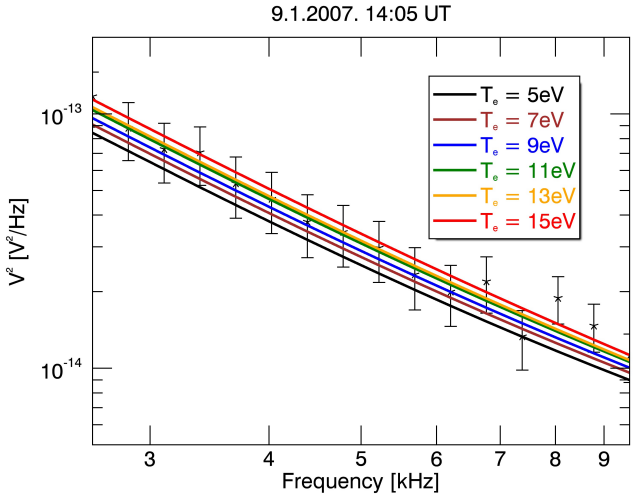

Figure 4.6: Example of LFR spectrum. Measured values are given by asterisk symbols with marked error bars. Plasma parameters measured by Wind (Section 4.4) for given time have the same values as on Figure 4.4, with $\kappa = 4$. Spectra calculated using the model for multiple values of T_e are given in different colors

In order to overcome this effect, averaging of results over certain time interval needs to be performed. This way, the result of the measured electron temperature is given as an average value for the chosen period. To choose the time interval most

suitable for averaging, we compared temperature measurements using the technique described above to measurements performed by Wind. For this we use the same period which was used for the measurement of base capacitance by [Zouganelis et al., 2010]. Figure 4 of that paper shows a histogram of measured C_{stray} values that also confirms the existence of the strong fluctuations described here. Details of the comparison, as well as criteria used to determine the averaging time interval, are given in Section 4.4.

Since, in the process of averaging, we assume that the 'true' value of T_e does not change during the given time interval, value of the error bars are calculated as standard deviations of the mean value of the results during the averaging period $\Delta < T_e >= \sigma/\sqrt{N}$, where N is number of measurements and σ is standard deviation of the measured T_e values during the time interval. This kind of treatment of the averaged temperature error neglects changes of the value of T_e during the given time interval, as well as error of each particular measurement, so the values of the $\Delta < T_e >$ can be (sometimes highly) underestimated.

4.4 Comparison with Wind

4.4.1 Real-time test and averaging intervals

Electron analyzers on both STEREO spacecraft are not functioning properly since launch [Fedorov et al., 2011] and, unfortunately, there is no data on thermal electrons at all, so that validity of the results cannot be confirmed in real-time. In order to validate our results we compared value of T_e derived by the model (Section 4.2.1) to the one measured by Wind when STEREO B was positioned just behind it. Namely, during the observed day (9.1.2007), in the early phase of the STEREO mission, while STEREO B was performing its rotation around the Earth in preparation to start rotating around the Sun, it formed a straight line with the Sun and Wind, which was standardly located at L1 point at $\sim 0.99AU$.

Unfortunately, during the selected period, there was no PLASTIC data so all particle data necessary for the analysis is taken from Wind. For providing electron data on Wind, the Wind/Waves Thermal Noise Receiver (TNR) [Bougeret et al., 1995] plasma peak (clearly visible because of long and thin antennas) was used for a reference value of the electron density, since that is crucial for our obtaining of accurate electron parameters. Using n_e obtained this way, fits of the VDF, as it is measured by Wind 3-Dimensional Plasma (3DP) analyzer [Lin et al., 1995], were performed. Some details of this procedure are given in [Pulupa et al., 2014]. Finally, we applied the fitting procedure described in Section 4.3.1 with parameters n_p and T_p measured by Wind Solar Wind Experiment (SWE) Faraday Cup [Ogilvie et al., 1995], n_e and v_{sw} measured by Wind/3DP (as described above) and $\kappa = 4$. The only fitted parameter was electron temperature which is compared with T_e measured by Wind/3DP. Figure 4.7 presents the results of this comparison.

Electron temperatures from Wind and STEREO B are plotted, showing a good agreement when spacecraft are close to each other (the relative position is shown by the blue line). On this Figure it can be noted that T_e is highly underestimated at the first part of the day (until 8 A.M). The reason for this is a very strong change of the electron density at Wind itself, as Wind/3DP measures $n_e \sim 25cm^{-3}$ during this period, and we conclude that the electron densities did not have the same value

for the two spacecraft. Because of the conspicuous sensitivity of the model to the assumed electron density, the difference of parameters on Wind and STEREO can highly affect results of our test, giving unrealistic values. For this very reason, period before 8 A.M. of this particular day was not used for base capacitance measurement in the previous work of [Zouganelis et al., 2010].

Choice of the time duration on which to perform averaging is a compromise between decrease of the statistical error (assuming that T_e does not change during the time interval) and time resolution of the results, so it needed to be chosen empirically. On Figure 4.7 are represented multiple averaging times. Time statistical error decreases as number of averaged results (time interval) increases. On the other hand, electron temperature is not constant over time, and for longer time intervals results will have larger deviations, depending on how the 'true' value of T_e varies. Consequently, the 'optimal' time interval for averaging of results can be found using these two premises. From the test period shown at Figure 4.7 the 60 minutes time interval has been selected and used further on, since the uncertainties of the measured T_e do not decrease for longer averaging periods.

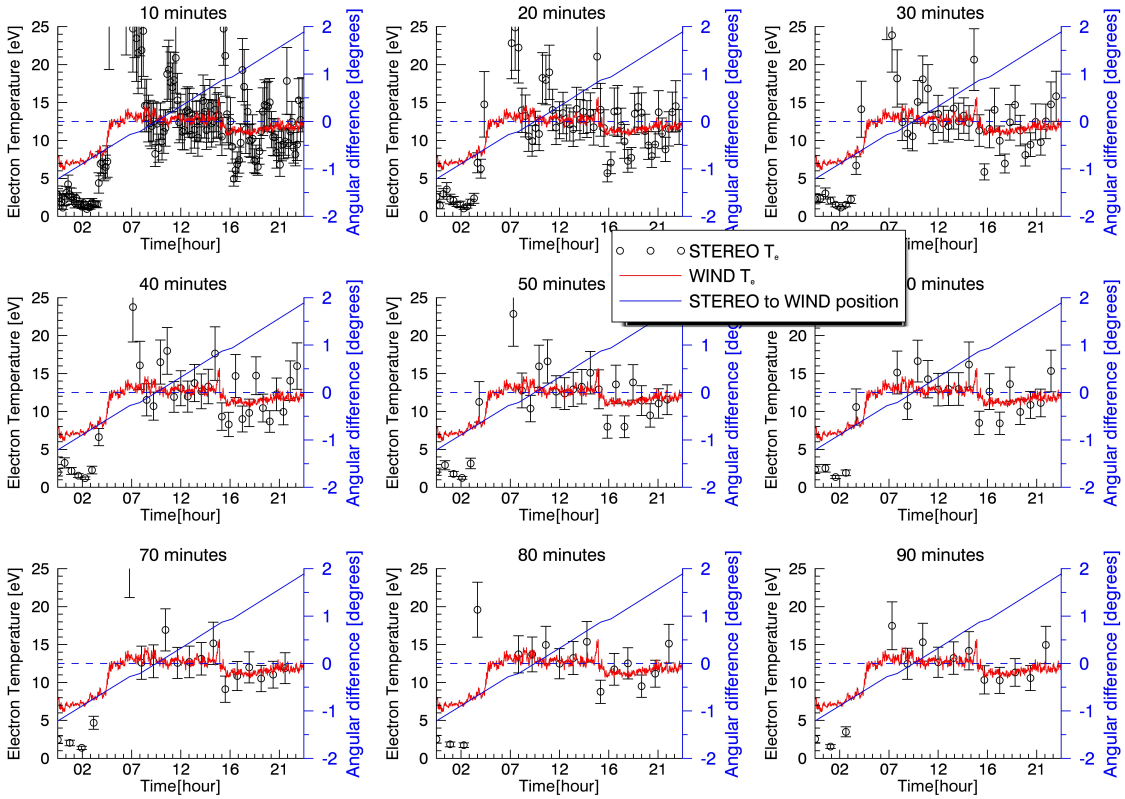

Figure 4.7: Electron temperature as measured by STEREO B/LFR on 9.1.2007 averaged over different time intervals (circles). T_e from Wind/3DP data used for comparison is given in red. Blue line stands for the angle between lines that connect Wind and the Sun and Wind and STEREO B

4.4.2 Processing a large data set

For additional verification, all the STEREO A spectra from 10 months (March to December) in year of 2007 have been processed and histogram plots were compared with Wind measurements. It is worth noting that around 85% of this period is covered by the nanodust bursts [Zaslavsky et al., 2012], so number of spectra used from STEREO A is much smaller than number of those taken from Wind, but still enough to perform the statistics. Results are given on Figure 4.8. It is noticeable that PLASTIC gives more scattered values for proton density compared to well calibrated Wind measurements. Although both histograms peak at the same value ($\approx 2cm^{-3}$) values of n_p are, in general, underestimated by PLASTIC but higher densities (especially in the range $n_p = 5 - 8cm^{-3}$) are measured more often than on Wind. Consequently, measured electron temperature is overestimated and also existence of low-temperature 'tail' can be noticed. The source of this tail is due to measurements where overestimation of density is evident on PLASTIC. To confirm this statement, we made a 'test' histogram (not shown here) where we exclude all measurements with $n_p > 5cm^{-3}$. On this histogram, the low-temperature tails do not exist.

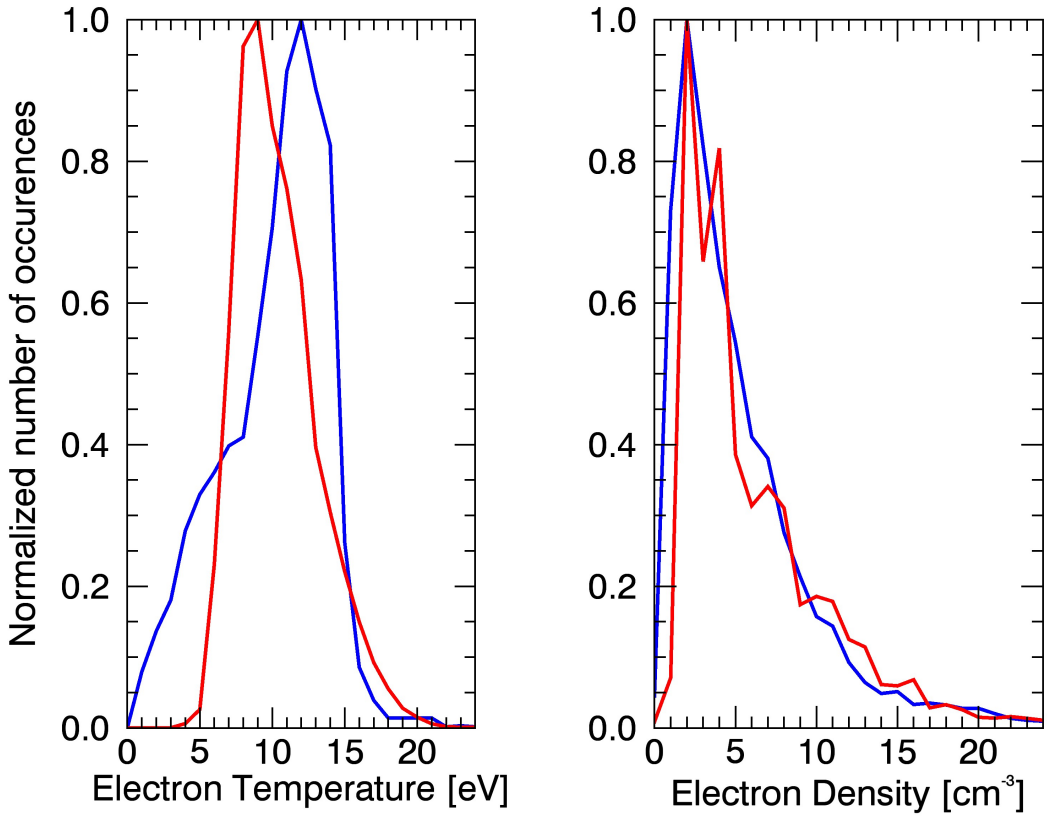

Figure 4.8: Histograms of electron density and temperature measured by Wind/3DP (red lines) and evaluated for STEREO (blue line) for ten months during the year of 2007. Here, as electron density is given the proton density measured by PLASTIC increased by 8% (Section 4.3.1) and electron temperature is calculated by applying our model to the STEREO A/LFR data

In order to verify the method, we compare histograms of $n_e\sqrt{T_e}$. Result is shown on Figure 4.9 and there is relatively good agreement between measurements from both spacecraft. Dispersion of results that originates from PLASTIC can also be noticed on this Figure. Processing of PLASTIC data has been approached in different ways several times during the STEREO mission and, as soon as values of plasma density are updated, we will be able to provide reliable measurements of the electron temperature.

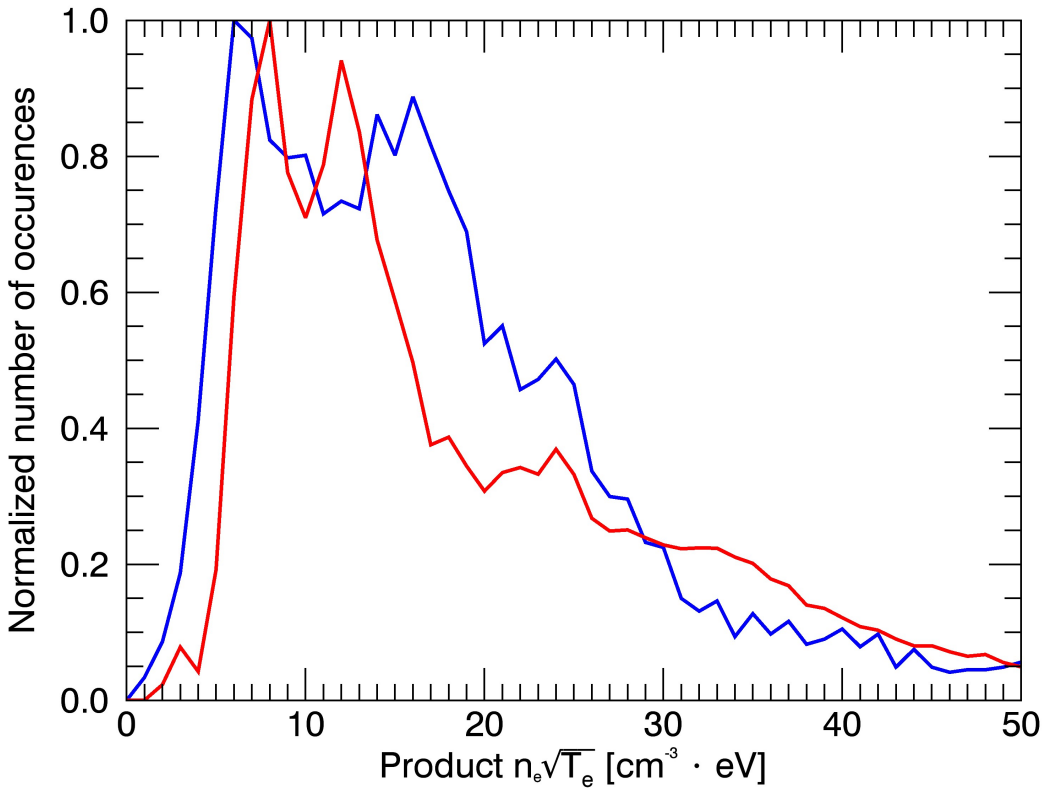

Figure 4.9: Histogram $n_e\sqrt{T_e}$ measured by Wind/3DP (red line) and STEREO (blue line) for the same data set as on Figure 4.8

4.5 STEREO electron moments database

Based on the tools given in this Chapter, the continuous survey of the electron moments can be made for 10 years of the STEREO data. At this point, it is possible to make a database of $n_e\sqrt{T_e}$. The time interval for a single data point can be chosen arbitrarily but taking shorter intervals will significantly increase the uncertainties (Figure 4.7). The uncertainties themselves still need to be accurately determined since they are strongly dependent on the PLASTIC measurements errors (the PLASTIC has been considered errorless in the present study) and are expected to be $\sim 40\%$. The work on this preliminary data is currently in progress.

In order to improve the procedures described in Section 4.3 several steps forward can be made. First, the errors of each particular fit need to be taken into account. This would imply that, if we note ΔT_{ei} as one σ uncertainty of i-th measurement, the average over the time interval would be calculated from

$$\overline{T_e} \sum_i \frac{1}{(\Delta T_{ei})^2} = \sum_i \frac{T_{ei}}{(\Delta T_{ei})^2} \tag{4.9}$$

so the most probable value should be an average of measurements, using the squared reciprocals of their uncertainties as weights.

The accuracy of the method would be significantly increased if the entire 48-point spectrum would be fitted with an adequate model. The Equation 2.69 presently used is correct only below the plasma frequency and we are forced to exclude two thirds of measured points. The precise theory is done by [Meyer-Vernet, 1983]. However, the numerics required to follow this theory is very robust, even for thermal plasma, which makes it inconvenient for processing of large data sets. This model requires additional work on precision and, especially, optimization.

The processing of the entire spectrum would be also helpful in resolving another important issue of this work. Namely, the measured temperature values can vary significantly due to photoelectron parameters Φ_{ph} and T_{ph}. As explained above, these values need to be empirically chosen in order to reduce systematic errors, so their affection to the results should be as low as possible. This is hard to accomplish when only the low frequency part of the spectrum is used. It is also worth noting that the 'true' value of the photoelectron flux is changing over time due to changes in the antenna surface work function, so a more comprehensive analysis is required in this topic.

Beside the additional work described in this Section, some 'fine tuning' can also be done to the fitting procedure. First of all, it was shown that the value of the κ index is partially dependent on the solar wind speed [Maksimović et al., 1997b] where smaller κ corresponds to the fast wind. Further on, the solar wind helium abundance is considered constant in the present study. In reality, this value varies with the solar wind speed and the solar cycle (Section 2.1.2). Several models on this topic have been developed (see e.g. [Ogilvie and Hirshberg, 1974, Matthias et al., 2001]) but even with usage of these models the percentage of the α particles used in our analysis remains just a decent approximation.

After finalizing the work on all the improvements given above and their implementation into the method described throughout this Chapter, realization of the final version of the electron temperature database will become possible. Including of the entire LFR spectrum should, as explained above, significantly decrease the measurement errors. The final values of the uncertainties are hard to predict at this point since they will remain dependent on the uncertainties of PLASTIC but they are expected to still be higher than standard values provided by particle analyzers on other missions.

Chapter 5

QTN spectroscopy in weakly ionized collisional plasma

The technique shown in Chapters 2 and 3 has been widely used for in situ space plasma diagnostics in both solar wind and planetary magnetospheres (see e.g. [Moncuquet et al., 2005, Le Chat et al., 2011]), that is, in nearly perfectly collisionless plasma. On the other hand, laboratory and ionospheric plasmas (especially at lower ionospheric layers), dominantly consist of neutral atoms and molecules, which frequently collide with electron population. The antenna impedance in a collisional plasma has been theoretically treated in the hydrodynamic approximation (which is reliable above the plasma frequency) by [Balmain, 1964] and measured in various rocket (see e.g. [Hoang, 1972, Spencer and Patra, 2015]) and laboratory experiments (see e.g. [Hall and Landauer, 1971, Blackwell et al., 2007a, Blackwell et al., 2007b]).

In this Chapter, we will accommodate this technique to weakly ionized collisional plasmas using kinetic approach [Martinović et al., 2016a]. Therefore, we propose, for the first time, a treatment valid below the plasma frequency, which was not the case for the hydrodynamic models. It turns out that the QTN spectrum is modified both at low frequencies, increasing level of the power spectrum, and around the plasma frequency, where collisions damp the plasma oscillations and therefore broaden and reduce amplitude of the plasma peak, while the spectrum at high frequencies is nearly unmodified compared to the collisionless case. Based on these results, we show that the QTN spectroscopy enables independent measurements of the collision frequency, electron density and temperature if the ratio of collisional to plasma frequency is $\nu/\omega_p \geq 0.1$. The method presented here can be used for precise estimation of plasma parameters in laboratory devices and unmagnetized ionospheres. The opposite is also possible, as the method itself can be studied for cases of different antenna geometries in controlled environment of a plasma facility. On the other hand, application in the ionosphere of Earth is possible but limited to small, low frequency range due to magnetic field influence.

In Section 5.1 we calculate QTN generic spectrum for collisional plasma and explore some of its features for wire dipole antennas. Double sphere antennas are not investigated in detail in this Chapter, for two reasons. First, these two commonly used geometries show very similar behavior of the QTN spectra for $\omega \leq \omega_p$, with only some quantitative differences [Meyer-Vernet and Perche, 1989] and it is also the case for corrections due to collisions. Second, it was proven by [Meyer-Vernet, 1983] that shot noise overwhelms the signal on sphere antennas at low frequencies.

This is why spherical dipoles are usually avoided in the QTN measurements.

In Section 5.2 we investigate the applicability of our theory to ionospheric and laboratory plasmas. Magnetic field in the ionosphere of Earth causes fundamental modifications to the entire spectrum. Because of this, usage of the QTN kinetic collisional theory for unmagnetized plasma is still possible, but is strictly limited to very low frequencies and tiny frequency range around cyclotron harmonics. We further on deal with problems in real laboratory plasmas, defining the conditions for which the theory is valid and usable in experiments. It is concluded that absolute value of the antenna potential should be as low as possible in order to avoid unwanted effects of the plasma sheath, while, as already noted in Section 2.3.3, usage of tiny dipoles is obligatory in order to preserve the simple form of the antenna current distribution.

5.1 Thermal noise in collisional plasmas

For plasmas in thermal equilibrium, the thermal noise power spectrum is described by Nyquist formula (Equation 2.44), where the wire dipole antenna resistance is given by Equation 2.42.

Plasma dielectric function $\epsilon_L(\omega, \vec{k})$ can be obtained for collisional, weakly ionized, unmagnetized plasma using Boltzmann equation

$$\frac{\partial f(\vec{v})}{\partial t} + \vec{v} \cdot \nabla f(\vec{v}) - \frac{e}{m}\vec{E} \cdot \frac{\partial f(\vec{v})}{\partial \vec{v}} = \Xi_v[f(\vec{v})] \tag{5.1}$$

Here, $\Xi[f(\vec{v})]$ is a collisional operator that depends on the nature of collisions. In this study, we consider electron-neutral collisions, in which case the it can be written in the fairly simple following form [Bhatnagar et al., 1954].

$$\Xi_v[f(\vec{v})] = -\nu[f(\vec{v}) - f_0(\vec{v})] \tag{5.2}$$

where $f_0(\vec{v})$ is an equilibrium electron VDF, assumed to be Maxwellian in a collisional plasma. The longitudinal dielectric permittivity is possible to derive using Equation 5.1 and set of Maxwell and charge continuity equations. This straightforward but lengthy calculation was performed by many authors (see e.g. [Alexandrov et al., 1984]) to obtain

$$\epsilon_L(k, \omega) = 1 + \frac{1}{k^2 L_D^2} \frac{1 + (z + i\nu')Z_0(\zeta)}{1 + i\nu' Z_0(\zeta)} \tag{5.3}$$

Here we use substitutions

$$\begin{aligned} \zeta &= z + i\nu' \\ z &= \frac{\omega}{k v_{the}} \\ \nu' &= \frac{\nu}{k v_{the}} \end{aligned}$$

Using Equations 2.42 and 2.44 the thermal noise can be calculated numerically and is shown on Figure 5.1. It is noticeable that the plasma peak is damped and that

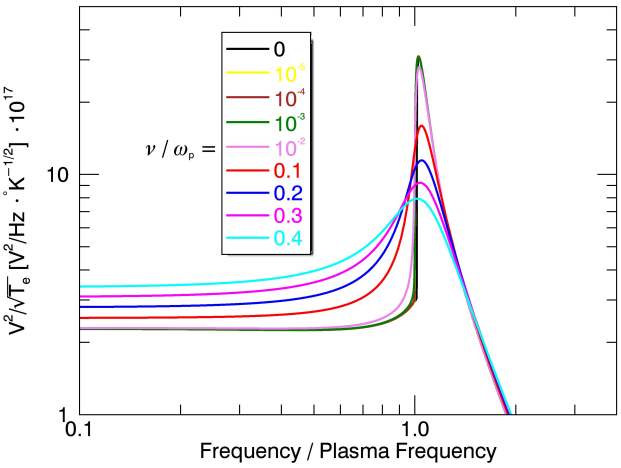

Figure 5.1: QTN power spectra observed by a long wire dipole antenna ($L_{ant}/L_D = 16$) for different values of the collision frequency. Result for $\nu = 0$ is identical as the one in Section 2.4.1

its location in the spectrum is slightly varying. Both features are important when $\nu/\omega_p > 10^{-2}$ and can be directly used to measure the electron density, temperature and collision frequency if the spectral resolution is satisfactory. The low frequency part of the spectrum is evidently increased for $\nu/\omega_p > 0.1$ and this effect is important to take into account in order to avoid overestimation of the electron temperature when it is examined using the 'thermal plateau' below ω_p (Section 2.4.1). On the other hand, the high frequency part is almost completely unmodified by collisions. It is important to note that the trend shown on Figure 5.1 is commonly present for long dipoles and change in the L_{ant}/L_D parameter only changes the peak to plateau signal ratio (see Section 5.1.3 for details). We give a closer insight below for each of these spectral domains.

5.1.1 Low frequency limit

If we write the plasma dispersion function in the form of the imaginary error function as

$$Z_0(\zeta) = \pi^{1/2} e^{-\zeta^2} [-erfi(\zeta) + i] \tag{5.4}$$

it can be approximated by series for small values of z as

$$Z_0(\zeta) \approx i\pi^{-1/2} e^{\nu'^2} erfc(\nu') - 2z - 2i\nu' z^2 + ... \tag{5.5}$$

where $erfc(x)$ stands for the complementary error function. Putting Equation 5.5 into 5.3 and then into Equation 2.42, after some tedious calculations we have

$$R_{ant}(\omega \to 0, \nu) = \sqrt{\frac{8}{\pi^3}} \frac{L_D}{\epsilon_0 \omega_p} \int_0^\infty \frac{kF(kL_{ant})}{\left[1 + k^2 L_D^2\right]^2} M(\nu) dk \tag{5.6}$$

with

$$M(\nu) = \frac{e^{\nu'^2} erfc(\nu')}{\left[1 - \nu'\pi^{1/2} e^{\nu'^2} erfc(\nu')\right]} \tag{5.7}$$

This term can be simplified for small values of ν' as

$$M(\nu \to 0) \approx 1 + \pi^{-1/2}(\pi - 2)\nu' + (\pi - 3)\nu'^2 + ... \tag{5.8}$$

Comparison with numerical results is shown on Figure 5.2. It is worth noting that using only the first term from Equation 5.8 gives error less than 0.15% for $\nu/\omega_p < 10^{-2}$ and less then 2% for $\nu/\omega_p \sim 0.3$ compared to the precise value calculated using Equation 5.3, while the computation time differs for a factor of ~ 20. This approximate expression is valid for the entire frequency range below ω_p.

In the collisionless limit, $\nu = 0$ implies $M = 1$ and we turn back to the well known expression that can be derived using the usual Debye screening dielectric function $\epsilon_L(\omega, \vec{k}) = 1 + (kL_D)^{-2}$.

The factor M can also be calculated for large values of ν' to be

$$M(\nu \to \infty) \approx 2\pi^{-1/2}(\nu' + \nu'^{-1}) + ... \tag{5.9}$$

and for frequent collisions we have

$$R_{ant}(\omega \to 0, \nu \to \infty)] = \frac{4}{\pi^2 \epsilon_0} \frac{\nu}{\omega_p^2} \int_0^\infty \frac{F(kL_{ant})}{\left[1 + k^2 L_D^2\right]^2} dk \tag{5.10}$$

yielding clear linear increase of the power spectrum level with ν, while the integrand is not depending on the collision frequency. Using Equation 5.10 gives uncertainty less than 5% for $\nu/\omega_p > 4$ and less than 1% for $\nu/\omega_p > 8.5$. These estimates are correct for $\omega/\omega_p < 0.1$. Above these frequencies, the approximation causes errors above 20% and is not useful for quick estimation of temperature or collision frequency.

5.1.2 High frequencies $\omega > \omega_p$

High frequency part of the QTN spectrum is directly proportional to the plasma pressure and can be used to determine the plasma temperature (see e.g. [Issautier et al., 1999, Le Chat et al., 2011]). How is this modified by the collisions?

In the high frequency (hydrodynamic) limit, we can derive the expression for dielectric permittivity by developing Equation 5.3 in series for $z \to \infty$ [Fried and Conte, 1961]. We keep only terms of the zeroth and first order in ν/ω and also neglect terms proportional to $(\nu/\omega)(k/\omega)^2$ to obtain the result

$$\epsilon(k, \omega > \omega_p) = 1 - \frac{\omega_p^2}{\omega^2 - i\omega\nu - 3k^2 v_{the}^2/2} \tag{5.11}$$

This expression is equivalent to the one obtained using the linearized hydrodynamic equations with a pressure term $p_e = 3n_e k_b T_e$. Also, by omitting the last term in the denominator we converge to the well known result for a cold plasma [Balmain, 1964]. Using Equation 5.11, the integral in Equation 2.41 can be calculated analytically (analogy with Equation 2.46 gives the same result), yielding

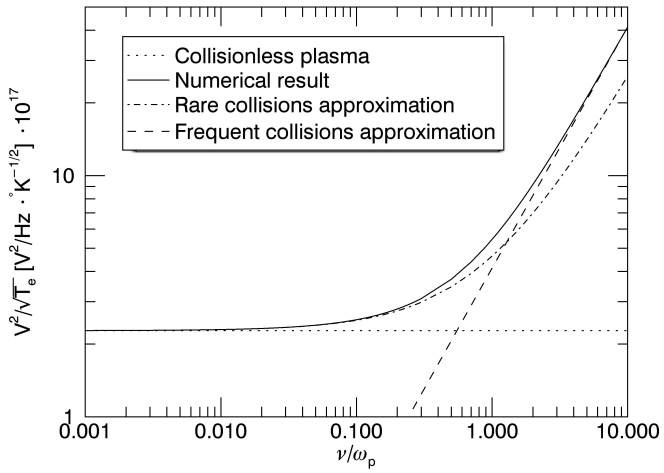

Figure 5.2: Level of the QTN on a wire dipole antenna ($L_{ant}/L_D = 16$) at $\omega = 0.01\omega_p$ computed numerically using Equation 5.6 and first order approximations given by Equations 5.8 and 5.9

$$Z_{ant}(\omega) = \frac{2F(k_* L_{ant})}{3\pi\epsilon_0 \omega L_D^2 k_*} \tag{5.12}$$

with complex pole

$$k_* = \frac{1}{L_D}\sqrt{\frac{1}{3}\left(\frac{\omega^2}{\omega_p^2} - 1 - i\frac{\omega\nu}{\omega_p^2}\right)} \tag{5.13}$$

From Equation 5.13 it is notable that if $\omega - \omega_p >> \nu$ then $k_* \approx (\sqrt{3}L_D)^{-1}(\omega^2/\omega_p^2 - 1)^{1/2}$ and the level of high frequency part of the spectrum is independent of ν, bringing us back to Equation 2.47. This means that the expressions given at [Meyer-Vernet and Perche, 1989] stay valid for high frequencies. This also implies that expressions given by [Chateau and Meyer-Vernet, 1991] for long antennas can be used to quickly estimate T_e from high frequency part of the spectrum.

5.1.3 Resonance region $\omega \sim \omega_p$

Around the plasma frequency, the hydrodynamic approach described by Equation 5.12 gives only approximate results and full QTN expression that includes Equation 5.3 needs to be used.

Since location of the plasma peak, depending mostly of n_e and very slightly of T_e (see Equation 2.49), is shifted due to collisions, this effect needs to be taken into account for accurate estimation of the electron density. On the other hand, damping of the plasma oscillations near the plasma frequency results in sharp decrease of the signal at the peak if $\nu/\omega_p > 10^{-2}$. Comparison of the peak and the low frequency thermal plateau intensities is illustrating this effect. Both of these parameters are numerically calculated for multiple values of ν/ω_p in the L_{ant}/L_D range of interest

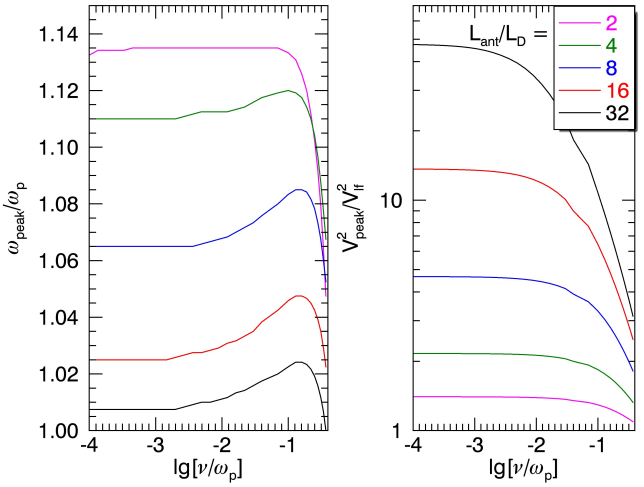

Figure 5.3: Location (left) and intensity (right) of the plasma peak observed by a wire dipole antenna in collisional plasma for some of L_{ant}/L_D ratios. The uncertainties are less than 0.3% for both plots

and given on Figure 5.3. For $\nu/\omega_p > 0.5$, the plasma peak completely disappears from the spectrum and is not practically useful for estimation of n_e.

5.1.4 Antenna capacitance

We define the antenna capacitance as $C_{ant} = 1/\omega Im[Z_{ant}(\omega)]$. In order to examine the imaginary part of antenna impedance at low frequencies we perform a similar calculation as in Section 5.1.1 to obtain a simple expression $Re[(\epsilon_L(k, \omega \to 0))^{-1}] = (1 + (kL_D)^{-2})^{-1}$, identical to the collisionless case. Similarly, for the high frequency part of the spectrum the hydrodynamic treatment described in Section 5.1.2 can be used, again concluding that collisions do not affect the signal on high frequencies. This implies that well known analytical expressions for both dipole and spherical antennas given in Section 2.3.2 are still valid in both low and high frequency limit.

On the other hand, for $\omega \sim \omega_p$ the antenna capacitance increases and is strongly peaked at the plasma frequency for $L_{ant}/L_D > 5$ ([Schiff, 1970, Nakatani and Kuehl, 1976]). The effect of collisions is visible through 'damping' of the plasma oscillations in similar way as for the QTN spectra, with the peak disappearing for $\nu/\omega_p > 0.1$. An example of the dipole antenna capacitance in a collisional plasma is given on Figure 5.4, showing that the collisional effects become important for $\nu/\omega_p \geq 10^{-2}$.

5.2 Practical consequences

As described in Chapter 2, the QTN spectroscopy is routinely used in the solar wind, providing independent measurements of the electron density and temperature. The solar wind plasma is practically collisionless, while ionospheric and laboratory plasmas have considerable amount of neutral atoms and molecules that collide with electrons and can affect the power spectrum in the way described in Section 5.1. In order to measure the plasma density and temperature in the collisional plasmas

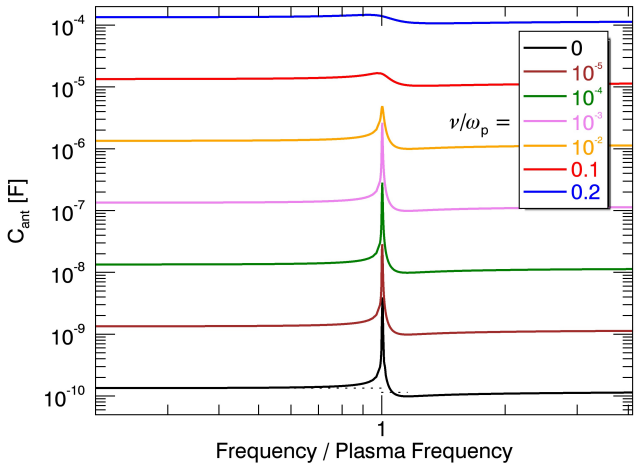

Figure 5.4: Example of the antenna capacitance for different values of the collision frequency for dipole antenna at $L_{ant}/L_D = 16$. Dotted points present the theoretical limits for low and high frequencies. The results are shifted for a decade for clarity

as accurately as it is done in the solar wind by using the method presented here, along with estimating the collision frequency as third independent parameter, one needs to be aware of the limiting factors that appear in real environments. In this Section, we give an overview of 'terms and conditions' for applicability of the theory presented above.

5.2.1 In the ionosphere of Earth

The main issue for applying the theory given in Section 5.1 is presence of the magnetic field in the lower ionosphere, having value around several tens of μT and creating electron cyclotron resonance at $\Omega_e \approx 5 - 7MHz$. Full adaptation of the QTN spectroscopy to magnetized collisional plasma would assume implementing the solution of Equation 5.1 with both magnetic and collision terms included into the theory presented in Chapter 2. This is a very complicated task and is far beyond the scope of this work, although the necessity of adapting the QTN spectroscopy for magnetized anisotropic plasma may appear in near future (see Section 6.1 for details). On the other hand, as described below, there are some areas where we actually can obtain a lot of information about the plasma parameters by measuring the QTN. In this subsection, we limit our discussion only to low frequencies since for $\omega > \omega_p$ the spectrum is well explained by the hydrodynamic approach [Balmain, 1964].

The effects of collisions (in the quiet ionosphere) start becoming notable for $0.01 < \nu/\omega_p$ at $\sim 120km$ altitude (dayside) [Bilitza et al., 2011] while at $\sim 85-90km$ (approximately the lowest altitude where electron density is still measurable), the collisional effects are expected to be dominant in the QTN spectrum as $\nu/\omega_p \sim 0.5$. In this range of altitudes, the angular plasma frequency of $\omega_p \sim 0.1 - 5MHz$ and the electron temperature of $T_e \sim 0.02 - 0.2eV$ are standardly measured.

From the numbers given above it is clear that in this region we have $\omega_p < \Omega_e$. The

dielectric permittivity function for the magnetized, collisionless, isotropic plasma is given as [Stix, 1962]

$$\epsilon_L(k,\omega,\Omega_e) = 1 + \frac{k_{||}^2}{k_\perp^2} + \frac{1}{k_\perp^2 L_D^2}\alpha(q,\lambda,\phi) \tag{5.14}$$

with

$$\alpha(q,\lambda,\phi) = \sum_{n=-\infty}^{\infty} e^{-\lambda} I_n(\lambda)\left[1 + z_{||} Z_0\Big(z_{||} - \frac{n}{r}\Big)\right] \tag{5.15}$$

where $z_{||} = \omega/k_{||}v_{the}$, $\lambda = (k_\perp v_{the}/2\Omega_e)^2$, $r = k_{||}v_{the}/\Omega_e$ and I_n is the modified Bessel function. Further on, for a long dipole ($kv_{the} << \omega_p$) at low frequencies we can write $\alpha(q,\lambda,\phi)$ as series for small arguments z and λ, along with series of the plasma dispersion function for large argument r^{-1} to obtain

$$\alpha(q,\lambda,\phi) = 1 + z_{||} Z_0(z_{||})(1+\lambda) \tag{5.16}$$

On the right-hand side of Equation 5.16 we recognize the solution analogous to one for the unmagnetized plasma given by Equation 2.39 and its correction due to collisions is given by Equation 5.3. Since we know that $kv_{the} << \Omega_e$, the additional term which scales with λ is negligible and we conclude that Equation 5.6 stays valid at low frequencies. This is somewhat expected result since at low frequencies the permittivity is determined by the Debye screening, which is not affected by the magnetic field. For $\omega \sim \omega_p$ the Equation 5.16 is not viable and the QTN theory for magnetized plasma needs to be done in order to interpret the measured spectra.

5.2.2 Laboratory plasmas and unmagnetized ionospheres

Laboratory plasma chambers can be vacuumed to very low pressures and mirror the conditions of the lower ionosphere (see e.g. [Hall and Landauer, 1971, Gekelman et al., 1991]). Primary purposes of experiments with ionospheric-like plasmas are studying of spacecraft wakes [Pigache, 1973] and ion and neutral flows in ionospheric or tokamak plasmas [Livesey and Pritchett, 1989, Wallace et al., 2004].

Beside the diagnostic studies, QTN spectroscopy can be used for precise calibration measurements of plasma parameters in a laboratory device, where the external magnetic field can be completely annulled in the system [Harp, 1964, Graf and Jassby, 1967]. In these unmagnetized plasmas, the entire QTN spectrum can be used for precise plasma diagnostics - examining the electron temperature and the collision frequency from the low frequency part of the spectrum, plasma density (with collisional corrections given in Section 5.1.3) from the resonance region and the electron temperature alone from the high frequency part. This provides independent measurements of n_e, T_e and ν with assumption that the plasma VDF is Maxwellian and is the only technique able to perform direct precise measurements of the collision frequency in laboratory plasmas using the wide frequency range, both below and above the plasma frequency. All these features noted for laboratory experiments also stay valid for ionospheres with negligible magnetic field, ones of Mars [Hanson and Mantas, 1988, Acuna et al., 1998] and Venus, where the QTN signal around the plasma frequency was clearly observed during the CASSINI flyby

[Gurnett et al., 2001] (unfortunately on too high altitudes for collisional effects to be noticeable).

On the other hand, the laboratory devices can be used to improve the QTN spectroscopy itself by exploring the antenna response functions. Namely, dipole can be realized with an arbitrary angle and/or with finite gap between the antenna arms, while for real double sphere antennas, each sphere needs to be placed on a boom. For these irregular geometries, the antenna response function, defined by Equation 2.16, becomes very complicated and in most cases not possible to calculate analytically, so it could be derived from the QTN spectra observed in controlled conditions where plasma parameters are known. This is the way to explore the effects of previously not used antenna geometries.

5.2.3 Standard problems and limitations

If the antenna potential is high compared to the thermal energy of electrons (which is unlikely in the solar wind but can be the case for both ionospheric and laboratory plasmas) then the plasma sheath effects can become significant. This is the problem that has been dealt with in many different ways in the past. The strict kinetic treatment is possible only in the ideal spherical geometry and even then is very complicated [Buckley, 1966]. This is the reason why many authors came up with various models of the plasma sheath where the most popular one is the model of the sheath as a cylindrical vacuum region around the dipole and the plasma is assumed to be homogeneous up to the surface of the sheath, studied in detail by [Meyer et al., 1974]. Another, simpler model where capacitance of the vacuum sheath is in series with the antenna capacitance is also commonly used, producing satisfying agreement with experimental results (see e.g. [Balmain, 1969, Hall and Landauer, 1971]). The main issue of all these models is dependence of the sheath thickness, which is itself the unknown parameter that highly affects the results, making the measurements less accurate.

Thus the most efficient way to go around the complicated sheath problematic and obtain best results from the QTN spectroscopy might be usage of biased antennas with collapsed sheath. In general, perturbation of the surrounding plasma and attracting/repelling of the particles depend of the ratio of antenna potential to particles thermal energy, as explained in detail in Chapter 3, and the sufficient condition for the plasma to be negligibly perturbed by the antenna is this parameter to be close to zero. This condition is achievable in both ionospheric and laboratory plasmas with biased antennas. Good example of this approach is given by [Balmain, 1964], where the experiment with collapsed sheath shows decent agreement with the hydrodynamic theory. However, this approach, even though it can be very efficient in laboratory, has a downside when probing the ionospheric plasma. Namely, biasing the antenna abolishes the balance between the fluxes of photoelectrons and plasma electrons given by Equation 3.26 as, instead of the antenna charging, the biasing current makes up for the loss of photoelectrons. This can significantly increase the photoelectron flux and, consequently, the shot noise at low frequencies as described in Section 2.4.3, and the shot noise signal will mostly depend on Φ_{ph} (Section 3.5), that is, on the properties of antenna surface material.

Another potential issue is the current distribution on a wire dipole antenna. In this study the dipole antenna current is assumed to be triangular. As noted

in Section 2.3.3 this is a valid approximation below the plasma frequency if two conditions are satisfied. First, the antenna is short compared to the free space wavelength $L_{ant} << c/\omega$ [Balanis, 1997]. Even though plasma frequency in both ionospheric and laboratory plasmas is several orders of magnitude above the one in the solar wind, this condition is still easily achieved, even for a long dipole ($L_{ant} >> L_D$) since $v_{the} << c$. Second, there are no contributions to the antenna current from electromagnetic surface waves. If $a_{ant} \sim L_D$ then contribution of these waves is considerable and the current is not triangular [Meyer et al., 1974]. Consequently, the necessary condition $a_{ant} << L_D$ [Couturier et al., 1981], dictates usage of very thin antennas (ideally a_{ant} should be at least an order of magnitude below L_D) in all of the described environments.

Chapter 6

Conclusions and perspectives

6.1 Quasi thermal noise spectroscopy on Solar Orbiter and Solar Probe Plus

In Chapter 2 the theory of the QTN was presented for non-thermal plasmas described by either two-Maxwellian or κ distributions. However, the VDFs measured by particle analyzers on space missions are also measuring the beam-like component known as the strahl, which is briefly discussed in Chapter 3. Since the strahl is being scattered into the halo while propagating through the heliosphere [Maksimović et al., 2005], neglecting this component is valid only if the spacecraft distance from the Sun is comparable to $1AU$ and, as we move closer to the Sun, it becomes less and less justified. As mentioned in Section 2.1.3, the different models that describe this process exist, but they can only be verified with comprehensive in situ measurements.

This is the reason why the problematic related to the strahl will be important for future missions that are planned to operate in 2020s and are aiming to explore the Solar corona and origins of the solar wind, with the spacecraft traveling over the trajectories that were never explored before. In this Section we will give brief notes on the challenges and potential issues that might appear on the ESA Solar Orbiter and NASA Solar Probe Plus (SPP), related to the QTN spectroscopy.

6.1.1 QTN on Solar Orbiter - predictions

Solar Orbiter is a mission planned to launch during 2018 and is dedicated to bringing us closer to answering several very important questions related to the Sun and inner heliosphere. The origins of the solar wind and its magnetic field will be explored, describing the mechanism and precise locations of its creation in the corona. Beside (and together with) this primary objective, the transition of both particles and fields from the corona to the heliosphere will be studied in detail through investigation of the CMEs, magnetic flux, energetic particles etc.

In order to obtain enough information on these complicated phenomena 4 in situ and 6 remote sensing instruments will work in parallel. The radio measurements will be performed by the Radio and Plasma Waves (RPW) instrument [Maksimović et al., 2007] that will sample wide range of frequencies ($4-1024kHz$) through 128 channels, providing $\delta f/f \approx 4.5\%$ resolution, in order to cover the plasma frequency occurrence on its path from the Earth to $\sim 0.28AU$. The instrument will be equipped with 3 $L_{ant} = 6.5m$ monopoles with average radius of $a_{ant} = 1.27cm$. It is important to

note that the Orbiter heliospheric latitude at the perihelion will gradually increase up to $\sim 30°$ (and even up to $\sim 34°$ during the extended mission). This implies that the perihelion in situ measurements will be performed mostly in the fast solar wind while measurements at larger distances, during the 'cruise phase', will happen mostly in the slow wind close to the ecliptic.

Here we make rough predictions of the QTN spectra expected to be observed by the RPW for the solar wind parameters given in Table 6.1. The spectra are given on Figure 6.1. Contribution of the strahl is not taken into account in the shown plots since no adequate theory exists at this point (even though some preliminary calculations show that the effect of the strahl will be visible mostly in the region just below the plasma frequency [Meyer-Vernet, personal communication]). The issue that appears in previous Chapters related to the shot noise at high frequencies still exists, so results for $f > f_p$ should be taken with some reserve. Considering these two unresolved issues, all the spectra shown here should be observed only as a preliminary insight into a model that needs to be carefully developed in the near future.

Parameter	1AU	0.6AU	0.3AU	Extreme conditions
$n_e[cm^{-3}]$	5	15	55	200
$T_e[eV]$	10	15	26	5
$n_p[cm^{-3}]$	5	15	55	200
$T_p[eV]$	5	8	17	2.5
κ	5	7	10	15
$v_{sw}[km/s]$	350	350	350	1000
$\Phi_{ph}[10^{14}m^{-2}s^{-1}]$	1	3	10	10
ϕ_{corr}	1.36	1.22	1.12	1.39
$L_D[m]$	9.9	6.8	4.8	1.1
$v_{the}[10^6 m/s]$	1.25	1.53	2.01	0.89

Table 6.1: Assumed conditions in the solar wind for various distances from the Sun. ϕ_{corr} is correction of the shot noise due to antenna potential (explained in detail in Chapter 3)

The important question that still needs to be answered is the visibility of the plasma peak on the RPW spectra in the quiet solar wind. Although the plots shown on Figure 6.1 do not look very promising it is important to note that the shot noise that covers the plasma peak is expected to drop close to the plasma frequency [Meyer-Vernet, 1983] so we should develop the accurate generic spectrum (see Section 2.4.3 for details) and wait for some real data in order to discuss this topic in more details.

Nonetheless, even when the necessary model is developed determination of the photoelectron parameters will still be a very important issue. The RPW will be routinely measuring the difference between the spacecraft and the antenna potential. This set of data is difficult to analyze using Equation 3.26 since it introduces photoelectron parameters of the spacecraft as new unknown variables, but the spacecraft floating potential values are possible to estimate using various methods on different instruments as it was done on some previous missions (see e.g. [Pedersen, 1995, Henri et al., 2011]) and used as a useful constrain when determining the antenna potential.

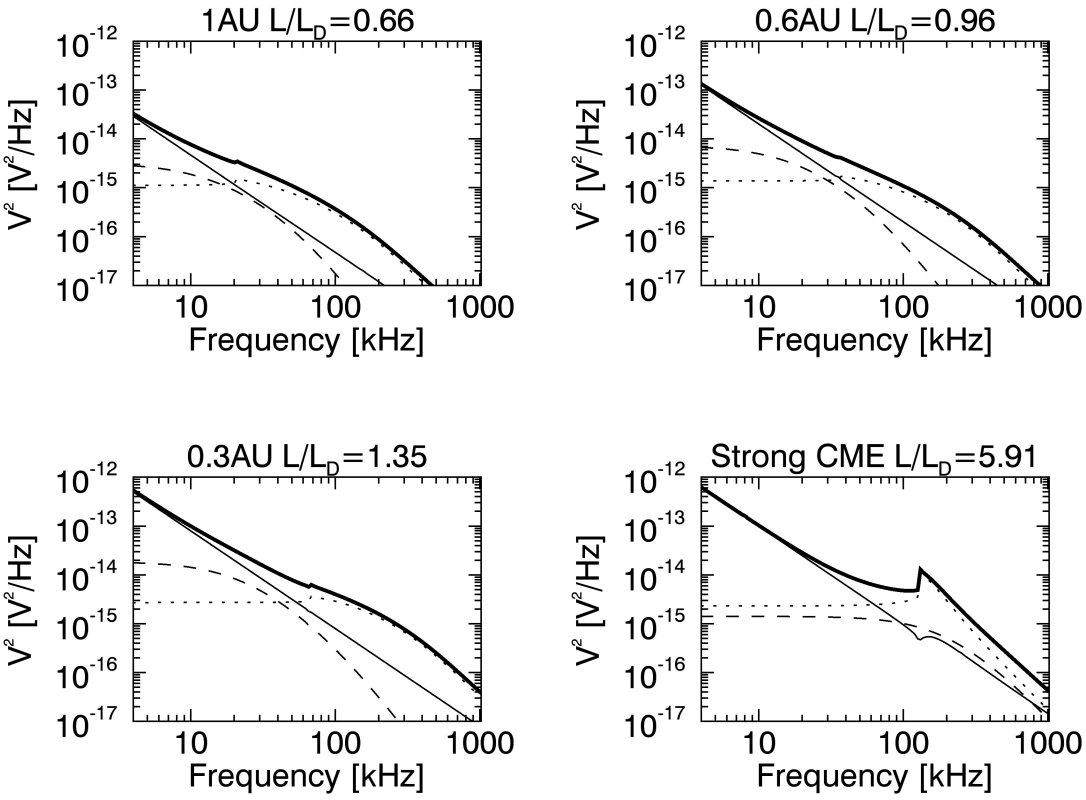

Figure 6.1: RPW generic spectra expected to be observed by the Solar Orbiter at various distances from the Sun. The parameters are given in Table 6.1 and the receiver gain is assumed to be $\Gamma = 0.5$. The receiver internal noise is not taken into account

6.1.2 QTN on Solar Probe Plus - unknowns and challenges

This mission (scheduled for launch at June 30, 2018) will be based mostly on in situ measurements inside the solar corona. The spacecraft is designed primarily for observations at perihelion (9.6 solar radii or $\sim 0.04AU$ from the surface of the Sun), using 4 instruments that will measure magnetic field, ion composition, particle velocity distributions and plasma waves. The Fields instrument [Bale et al., 2016] that will be synchronized with the Solar Wind Electrons Alphas and Protons Investigation (SWEAP) particle analyzer [Kasper et al., 2015] is designed to observe the radio and plasma waves. It is equipped with 4 cross-positioned $L_{ant} = 2m$ antennas with $a_{ant} \approx 0.16cm$ radius and will provide measurements in the frequency range $10kHz - 19.2MHz$ while Fields/LFR, primarily created to observe the QTN, will be able to provide the $\delta f/f \approx 4.5\%$ resolution in the $10kHz - 2.4MHz$ range.

Two major issues arise while predicting the QTN for the SPP. First one is the strahl which requires a comprehensive theoretical work, as already discussed above. Second one is the shot noise. Namely, Fields antennas are positioned closely to the heat shield that will be facing the Sun. Both the shield and the antennas will be biased in order to prevent the surface potential to become too large, either positive or negative. Several biasing algorithms are prepared by the instrument team in

order to cover possible scenarios, depending on the physical processes that will turn out to be dominant at the material surface, as discussed in detail by [Bale et al., 2016]. This is why the particle collection of both spacecraft and the antenna is very hard to predict, even with simulations. Further on, the noise caused by the photoelectrons that leave the surface and then return to it will need to be studied in more detail. This component, briefly discussed in Section 2.4.3, gives nearly white noise for frequencies up to $300kHz$ [Petit, 1975]. For higher frequencies, interesting for the SPP, the δ function of induced antenna current due to an electron impact is not a justified approximation and the antenna potential rise/decay times need to be taken into account in order to obtain satisfying results. All these reasons make predicting of the QTN spectrum that is supposed the be observed by Fields/LFR a very 'thankless' job since too many variables are unknown and the real in-depth analysis will probably need to wait for the real data, and all the theory needed for its interpretation will be developed as the circumstances dictate.

6.2 Concluding remarks

The starting motivation of this work (or at least first part of it) was an attempt to recover the missing electron temperature data from the STEREO/SWEA electron analyzer. This was imagined, at first, as a straight forward task that will use the QTN theory which is well known for decades and the PLASTIC data for the density estimation.

This well known theory is summarized in Chapter 2, providing an overview of the QTN phenomenology, antenna characteristics and the basic equations that introduce connection between the plasma parameters and the power spectral density observed at the antenna terminals. The antenna response to nearby plasma for the frequency range of interest is given by the antenna response function. This function includes dependency from the antenna geometry and current distribution. On the other hand, plasma influence is completely determined by the VDF of particles. From the VDF we derive the dielectric functions and, directly, the mean values of the squared electric field tensor which determines the power spectral density. As contributions from electrons and protons are additive we calculate them separately. Further on, since the QTN theory assumes 'grid' antennas that are transparent for particles, we calculate the correction due to the antenna thickness. The noise signal that originates from this effect is known as the shot noise. This component was usually negligible at most of the antenna configurations used in previous missions and no demands for its strict modeling appeared before. On the other hand, the shot noise is dominant for the case of STEREO and it was necessary to make a closer insight into this problematic. This is the reason why we needed to deal with several problems that were not rigorously treated by previous authors.

These issues are related to the particle impacts/emission to/from the antenna and are described in detail in Chapter 3. The equilibrium state at the antenna surface assumes the current (flux) balance between particles that arrive to the antenna surface from the surrounding plasma and ones that are emitted from the surface due to photoelectric effect. As the flux of photoelectrons is usually for an order of magnitude larger then the flux of electrons impacting the antenna at zero potential then the antenna surface charges in order to equalize these two components. Using the orbit limited theory, we calculated the equilibrium particle flux (that determines

the shot noise) as a function of the surface potential for a plasma described by κ distributions, proving that the particle collection is considerably increased, for both cylindrical and spherical collectors, due to presence of the supra-thermal particles which are ubiquitous in the solar wind. As the surface potential is playing a key role in determination of the particle flux, we also implement the results obtained into the current balance equation in order to calculate the potential as a function of the plasma density and temperature. These results give a total 'correction' factor for the shot noise compared to the case where the potential is considered to be very small (this approximation was used by most of the previous authors when dealing with the shot noise). It turns out that the corrections obtained are not negligible and change the value of the electron temperature measured for a factor of 2 or more whenever the shot noise is dominant. This is why these results are absolutely necessary to be taken into account for both STEREO and future missions described in Section 6.1, for which we also expect to observe mostly the shot noise at low frequencies (Figure 6.1).

Even though the theory of the shot noise at high frequencies was developed in the past, we still do not have an adequate, precise and fast numerical model that can be used for large data sets. This is why application of the QTN spectroscopy to the STEREO data, described in Chapter 4, was limited only to the low frequency part of the spectrum. The tools needed for creating an electron temperature database of the entire mission are developed in this Chapter. During this work, several additional issues appeared. Namely, the LFR instrument uncertainties cause very large measurement errors and it was necessary to perform averaging of the results during an empirically chosen time interval. The one hour interval was chosen using comparison with the Wind data for a short period where two spacecraft were positioned close to each other. This period was also used to verify the results from the method applied on STEREO by comparing the electron density and temperature with ones measured by reliable particle analyzers on Wind. At this point, developing of a 'version 0' database is in the initial phase, containing $n_e\sqrt{T_e}$ data, even though additional work needs to be done on estimation of the uncertainties. The total error of each one-hour averaged value is dependent from errors of the PLASTIC data, uncertainties obtained from fitting of each particular spectrum, deviations of the results during the averaging interval etc. Value of the error for the first version of the database is expected to be around 40%. This number does not look very impressive but, since at this point there is no data for thermal electrons on STEREO at all, it will present a useful order of magnitude estimate. More precise 'version 1' electron temperature data requires two crucial improvements. First, an efficient shot noise model above the plasma frequency needs to be developed, as already discussed above. This will enable us to include three times more frequency channels and decrease the measurement uncertainties and/or averaging time intervals. Second, the PLASTIC data update is essential in order to give more reliable electron density estimates. The uncertainties of the obtained electron temperature are expected to be larger than the ones that would be provided by the malfunctioning particle analyzers, but the results will still be reliable and useful to the community.

The second part of the theoretical work that still awaits its application is presented in Chapter 5. Although impedance of the antennas in collisional plasmas was studied by many previous authors, both in the ionosphere and in laboratory, the QTN spectroscopy was not used before in these particular environments. In

this work, we presented the theory of the antenna impedance and, directly from the Nyquist theorem, the thermal noise for plasmas where collisions occur mostly between electrons and neutrals. The main advantage of the model presented here is usage of the kinetic approach that relies on the Boltzmann equation instead of the hydrodynamic treatment that was usually used in this problematics and is valid only above the plasma frequency. This enabled us to introduce the method able to measure the electron density, temperature and electron-neutral collisional frequency as independent parameters while relying on the wide frequency range. However, despite the liability and accuracy of the theory, it must be noted that several limitations exist in realistic plasmas. The main issue is that our approach (and, in general, the QTN theory developed to this day) does not include magnetic field effects. This is a major difficulty for plasmas where the cyclotron frequency is comparable to the plasma frequency, for example at the ionosphere of Earth, and we can only use very low frequencies to estimate electron moments. This method still needs to be tested in Earth's ionosphere but it is expected to be more useful in studying unmagnetized planetary ionospheres. On the other hand, the magnetic field is not an issue in laboratory plasmas where it can be completely annulled. The QTN laboratory measurements are important both as a diagnostic tool and as a way to enable deeper investigation of the method itself in a controlled environment. Nonetheless, even in a highly stable facility with known plasma parameters, the important problem of the plasma sheath presence around the antenna will still persist. Namely, since the Debye length in these cold and dense plasmas can be very small and comparable to the antenna diameter, affection of the sheath to the measured power spectrum can become significant. We propose usage of very tiny antennas and/or the antenna biasing in order to avoid this problem and keep the antenna current distribution simple and similar to the one in the solar wind. The first laboratory thermal noise measurements are expected to be realized in the near future through the ongoing collaboration between Paris Observatory and University of Belgrade. These experiments might turn out to be very important for ground testing the responses of antennas with complicated geometries and, consequently, of the QTN spectroscopy as a piggyback technique used on the cubesats, which will usually be made with the body size comparable to the antenna length, or on other devices with complicated shapes.

Finally, we can conclude that this thesis gives answers to several questions in the field of the QTN spectroscopy, especially related to the shot noise, but it also (like any other scientific work) points out to a series of still unresolved topics that will be the subject of some future research. The impression in the space science community is that this field will become more and more interesting as time goes on, since the radio measurements can be performed even in the extreme conditions in proximity of the Sun - the next milestone for in situ measurements on space missions.

Bibliography

[Acuna et al., 1998] Acuna, M. H., Connerney, J. E. P., Wasilewski, P., Lin, R. P., Anderson, K. A., Carlson, C. W., McFadden, J., Curtis, D. W., Mitchell, D., Reme, H., Mazelle, C., Sauvaud, J. A., D'Uston, C., Cros, A., Medale, J. L., Bauer, S. J., Cloutier, P., Mayhew, M., Winterhalter, D., and Ness, N. F. (1998). Magnetic field and plasma observations at mars: Initial results of the mars global surveyor mission. *Science*, 279:1676–1680.

[Alexandrov et al., 1984] Alexandrov, A. F., Bogdankevich, L. S., and Rukhadze, A. A. (1984). *Principles of Plasma Electrodynamics*. Springer.

[Alfvén, 1941] Alfvén, H. (1941). On the motion of a charged particle in a magnetic field. *Arkiv för Matematik, Astronomi och Fysik*, 25:1–23.

[Allen, 1992] Allen, J. E. (1992). Probe theory - the orbital motion approach. *Physica Scripta*, 45:497–503.

[Allen, 2008] Allen, J. E. (2008). The plasma sheath boundary: its history and langmuir's definition of the sheath edge. *Plasma Sources Science and Technology*, 18:014004.

[Andronov, 1966] Andronov, A. A. (1966). Импеданс и шумы антенны (зонда) в космической плазмы. *Космические исследования*, 4:558–567.

[Annaratone et al., 1992] Annaratone, B. M., Allen, M. W., and Allen, J. E. (1992). Ion currents to cylindrical langmuir probes in rf plasmas. *Journal of Physics D: Applied Physics*, 25:417–424.

[Aubier et al., 1983] Aubier, M. G., Meyer-Vernet, N., and Pedersen, B. M. (1983). Shot noise from grain and particle impacts in saturn's ring plane. *Journal of Geophysical Research*, 88:8081–8093.

[Balanis, 1997] Balanis, C. A. (1997). *Antenna theory; Analysis and design*. Wiley.

[Bale et al., 2016] Bale, S. D., Goetz, K., Harvey, P. R., Turin, P., Bonnell, J. W., Dudok de Wit, T., Ergun, R. E., MacDowall, R. J., Pulupa, M., Andre, M., Bolton, M., Bougeret, J. L., Bowen, T. A., Burgess, D., Cattell, C. A., Chandran, B. D. G., Chaston, C. C., Chen, C. H. K., Choi, M. K., Connerney, J. E., Cranmer, S., Diaz-Aguado, M., Donakowski, W., Drake, J. F., Farrell, W. M., Fergeau, P., Fermin, J., Fischer, J., Fox, N., Glaser, D., Goldstein, M., Gordon, D., Hanson, E., Harris, S. E., Hayes, L. M., Hinze, J. J., Hollweg, J. V., Horbury, T. S., Howard, R. A., Hoxie, V., Jannet, G., Karlsson, M., Kasper, J. C., Kellogg, P. J., Kien, M., Klimchuk, J. A., Krasnoselskikh, V. V., Krucker, S., Lynch, J. J., Maksimović, M.,

Malaspina, D. M., Marker, S., Martin, P., Martinez-Oliveros, J., McCauley, J., McComas, D. J., McDonald, T., Meyer-Vernet, N., Moncuquet, M., Monson, S. J., Mozer, F. S., Murphy, S. D., Odom, J., Oliverson, R., Olson, J., Parker, E. N., Pankow, D., Phan, T., Quataert, E., Quinn, T., Ruplin, S. W., Salem, C., Seitz, D., Sheppard, D. A., Siy, A., Stevens, K., Summers, D., Szabo, A., Timofeeva, M., Vaivads, A., Velli, M., Yehle, A., Werthimer, D., and Wygant, J. R. (2016). The fields instrument suite for solar probe plus - measuring the coronal plasma and magnetic field, plasma waves and turbulence, and radio signatures of solar transients. *Space Science Reviews*.

[Bale et al., 2008] Bale, S. D., Ullrich, R., Goetz, K., Alster, N., Cecconi, B., Dekkali, M., Lingner, N., Macher, W., Manning Robert, E., McCauley, J., Monson, S. J., Oswald, T. H., and Pulupa, M. (2008). The electric antennas for the stereo/waves experiment. *Space Science Reviews*, 136:529–547.

[Balmain, 1964] Balmain, K. (1964). The impedance of a short dipole antenna in a magnetoplasma. *IEEE Transactions on Antennas and Propagation*, 12:605–617.

[Balmain, 1969] Balmain, K. (1969). Dipole admittance for magnetoplasma diagnostics. *IEEE Transactions on Antennas and Propagation*, 17:389–392.

[Bame et al., 1975] Bame, S. J., Asbridge, J. R., Feldman, W. C., Montgomery, M. D., and Kearney, P. D. (1975). Solar wind heavy ion abundances. *Solar Physics*, 43:463–473.

[Bame et al., 1992] Bame, S. J., McComas, D. J., Barraclough, B. L., Phillips, J. L., Sofaly, K. J., Chavez, J. C., Goldstein, B. E., and Sakurai, R. K. (1992). The ulysses solar wind plasma experiment. *Astronomy and Astrophysics Supplement Series*, 92:237–265.

[Baum et al., 1946] Baum, W. A., Johnson, F. S., Oberly, J. J., Rockwood, C. C., Strain, C. V., and Tousey, R. (1946). Solar ultraviolet spectrum to 88 kilometers. *Physical Review*, 70:781–782.

[Bernstein and Rabinowitz, 1959] Bernstein, I. B. and Rabinowitz, I. N. (1959). Theory of electrostatic probes in a low-density plasma. *Physics of Fluids*, 2:112–121.

[Bhatnagar et al., 1954] Bhatnagar, P. L., Gross, E. P., and Krook, M. (1954). A model for collision processes in gases. i. small amplitude processes in charged and neutral one-component systems. *Physical Review*, 94:511–525.

[Bilitza et al., 2011] Bilitza, D., McKinnell, L.-A., Reinisch, B., and Fuller-Rowell, T. (2011). The international reference ionosphere today and in the future. *Journal of Geodesy*, 85:909–920.

[Bishop, 1972] Bishop, R. H., B. K. D. (1972). Electron temperature and density determination from rf impedance probe measurements in the lower ionosphere. *Planetary and Space Science*, 20:997–1013.

[Blackwell et al., 2007a] Blackwell, D. D., Walker, D. N., Messer, S. J., and Amatucci, W. E. (2007a). Antenna impedance measurements in a magnetized plasma. i. spherical antenna. *Physics of Plasmas*, 14:092105.

[Blackwell et al., 2007b] Blackwell, D. D., Walker, D. N., Messer, S. J., and Amatucci, W. E. (2007b). Antenna impedance measurements in a magnetized plasma. ii. dipole antenna. *Physics of Plasmas*, 14:092106.

[Bougeret et al., 2008] Bougeret, J. L., Goetz, K., Kaiser, M. L., Bale, S. D., Kellogg, P. J., Maksimović, M., Monge, N., Monson, S. J., Astier, P. L., Davz, S., Dekkali, M., Hinye, J. J., Manning, R. E., and Aguilar-Rodriguez, E. (2008). S/waves: The radio and plasma wave investigation on the stereo mission. *Space Science Reviews*, 136:487–528.

[Bougeret et al., 1995] Bougeret, J. L., Kaiser, M. L., Kellogg, P. J., Manning, R., Goetz, K., Monson, S. J., Monge, N., Friel, L., Meetre, C. A., Perche, C., Sitruk, L., and Hoang, S. (1995). Waves: The radio and plasma wave investigation on the wind spacecraft. *Space Science Reviews*, 71:231–265.

[Brandt and Cassinelli, 1966] Brandt, J. C. and Cassinelli, J. P. (1966). Interplanetary gas. xi. an exospheric model of the solar wind. *Icarus*, 5:47–63.

[Buckley, 1966] Buckley, R. (1966). A theory of resonance rectification. the response of a spherical plasma probe to alternating potentials. *Proceedings of the Royal Society of London. Series A, Mathematical and Physical Sciences*, 290:186–219.

[Chamberlain, 1960] Chamberlain, J. W. (1960). Interplanetary gas.ii. expansion of a model solar corona. *Astrophysical Journal*, 131:47–56.

[Chateau and Meyer-Vernet, 1991] Chateau, Y. F. and Meyer-Vernet, N. (1991). Electrostatic noise in non-maxwellian plasmas: Generic properties and 'kappa' distributions. *Journal of Geophysical Research*, 96:5825–5836.

[Couturier et al., 1981] Couturier, P., Meyer-Vernet, N., Hoang, S., and Steinberg, J. L. (1981). Quasi-thermal noise in a stable plasma at rest: Theory and observations from isee 3. *Journal of Geophysical Research*, 86:11127–11138.

[Echim et al., 2011] Echim, M. M., Lemaire, J., and Lie-Svendsen, y. (2011). A review on solar wind modeling: Kinetic and fluid aspects. *Surveys in Geophysics*, 32:1–70.

[Edlén, 1943] Edlén, B. (1943). Die deutung der emissionslinien im spektrum der sonnenkorona. *Zeitschrift für Astrophysik*, 22:30–64.

[Escoubet et al., 1997] Escoubet, C. P., Pedersen, A., Schmidt, R., and Lindqvist, P. A. (1997). Density in the magnetosphere inferred from isee 1 spacecraft potential. *Journal of Geophysical Research*, 102:17595–17609.

[Fedorov et al., 2011] Fedorov, A., Opitz, A., Sauvaud, J. A., Luhmann, J. G., Curtis, D., and Larson, D. (2011). The impact solar wind electron analyzer (swea): Reconstruction of the swea transmission function by numerical simulation and data analysis. *Space Science Reviews*, 161:49–62.

[Fejer and Kan, 1969] Fejer, J. A. and Kan, J. R. (1969). Noise spectrum received by an antenna in a plasma. *Radio Science*, 4:721–728.

[Feldman et al., 1975] Feldman, W. C., Asbridge, J. R., Bame, S. J., Montgomery, M. D., and Gary, S. P. (1975). Solar wind electrons. *Journal of Geophysical Research*, 80:4181–4196.

[Fitzpatrick, 2014] Fitzpatrick, R. (2014). *Plasma Physics: An Introduction*. CRC Press.

[Franklin, 2003] Franklin, R. N. (2003). The plasma sheath boundary region. *Journal of Physics D: Applied Physics*, 36:R309–R320.

[Fried and Conte, 1961] Fried, B. D. and Conte, S. D. (1961). *The plasma dispersion function*. Academic Press New York.

[Galvin et al., 2008] Galvin, A., Kistler, L., Popecki, M., Farrugia, C., Simunac, K., Ellis, L., Möbius, E., Lee, M., Boehm, M., Carroll, J., Crawshaw, A., Conti, M., Demaine, P., Ellis, S., Gaidos, J., Googins, J., Granoff, M., Gustafson, A., Heirtzler, D., King, B., Knauss, U., Levasseur, J., Longworth, S., Singer, K., Turco, S., Vachon, P., Vosbury, M., Widholm, M., Blush, L. M., Karrer, R., Bochsler, P., Daoudi, H., Etter, A., Fischer, J., Jost, J., Opitz, A., Sigrist, M., Wurz, P., Klecker, B., Ertl, M., Seidenschwang, E., Wimmer-Schweingruber, R., Koeten, M., Thompson, B., and Steinfeld, D. (2008). The plasma and suprathermal ion composition (plastic) investigation on the stereo observatories. *Space Science Reviews*, 136:487–528.

[Gekelman et al., 1991] Gekelman, W., Pfister, H., Lucky, Z., Bamber, J., Leneman, D., and Maggs, J. (1991). Design, construction, and properties of the large plasma research device - the lapd at ucla. *Review of Scientific Instruments*, 62:2875–2883.

[Gosling et al., 1987] Gosling, J. T., Baker, D. N., Bame, S. J., Feldman, W. C., Zwickl, R. D., and Smith, E. J. (1987). Bidirectional solar wind electron heat flux events. *Journal of Geophysical Research*, 92:8519–8535.

[Graf and Jassby, 1967] Graf, K. A. and Jassby, D. L. (1967). Measurements of dipole antenna impedance in an isotropic laboratory plasma. *IEEE Transactions on Antennas and Propagation*, 5:681–688.

[Gringauz et al., 1960] Gringauz, K. I., Bezrokikh, V. V., Ozerov, V. D., and Rybchinskii, R. E. (1960). A study of the interplanetary ionized gas, high-energy electrons and corpuscular radiation from the sun by means of the three-electrode trap for charged particles on the second soviet cosmic rocket. *Soviet Physics Doklady*, 5:361–364.

[Grotrian, 1939] Grotrian, W. (1939). Zur frage der deutung der linien im spektrum der sonnenkorona. *Naturwissenschaften*, 27:214.

[Gurnett et al., 2004] Gurnett, D. A., Kurth, W. S., Kirchner, D. L., Hospodarsky, G. B., Averkamp, T. F., Zarka, P., Lecacheux, A., Manning, R., Roux, A., Canu, P., Cornilleau-Wehrlin, N., Galopeau, P., Meyer, A., Boström, R., Gustafsson, G., Wahlund, J. E., Åhlen, L., Rucker, H. O., Ladreiter, H. P., Macher, W., Woolliscroft, L. J. C., Alleyne, H., Kaiser, M. L., Desch, M. D., Farrell, W. M., Harvey, C. C., Louarn, P., Kellogg, P. J., Goetz, K., and Pedersen, A. (2004). The cassini radio and plasma wave investigation. *Space Science Reviews*, 114:395–463.

[Gurnett et al., 2001] Gurnett, D. A., Zarka, P., Manning, R., Kurth, W. S., Hospodarsky, G. B., Averkamp, T. F., Kaiser, M. L., and Farrell, W. M. (2001). Non-detection at venus of high-frequency radio signals characteristic of terrestrial lightning. *Nature*, 409:313–315.

[Hall and Landauer, 1971] Hall, T. A. and Landauer, G. (1971). Admittance of dipolar rf probes in a simulated ionosphere. *Radio Science*, 6:967–980.

[Hanson and Mantas, 1988] Hanson, W. B. and Mantas, G. P. (1988). Viking electron temperature measurements - evidence for a magnetic field in the martian ionosphere. *Journal of Geophysical Research*, 93:7538–7544.

[Harp, 1964] Harp, R. S. (1964). The behavior of the resonance probe in a plasma. *Applied Physics Letters*, 4:186–188.

[Henri et al., 2011] Henri, P., Meyer-Vernet, N., Briand, C., and Donato, S. (2011). Observations of langmuir ponderomotive effects using the solar terrestrial relations observatory spacecraft as a density probe. *Physics of Plasmas*, 18:082308.

[Hoang, 1972] Hoang, S. (1972). Admittance measurements of a 36-m dipole antenna in the topside ionosphere. *Planetary and Space Science*, 20:1185–1204.

[Hoang et al., 1980] Hoang, S., Steinberg, J. L., Epstein, G., Tilloles, P., Fainberg, J., and Stone, R. G. (1980). The low-frequency continuum as observed in the solar wind from isee 3 - thermal electrostatic noise. *Journal of Geophysical Research*, 85:3419–3430.

[Hoang et al., 1982] Hoang, S., Steinberg, J. L., Feldman, W. C., and Couturier, P. (1982). An electric noise component with density 1/f identified on isee 3. *Journal of Geophysical Research*, 87:9025–9034.

[Howard et al., 2008] Howard, R. A., Moses, J. D., Vourlidas, A., Newmark, J. S., Socker, D. G., Plunkett, S. P., Korendyke, C. M., Cook, J. W., Hurley, A., Davila, J. M., Thompson, W. T., St Cyr, O. C., Mentzell, E., Mehalick, K., Lemen, J. R., Wuelser, J. P., Duncan, D. W., Tarbell, T. D., Wolfson, C. J., Moore, A., Harrison, R. A., Waltham, N. R., Lang, J., Davis, C. J., Eyles, C. J., Mapson-Menard, H., Simnett, G. M., Halain, J. P., Defise, J. M., Mazy, E., Rochus, P., Mercier, R., Ravet, M. F., Delmotte, F., Auchere, F., Delaboudiniere, J. P., Bothmer, V., Deutsch, W., Wang, D., Rich, N., Cooper, S., Stephens, V., Maahs, G., Baugh, R., McMullin, D., and Carter, T. (2008). Sun earth connection coronal and heliospheric investigation (secchi). *Space Science Reviews*, 136:67–115.

[Issautier et al., 1999] Issautier, K., Meyer-Vernet, N., Moncuquet, M., and Hoang, S. (1999). Quasi-thermal noise in a drifting plasma: Theory and application to solar wind diagnostic on ulysses. *Journal of Geophysical Research*, 104:6691–6704.

[Jackson and Kane, 1959] Jackson, J. E. and Kane, J. A. (1959). Measurement of ionospheric electron densities using an rf probe technique. *Journal of Geophysical Research*, 64:1074–1075.

[Jockers, 1970] Jockers, K. (1970). Solar wind models based on exospheric theory. *Astronomy and Astrophysics*, 6:219–239.

[Kaiser, 1962] Kaiser, T. R. (1962). The admittance of an electric dipole in a magneto-ionic environment. *Planetary and Space Science*, 9:639–657.

[Kasper et al., 2015] Kasper, J. C., Abiad, R., Austin, G., Balat-Pichelin, M., Bale, S. D., Belcher, J. W., Berg, P., Bergner, H., Berthomier, M., Bookbinder, J., Etienne, B., Caldwell, D., W., C. A., Chandran, B. D. G., Cheimets, P., Cirtain, J. W., Cranmer, S. R., Curtis, D. W., Daigneau, P., Dalton, G., Dasgupta, B., DeTomaso, D., Diaz-Aguado, M., Đorđević, B., Donaskowski, B., Effinger, M., Florinski, V., Fox, N., Freeman, M., Gallagher, D., Gary, S. P., Gauron, T., Gates, R., Goldstein, M., Golub, L., Gordon, D. A., Gurnee, R., Guth, G., Halekas, J., Hatch, K., Heerikuisen, J., Ho, G., Hu, Q., Johnson, G., Jordan, S. P., Korreck, K. E., Larson, D., Lazarus, A. J., Li, G., Livi, R., Ludlam, M., Maksimović, M., McFadden, J. P., Marchant, W., Maruca, B. A., McComas, D. J., Messina, L., Mercer, T., Park, S., Peddie, A. M., Pogorelov, N., Reinhart, M. J., Richardson, J. D., Robinson, M., Rosen, I., Skoug, R. M., Slagle, A., Steinberg, J. T., Stevens, M. L., Szabo, A., Taylor, E. R., Tiu, C., Turin, P., Velli, M., Webb, G., Whittlesey, P., Wright, K., Wu, S. T., and Zank, G. (2015). Solar wind electrons alphas and protons (sweap) investigation: design of the solar wind and coronal plasma instrument suite for solar probe plus. *Space Science Reviews*.

[Katzin and Katzin, 1961] Katzin, J. C. and Katzin, M. (1961). The impedance of a cylindrical dipole in a homogeneous anisotropic ionosphere. Open File Rep. NAS 585-2, NASA Goddard Space Flight Center, 8800 Greenbelt Rd, Greenbelt, MD 20771, United States.

[Kellogg, 1981] Kellogg, P. (1981). Calculation and observation of thermal electrostatic noise in solar wind plasma. *Plasma Physics*, 23:735–751.

[Kellogg et al., 2009] Kellogg, P. J., Goetz, K., Monson, S. J., Bale, S. D., Reiner, M. J., and Maksimović, M. (2009). S/waves: The radio and plasma wave investigation on the stereo mission. *Journal of Geophysical Research*, 114:A02107.

[Knoll et al., 1978] Knoll, R., Epstein, G., Hoang, S., Huntzinger, G., Steinberg, J. L., Fainberg, J., Grena, F., Stone, R. G., and Mosier, S. R. (1978). The 3-dimensional radio mapping experiment /sbh/ on isee-c. *IEEE Transactions on Geoscience and Electronics*, GE-16:199–204.

[Kuehl, 1966] Kuehl, H. H. (1966). Resistance of a short antenna in a warm plasma. *Radio Science*, 1:971–976.

[Kuehl, 1967] Kuehl, H. H. (1967). Computations of the resistance of a short antenna in a warm plasma. *Radio Science*, 2:73–76.

[Laframboise, 1966] Laframboise, J. G. (1966). Theory of spherical and cylindrical langmuir probes in a collisionless, maxwellian plasma at rest. Open File Rep. 100, University of Toronto, Institute for Aerospace Studies, 4925 Dufferin Street, Toronto, Ontario, Canada.

[Laframboise and Parker, 1973] Laframboise, J. G. and Parker, L. W. (1973). Probe design for orbit-limited current collection. *The Physics of Fluids*, 16:629–636.

[Langmuir, 1923] Langmuir, I. (1923). Positive ion currents from the positive column of mercury arcs. *Science*, 58:290–291.

[Le Chat et al., 2011] Le Chat, G., Issautier, K., Meyer-Vernet, N., and Hoang, S. (2011). Large-scale variation of solar wind electron properties from quasi-thermal noise spectroscopy: Ulysses measurements. *Solar Physics*, 271:141–148.

[Le Chat et al., 2009] Le Chat, G., Issautier, K., Meyer-Vernet, N., Zouganelis, Y., Maksimović, M., and Moncuquet, M. (2009). Quasi-thermal noise in space plasma: 'kappa' distributions. *Physics of plasmas*, 16:102903.

[Le Chat et al., 2013] Le Chat, G., Zaslavsky, A., Meyer-Vernet, N., Issautier, K., Belheouane, S., Zouganelis, Y., Bale, S. D., and Kasper, J. C. (2013). Interplanetary nanodust detection by the solar terrestrial relations observatory/waves low frequency receiver. *Solar Physics*, 286:549–559.

[Lemaire and Scherer, 1971] Lemaire, J. and Scherer, M. (1971). Kinetic models of the solar wind. *Journal of Geophysical Research*, 76:7479–7490.

[Lin et al., 1995] Lin, R. P., Anderson, K. A., Ashford, S., Carlson, C., Curtis, D., Ergun, R., Larson, D., McFadden, J., McCarthy, M., Parks, G. K., Reme, H., Bosqued, J. M., Coutelier, J.and Cotin, F., D'Uston, C., Wenzel, K. P., Sanderson, T. R., Henrion, J., Ronnet, J. C., and Paschmann, G. (1995). A three-dimensional plasma and energetic particle investigation for the wind spacecraft. *Space Science Reviews*, 71:125–153.

[Liu et al., 2014] Liu, Y. D., Luhmann, J. G., Kajdič, P., Kilpua, E. K. J., Lugaz, N., Nitta, N. V., Möstl, C., Lavraud, B., Bale, S. D., Farrugia, C. J., and Galvin, A. B. (2014). Observations of an extreme storm in interplanetary space caused by successive coronal mass ejections. *Nature Communications*, 5:3481.

[Livesey and Pritchett, 1989] Livesey, W. A. and Pritchett, P. L. (1989). Two-dimensional simulations of a charge-neutral plasma beam injected into a transverse magnetic field. *Physics of Fluids B*, 1:914–922.

[Luhmann et al., 2008] Luhmann, J. G., Curtis, D. W., Schroeder, P., McCauley, J., Lin, R. P., Larson, D. E., Bale, S. D., Sauvaud, J. A., Aoustin, C., Mewaldt, R. A., Cummings, A. C., Stone, E. C., Davis, A. J., Cook, W. R., Kecman, B., Wiedenbeck, M. E., von Rosenvinge, T., Acuna, M. H., Reichenthal, L. S., Shuman, S., Wortman, K. A., Reames, D. V., Mueller-Mellin, R., Kunow, H., Mason, G. M., Walpole, P., Korth, A., Sanderson, T. R., Russell, C. T., and Gosling, J. T. (2008). Stereo impact investigation goals, measurements, and data products overview. *Space Science Reviews*, 136:117–186.

[Maksimović et al., 2007] Maksimović, M., Bale, S. D., Vaivads, A., Krasnoselskikh, V., Chust, T., Balikhin, M., Goetz, K., Gough, P., Travnicek, P., Soucek, J., and Rucker, H. (2007). A radio and plasma waves experiment for the solar orbiter mission. *Proceedings of the 2nd Solar Orbiter Workshop*.

[Maksimović et al., 2000] Maksimović, M., Gary, S. P., and Skoug, R. M. (2000). Solar wind electron suprathermal strength and temperature gradients: Ulysses observations. *Journal of Geophysical Research*, 105:18337–18350.

[Maksimović et al., 1992] Maksimović, M., Hoang, S., Meyer-Vernet, N., Moncuquet, M., Bougeret, J. L., Phillips, J. L., and Canu, P. (1992). Solar wind electron parameters from quasi-thermal noise spectroscopy and comparison with other measurements on ulysses. *Journal of Geophysical Research*, 100:19881–19892.

[Maksimović et al., 1997a] Maksimović, M., Pierrard, V., and Lemaire, J. F. (1997a). A kinetic model of the solar wind with kappa distribution functions in the corona. *Astronomy and Astrophysics*, 324:725–734.

[Maksimović et al., 1997b] Maksimović, M., Pierrard, V., and Riley, P. (1997b). Ulysses electron distributions fitted with kappa functions. *Geophysical Research Letters*, 9:1151–1154.

[Maksimović et al., 2005] Maksimović, M., Zouganelis, Y., Chaufray, J. Y., Issautier, K., Scime, E. E., Littleton, J. E., Marsch, E., McComas, D. J., Salem, C., Lin, R. P., and Elliot, H. (2005). Radial evolution of the electron distribution functions in the fast solar wind between 0.3 and 1.5 au. *Journal of Geophysical Research*, 110:A09104.

[Maksimovic et al., 1998] Maksimovic, M., Bougeret, J. L., Perche, C., Steinberg, J. T., Lazarus, A. J., Viñas, A. F., and Fitzenreiter, R. J. (1998). Solar wind density intercomparisons on the wind spacecraft using waves and swe experiments. *Geophysical Research Letters*, 25:1265–1268.

[Martinović, 2016] Martinović, M. M. (2016). Orbit limited teory in the solar wind - kappa distributions. *Serbian Astronomical Journal*, 192:27–34.

[Martinović et al., 2016a] Martinović, M. M., Zaslavsky, A., Maksimović, M., and Šegan, S. (2016a). Electrostatic thermal noise in a weakly ionized collisional plasma. *Submitted to Radio Science*.

[Martinović et al., 2016b] Martinović, M. M., Zaslavsky, A., Maksimović, M., Meyer-Vernet, N., Šegan, S., Zouganelis, Y., Salem, C., Pulupa, M., and Bale, S. D. (2016b). Quasi-thermal noise measurements on stereo: Kinetic temperature deduction using electron shot noise model. *Journal of Geophysical Research: Space Physics*, 121:129–139.

[Matthias et al., 2001] Matthias, A. R., Lazarus, A. J., and Steinberg, J. T. (2001). The solar wind helium abundance: Variation with wind speed and the solar cycle. *Geophysical Research Letters*, 136:2767–2770.

[Meyer and Vernet, 1975] Meyer, P. and Vernet, N. (1975). The impedance of a dipole antenna in the ionosphere 2, comparison with theory. *Radio Science*, 10:529–536.

[Meyer et al., 1974] Meyer, P., Vernet, N., and Lassudrie-Duchesne, P. (1974). Theoretical and experimental study of the effect of the sheath on an antenna immersed in a warm isotropic plasma. *Journal of Applied Physics*, 45:700–706.

[Meyer-Vernet, 1979] Meyer-Vernet, N. (1979). On natural noises detected by antennas in plasmas. *Journal of Geophysical Research*, 94:2405–2415.

[Meyer-Vernet, 1982] Meyer-Vernet, N. (1982). Flip-flop of electric potential of dust grains in space. *Astronomy and Astrophysics*, 105:98–106.

[Meyer-Vernet, 1983] Meyer-Vernet, N. (1983). Quasi-thermal noise correction due to particle impacts of emission. *Journal of Geophysical Research*, 88:8081–8093.

[Meyer-Vernet et al., 1986] Meyer-Vernet, N., Couturier, P., Hoang, S., Steinberg, J. L., and Zwickl, R. D. (1986). Ion thermal noise in the solar wind - interpretation of the 'excess' electric noise on isee 3. *Journal of Geophysical Research*, 91:3294–3298.

[Meyer-Vernet et al., 1993] Meyer-Vernet, N., Hoang, S., and Moncuquet, M. (1993). Bernstein waves in the io plasma torus: A novel kind of electron temperature sensor. *Journal of Geophysical Research*, 98:21163–21176.

[Meyer-Vernet and Issautier, 1998] Meyer-Vernet, N. and Issautier, K. (1998). Electron temperature in the solar wind: Generic radial variation from kinetic collisionless models. *Journal of Geophysical Research*, 103:29705–29718.

[Meyer-Vernet et al., 2009] Meyer-Vernet, N., Maksimović, M., Czechowski, A., Mann, I., Zouganelis, Y., Goetz, K., Kaiser, M. L., St Cyr, O. C., Bougeret, J. L., and Bale, S. D. (2009). Dust detection by the wave instrument on stereo: Nanoparticles picked up by the solar wind? *Solar Physics*, 256:463–474.

[Meyer-Vernet and Perche, 1989] Meyer-Vernet, N. and Perche, C. (1989). Tool kit for antennae and thermal noise near the plasma frequency. *Journal of Geophysical Research*, 94:2405–2415.

[Mishra et al., 2013] Mishra, S. K., Misra, S., and Sodha, M. S. (2013). Charging kinetics of dust particles in a non-maxwellian lorentzian plasma. *The European Physical Journal D*, 67:id.210.

[Moncuquet et al., 2005] Moncuquet, M., Lecacheux, A., Meyer-Vernet, N., Cecconi, B., and Kurth, W. S. (2005). Quasi thermal noise spectroscopy in the inner magnetosphere of saturn with cassini/rpws: Electron temperatures and density. *Geophysical Research Letters*, 32:L20S02.

[Mott-Smith and Langmuir, 1926] Mott-Smith, H. M. and Langmuir, I. (1926). The theory of collectors in gaseous discharges. *Physical Review*, 28:727–763.

[Nakatani and Kuehl, 1976] Nakatani, D. T. and Kuehl, H. H. (1976). Input impedance of a short dipole antenna in a warm anisotropic plasma, 1, kinetic theory. *Radio Science*, 11:433–444.

[Neugebauer and Snyder, 1966] Neugebauer, M. and Snyder, C. W. (1966). Mariner 2 observations of the solar wind, 1, average properties. *Journal of Geophysical Research*, 71:4469–4484.

[Nyquist, 1928] Nyquist, H. (1928). Thermal agitation of electric charge in conductors. *Physical Review*, 32:110–113.

[Ogilvie et al., 1995] Ogilvie, K. W., Chornay, D. J., Fritzenreiter, R. J., Hunsaker, F., Keller, J., Lobell, J., Miller, G., Scudder, J. D., Sittler Jr, E. C., Torbert, R. B., Bodet, D., Needell, G., Lazarus, A. J., Steinberg, J. T., Tappan, J. H., Mavretic, A., and Gergin, E. (1995). Swe, a comprehensive plasma instrument for the wind spacecraft. *Space Science Reviews*, 71:55–77.

[Ogilvie and Hirshberg, 1974] Ogilvie, K. W. and Hirshberg, J. (1974). The solar cycle variation of the solar wind helium abundance. *Journal of Geophysical Research*, 79:4595–4602.

[Ogilvie and Scudder, 1978] Ogilvie, K. W. and Scudder, J. D. (1978). The radial gradients and collisional properties of solar wind electrons. *Journal of Geophysical Research*, 83:3776–3782.

[Ogilvie et al., 1977] Ogilvie, K. W., von Rosenvinge, T., and Durney, A. C. (1977). International sun-earth explorer: A three-spacecraft program. *Science*, 198:131–138.

[Ogilvie et al., 1978] Ogilvie, K. W., von Rosenvinge, T., and Durney, A. C. (1978). Description of experimental investigations and instruments for the isee spacecraft. *IEEE Transactions on Geoscience and Electronics*, GE-16:151–153.

[Pannekoek, 1922] Pannekoek, A. (1922). Ionization in stellar atmospheres. *Bulletin of the Astronomical Institutes of the Netherlands*, 1:107–118.

[Pantellini et al., 2012] Pantellini, F., Meyer-Vernet, N., Belheouane, S., and Zaslavsky, A. (2012). Nano dust impacts on spacecraft and boom antenna charging. *Astrophysics and Space Science*, 341:309–314.

[Parker, 1958] Parker, E. N. (1958). Dynamics of the interplanetary gas and magnetic fields. *Astrophysical Journal*, 128:664–684.

[Pedersen, 1995] Pedersen, A. (1995). Solar wind and magnetosphere plasma diagnostics by spacecraft electrostatic potential measurements. *Annales Geophysicae*, 13:118–129.

[Perkins and Salpeter, 1965] Perkins, F. and Salpeter, E. E. (1965). Enhancement of plasma density fluctuations by nonthermal electrons. *Physical Review*, 139:55–62.

[Petit, 1975] Petit, M. (1975). Bruit radioélectrique dû aux photoélectrons. *Annales des Telecommunications*, 30:351–357.

[Pierrard and Lemaire, 2001] Pierrard, V. and Lemaire, J. (2001). Exospheric model of the plasmasphere. *Journal of Atmospheric and Solar-Terrestrial Physics*, 63:1261–1265.

[Pierrard and Lemaire, 1996] Pierrard, V. and Lemaire, J. F. (1996). Lorentzian ion exosphere model. *Journal of Geophysical Research*, 101:7923–7934.

[Pigache, 1973] Pigache, D. W. (1973). A laboratory simulation of the ionospheric plasma. *The American Institute of Aeronautics and Astronautics Journal*, 11:129–130.

[Pulupa et al., 2014] Pulupa, M., Bale, S. D., Salem, C., and Horaites, K. (2014). Spin-modulated spacecraft floating potential: Observations and effects on electron moments. *Journal of Geophysical Research: Space Physics*, 119:647–657.

[Rosenberg and Mendis, 1992] Rosenberg, M. and Mendis, D. A. (1992). A note on dust grain charging in space plasmas. *Journal of Geophysical Research*, 97:14773–14776.

[Rosseland, 1924] Rosseland, S. (1924). Electrical state of a star. *Monthly Notices of the Royal Astronomical Society*, 84:720–728.

[Roussel et al., 2005] Roussel, J. F., Rogier, F., Volpert, D., Rousseau, G., Forest, J., and Hilgers, A. (2005). Spacecraft plasma interaction software (spis): numerical solvers – methods and architecture. *Proceedings of 9th Spacecraft Charging Technology Conference*.

[Salem et al., 2003] Salem, C., Hoang, Sang Issautier, K., Maksimović, M., and Perche, C. (2003). Wind-ulysses in-situ thermal noise measurements of solar wind electron density and core temperature at solar maximum and minimum. *Advances in Space Research*, 32:491–496.

[Sauvaud et al., 2008] Sauvaud, J. A., Larson, D., Aoustin, C., Curtis, D., Médale, J. L., Fedorov, A., Rouzaud, J., Luhmann, J., Moreau, T., Schröder, P., Louarn, P., Dandouras, I., and Penou, E. (2008). The impact solar wind electron analyzer (swea). *Space Science Reviews*, 136:227–239.

[Schelkunoff and Friis, 1952] Schelkunoff, S. A. and Friis, H. T. (1952). *Antennas: theory and practice*. Wiley.

[Schiff, 1970] Schiff, M. L. (1970). Impedance of a short dipole antenna in a warm isotropic plasma. *Radio Science*, 5:1489–1496.

[Scime et al., 1994] Scime, E. E., Bame, S. J., Feldman, W. C., Gary, S. P., Phillips, J. L., and Balogh, A. (1994). Regulation of the solar wind electron heat flux from 1 to 5 au: Ulysses observations. *Journal of Geophysical Research*, 99:23401–23410.

[Scudder, 1992a] Scudder, J. D. (1992a). On the causes of temperature change in inhomogeneous low-density astrophysical plasmas. *The Astrophysical Journal*, 398:299–318.

[Scudder, 1992b] Scudder, J. D. (1992b). Why all stars should possess circumstellar temperature inversions. *The Astrophysical Journal*, 398:319–349.

[Scudder et al., 2000] Scudder, J. D., Cao, X., and Mozer, F. S. (2000). Photoemission current-spacecraft voltage relation: Key to routine, quantitative low-energy plasma measurements. *Journal of Geophysical Research*, 105:21281–21294.

[Seddon, 1953] Seddon, C. J. (1953). Propagation measurements in the ionosphere with the aid of rockets. *Journal of Geophysical Research*, 58:323–335.

[Seddon et al., 1954] Seddon, C. J., Pickar, A. D., and Jackson, J. E. (1954). Continuous electron density measurements up to 200km. *Journal of Geophysical Research*, 59.

[Spencer and Patra, 2015] Spencer, E. and Patra, S. (2015). Ionosphere plasma electron parameters from radio frequency sweeping impedance probe measurements. *Radio Science*, 50:853–965.

[Spencer, 1975] Spencer, W. T. (1975). Photoelectron emission analysis of surface elements of the international sun earth explorer. Open File Rep. NAS5-20592, Avco Systems Division, Wilmington, Massachusetts, USA.

[Stix, 1962] Stix, T. H. (1962). *The Theory of Plasma Waves*. McGraw-Hill.

[Stone et al., 1992] Stone, R. G., Bougeret, J. L., Caldwell, J., Canu, P., de Conchy, Y., Cornilleau-Wehrlin, N., Desch, M. D., Fainberg, J., Goetz, K., and Goldstein, M. L. (1992). The unified radio and plasma wave investigation. *Astronomy and Astrophysics Supplement Series*, 92:291–316.

[Sturrock and Hartle, 1966] Sturrock, P. A. and Hartle, R. E. (1966). Two-fluid model of the solar wind. *Physical Review Letters*, 14:628–631.

[Tong et al., 2015] Tong, Y., Pulupa, M., Salem, C., and Bale, S. D. (2015). Investigating wind quasi-thermal noise spectra between the ion and the electron plasma frequency. *AGU Fall Meeting Abstracts*.

[Tong et al., 2016] Tong, Y., Salem, C., Pulupa, M., and Bale, S. D. (2016). Manuscript in preparation.

[Štverak et al., 2009] Štverak, S., Maksimović, M., Travniček, P., Marsch, E., Fazakerley, A. N., and Scime, E. E. (2009). Radial evolution of nonthermal electron populations in the low-latitude solar wind: Helios, cluster, and ulysses observations. *Journal of Geophysical Research*, 114:A05104.

[von Steiger et al., 2000] von Steiger, R., Schwadron, N. A., Fisk, L. A., Geiss, J., Gloeckler, G., Hefti, S., Wilken, B., Wimmer-Schweingruber, R. F., and Zurbuchen, T. H. (2000). Composition of quasi-stationary solar wind flows from ulysses/solar wind ion composition spectrometer. *Journal of Geophysical Research*, 105:27217–27238.

[Wallace et al., 2004] Wallace, E., Thomas, E., Eadon, A., and Jackson, J. D. (2004). Design and initial operation of the auburn linear experiment for instability studies: A new plasma experiment for studying shear driven flows. *Review of Scientific Instruments*, 75:5160–5165.

[Watson, 1956] Watson, K. M. (1956). Use of the boltzmann equation for the study of ionized gases of low density i. *Physical Review*, 102:12–19.

[Wolff et al., 1971] Wolff, C. L., Brandt, J. C., and Southwick, R. G. (1971). A two-component model of the quiet solar wind with viscosity, magnetic field, and reduced heat conduction. *Astrophysical Journal*, 165:181–194.

[Zaslavsky et al., 2011] Zaslavsky, A., Meyer-Vernet, N., Hoang, S., Maksimović, M., and Bale, S. D. (2011). On the antenna calibration of space radio instruments using the galactic background: General formulas and application to stereo/waves. *Radio Science*, 46:RS2008.

[Zaslavsky et al., 2012] Zaslavsky, A., Meyer-Vernet, N., Mann, I., Chechowski, A., Issautier, K., Le Chat, G., Pantellini, F., Goetz, K., Maksimović, M., Bale, S. D., and Kasper, J. C. (2012). Interplanetary dust detection by radio antennas: Mass calibration and fluxes measured by stereo/waves. *Journal of Geophysical Research*, 117:A05102.

[Zhong et al., 2008] Zhong, W. Y., Shen, Z. X., Tai, Y. K. R., and Koh, W. J. (2008). Current distributions along a receiving thin dipole inside idela anechoic and reverberation champers. *Progress In Electromagnetics Research*, 105:105–120.

[Zouganelis, 2008] Zouganelis, Y. (2008). Measuring suprathermal electron parameters in space plasmas: Implementation of the quasi-thermal noise spectroscopy with kappa distributions using in situ ulysses/urap radio measurements in the solar wind. *Journal of Geophysical Research*, 113:A08111.

[Zouganelis et al., 2010] Zouganelis, Y., Maksimović, M., Meyer-Vernet, N., Bale, S. D., Eastwood, J. P., Zaslavsky, A., Dekkali, M., Goetz, K., and Kaiser, M. L. (2010). Measurements of stray antenna capacitance in the stereo/waves instrument: Comparison of the measured voltage spectrum with an antenna electron shot noise model. *Radio science*, 45:1005–1009.

[Zouganelis et al., 2004] Zouganelis, Y., Maksimović, M., Meyer-Vernet, N., Lamy, H., and Issautier, K. (2004). A transonic collisionless model of the solar wind. *The Astrophysical Journal*, 606:542–554.